

Surface acoustic wave-assisted scanning probe microscopy—a summary

This article has been downloaded from IOPscience. Please scroll down to see the full text article.

2010 Rep. Prog. Phys. 73 016102

(<http://iopscience.iop.org/0034-4885/73/1/016102>)

View [the table of contents for this issue](#), or go to the [journal homepage](#) for more

Download details:

IP Address: 133.28.19.14

The article was downloaded on 30/09/2010 at 09:42

Please note that [terms and conditions apply](#).

Surface acoustic wave-assisted scanning probe microscopy—a summary

Thorsten Hesjedal¹

Solid State and Photonics Lab, Department of Electrical Engineering, Stanford University, Stanford, CA 94305-4075, USA

E-mail: thorsten.hesjedal@stanford.edu

Received 2 June 2009, in final form 16 October 2009

Published 23 December 2009

Online at stacks.iop.org/RoPP/73/016102

Abstract

Elastic properties of nanoscopic materials, structures and thin films are important parameters controlling their growth, as well as their optical and electronic properties. Acoustic microscopy is a well-established method for elastic imaging. In order to overcome its micrometer-scale diffraction-limited lateral resolution, scanning probe microscopy-based acoustic near-field techniques have been developed. Among the acoustic modes used for microscopy, surface acoustic waves (SAWs) are especially suited for probing very small and thin objects due to their localization in the vicinity of the surface. Moreover, the study of SAWs is crucial for the design of frequency filter devices as well as for fundamental physical studies, for instance, the probing of composite fermions in two-dimensional electron systems.

This review discusses the capabilities and limitations of SAW-based scanning probe microscopy techniques. Particular emphasis is laid on the review of surface acoustic waves and their interaction with elastic inhomogeneities. Scattering, diffraction and wave localization phenomena will be discussed in detail. Finally, the possibilities for quantitative acoustic microscopy of objects on the nanoscale, as well as practical applications, are presented.

(Some figures in this article are in colour only in the electronic version)

This article was invited by K H Ploog.

¹ On leave from the Waterloo Institute for Nanotechnology, University of Waterloo, Waterloo, ON N2L 3G1, Canada.

Contents

1. Introduction	2	5.3. Investigation of non-collinear waves	17
2. Surface acoustic waves (SAWs): properties, interactions and excitation	2	5.4. Distortions and nonlinear effects	19
2.1. SAW modes and their properties	3	6. SAW-STM—‘seeing’ atoms oscillate	20
2.2. SAW excitation and detection	5	6.1. Contrast model	21
2.3. Determination of elastic constants	6	6.2. Surface oscillations on the atomic scale	24
3. Scanning probe microscopy of surface acoustic waves	7	7. Investigation of elementary wave phenomena	25
3.1. How to detect a high-frequency (mechanical) signal on the nanoscale?	7	7.1. Reflection and mode conversion	26
3.2. SAW-assisted atomic force microscopy—SAW-AFM	7	7.2. Scattering	27
3.3. SAW-assisted scanning tunneling microscopy—SAW-STM	9	7.3. Emission from elementary wave sources	29
4. SAW-AFM—amplitude detection	10	8. Ultrasound and friction on the nanoscale	31
4.1. Wave field imaging	10	8.1. Acoustically-induced superlubricity	31
4.2. Tip-sample force interaction	12	8.2. Lateral force rectification	34
5. SAW-AFM—phase detection	14	9. Technical applications—SAW device characterization	36
5.1. Phase velocities on the nanoscale	14	9.1. Resonator structures	36
5.2. Measurement of in-plane polarized waves	15	9.2. Acoustomigration	37
		10. Conclusions and perspectives	38
		Acknowledgments	40
		References	40

1. Introduction

The study of elastic properties of nanoscopic materials, structures and thin films allows for a deeper insight into the interplay of elastic phenomena with the growth of nanostructures, as well as their optical and electronic properties. Nanoscale elastic investigations are of great importance for applications on the macro-, micro- and nanoscale [1, 2]. On the one hand, the ongoing process of miniaturization demands increasingly smaller (nano-) structures. Due to their preparation (heteroepitaxy) they exhibit extreme mechanical stress—thus making the detailed knowledge of elastic properties essential [3]. On the other hand, micro- and nanoscopic defects are often the reason for fatigue in materials.

Acoustic methods are very useful tools for the investigation of elastic properties of crystalline and isotropic solids [4]. In order to overcome the diffraction limit of quantitative acoustic methods such as scanning acoustic microscopy (SAM) [5], near-field setups—either for the acoustic wave and/or for the probing wave—have to be employed. In the near-field regime, i.e. when the aperture or source/detector width is smaller than the involved wavelength, the lateral resolution becomes independent of the wavelength [6]. A near-field SAM has been constructed by adding a sub-wavelength focusing element, such as a truncated cone or a pin, to the end of the acoustic lens [7]. The use of miniaturized mechanical point transducers as acoustic sources and/or detectors is also possible, although the involved acoustic frequencies are rather in the kilohertz than in the megahertz range. In the kilohertz excitation range, the lateral resolution is determined by the tip diameter, which is typically a couple of micrometers [8]. In sections 4 and 5, acoustic wave detection by the nanoscopic tip of an atomic force microscope (AFM) will be discussed for excitation frequencies even reaching the gigahertz range. A related method, the tunneling acoustic microscope (TAM), relies on the wave excitation by a vibrating scanning tunneling microscope (STM) tip [9]. The use of the STM as a wave detector will be discussed in section 6.

The ultrasonic frequency range is well suited for studying thin film properties. In the first work reporting about the detection of surface vibrations at frequencies above the cantilever's resonance frequency, SAWs at 35 MHz were detected via self-mixing at the nonlinear force curve [10]. In subsequent years, several groups successfully detected ultrasound with an AFM [11–14]. Rabe and Arnold [15] found that the cantilever in contact is forced to vibrate also at higher harmonic bending modes [16]. Typically, the frequency range of 100 kHz to some 10 MHz is accessible. This method has been proven to be very useful for the quantitative determination of contact stiffness [17], local elasticity and lubrication measurements [19], as well as elastic properties of ultra-thin diamond-like carbon coatings [20]. The detection of ultrasonic waves by an AFM is possible by using the nonlinear force–distance curve [18] as a demodulator—effectively shifting the cantilever's rest position as a function of wave amplitude. This behavior is called the *mechanical diode effect* in analogy to the characteristic of an electrical diode (followed by a low-pass filter) [21]. The ultrasonic force modulation microscope,

the so-called ultrasonic force microscopy (UFM), has been successfully applied to the analysis of a variety of materials systems, such as semiconductors [22] and Ge islands on Si [23]. The nonlinear nature of the force interaction can also result in the sub-harmonic excitation of cantilever vibrations [24]. This way, high-frequency signals that are not directly accessible (e.g. 1 MHz) can be downconverted to a detectable frequency range. This effect can also be employed in the sense of laterally resolved mechanical spectroscopy (scanning local acceleration microscopy—SLAM) [25]. Moreover, the nonlinear force curve can be exploited in a heterodyne mixing scheme (heterodyne force microscopy—HFM) where waves are simultaneously launched through the cantilever and on the sample [26] and detected resonantly [27]. It has to be pointed out that most AFAM (acoustic AFM) techniques are meant for the study of the microscopic elastic properties of the tip–sample contact [28, 29]—and not the waves themselves [30].

As will be discussed, SAW-assisted scanning probe microscopy (SPM) relies on the detection of waves that have interacted with the elastic system. Despite their complexity, these methods have the inherent advantage that the tip–sample contact plays only a minor role for the determination of the elastic properties. Furthermore, the study of scattering, diffraction and localization phenomena of acoustic waves is of fundamental, as well as of technological interest. It allows a deeper insight into the function of technologically relevant high-frequency filter devices, which are widely employed in mobile phones, sensors and touchscreen displays. Moreover, the method has been recently expanded to the imaging of buried structures via near-field ultrasound holography [31].

2. Surface acoustic waves (SAWs): properties, interactions and excitation

Surface acoustic waves (SAWs) are additional solutions of the mechanical wave equation that exists on the plane, free surface of an infinite, homogeneous, isotropic and elastic solid [32]. The boundary conditions, which have to be fulfilled by surface waves in contrast to bulk waves, are responsible for their differences. The most important difference is that surface waves show a wave-like behavior in directions parallel to the surface and exhibit an exponential decay perpendicular to it. Therefore, SAWs offer unique opportunities for surface measurements, such as thin film non-destructive testing, and for simple and efficient excitation schemes.

In solid-state acoustics, SAWs are typically excited in the high frequency range between some 10 MHz to some gigahertz [33] at the interface between a piezoelectric solid and a second medium, which can be a thin film, a liquid or a gas. The most efficient way to excite and detect SAWs is by an interdigital transducer (IDT). IDTs are widely used in everyday life, e.g. in cell phones, TV sets, satellite communication and radar. The key to the success of these passive devices is the fact that the very fast electromagnetic waves ($v = c$)—with their impractically large wavelengths (dm to m)—can be slowed down five orders of magnitude by transforming them into acoustic waves. Their application as delay lines is thus self-evident. Since the wavelength is reduced by the same factor

($f = v/\lambda = \text{const.}$), micrometer-sized reflectors and waveguides allow for precise control of the frequency characteristics of a device. The current trend is to push the frequency limit of SAW devices into the 10 GHz range, to improve the acoustic materials, to reduce scattering and metallization damage and to apply them for sensing applications (e.g. powerless and wireless gas and liquid sensors).

2.1. SAW modes and their properties

The propagation of acoustic waves in a piezoelectric, charge-free medium is described by a system of coupled wave equations:

$$\rho \frac{\partial^2 u_j}{\partial t^2} = c_{ijkl} \frac{\partial^2 u_k}{\partial x_i \partial x_l} + e_{kij} \frac{\partial^2 \varphi}{\partial x_k \partial x_i}, \quad (2.1)$$

$$\varepsilon_{ik} \frac{\partial^2 \varphi}{\partial x_i \partial x_k} = e_{ikl} \frac{\partial^2 u_k}{\partial x_i \partial x_l}, \quad (2.2)$$

with u_i the particles' displacements, φ the electric potential, ρ the density, c_{ijkl} the elasticity or stiffness tensor, e_{kij} the piezoelectric tensor and ε_{ij} the dielectric tensor. In the case of surface waves, mechanical and electric boundary conditions have to be fulfilled. For an elastic medium ($x_3 < 0$), terminated by a stress-free surface at $x_3 = 0$, all stress components have to vanish in the x_3 -direction: $T_{3i} = 0$ (stress tensor T_{ij}). For piezoelectric media, the electric displacement component D_3 has to be continuous at the surface. If the surface is electrically short-circuited, the potential has to vanish at the surface. Similar conditions exist for layered media. In the case of vanishing piezoelectricity, i.e. $e_{kij} \rightarrow 0$, the system of coupled differential equations (2.1) and (2.2) renders the simple wave equation again.

In the general case there are 21 independent elastic constants c_{ijkl} in the elasticity tensor. With a higher crystal symmetry, the number of independent components is reduced as some c_{ijkl} become equal or vanish. The elasticity tensors for trigonal LiNbO₃, cubic GaAs and isotropic substrates are characterized by 6, 3 and 2 independent elastic constants, respectively. Further, in piezoelectric media the stress tensor T_{ij} and the electric field E_k , which are directly proportional to each other, are connected by the piezoelectric tensor e_{kij} . Consequently, deformations cause surface charges, and, conversely, the application of an electric field a deformation. These effects are called direct and inverse piezoelectric effects. The piezotensor can be written as a (3 × 6) matrix. Hence, there are 18 independent components. Again, as in the case of the c_{ijkl} s, higher crystal symmetries reduce the number of independent components. For triclinic substrates, trigonal LiNbO₃ and cubic GaAs the piezoelectric tensor has 18, 4 and 1 independent components, respectively. In dielectric solids, electric displacement D_i and electric field E_j are connected by $D_i = \varepsilon_{ij} E_j$ with ε_{ij} the dielectric tensor. The dielectric tensor (at constant strain) has 6 independent components in the case of a triclinic crystal and 1 for isotropic and cubic crystals. As SAWs are propagating at sonic speeds, the magnetic fields induced by oscillating electric fields can be neglected (electrostatic approximation).

The following partial wave ansatz solves the general form of the coupled wave equations:

$$\begin{aligned} u_j^m &= A_j^m \cdot \exp[-\alpha^m k x_3] \exp[i(\omega t - k x_1)], \\ \varphi^m &= A_4^m \cdot \exp[-\alpha^m k x_3] \exp[i(\omega t - k x_1)], \end{aligned} \quad (2.3)$$

and yields four complex pairs for the decay constants α^m with negative and positive real parts, and the corresponding vectors A^m ; which depend on the still unknown phase velocity (eigenvalue). In order to fulfill the boundary conditions, the solution (u_j, φ) is set up as a linear combination of four partial waves, α^m , and the resulting equation system is solved for the coefficients of the linear combination, yielding the phase velocity.

True SAWs consist only of partial waves with negative decay constants, since the amplitude should not diverge in depth. However, there are other solutions that fulfill the boundary conditions, when one or two of the negative decay constants are replaced by positive ones. Such solutions exhibit to a certain degree a bulk wave character and emit energy into the bulk. These modes are called pseudo-SAWs (PSAWs) or leaky waves [34] and are mainly transversally or longitudinally polarized. As a result of their partial bulk wave character, their phase velocity is very high.

In the case of an isotropic system, the only solution is the Rayleigh wave. The Rayleigh wave is polarized in the sagittal plane, which is defined by the propagation direction and the surface normal direction. The Rayleigh wave oscillation is composed of a longitudinal and a 90° phase-shifted vertical component. Figure 1 shows a snapshot of the particle oscillations for this wave type (for the specific materials system discussed in section 6.2). The particle movement takes place on elliptical trajectories, in the direction opposite to the wave propagation. As can be seen in the figure, the amplitude decays within one wavelength in depth.

The power flow in the absence of piezoelectricity and for Rayleigh waves propagating in the x_1 -direction, i.e. $W_2 = W_3 = 0$, can be obtained by integrating the equations. For typical transducer setups with $f = 219$ MHz and $W_1 = 1$ mW/330 μm the displacement components at the surface are $u_3 = 1.9$ Å in the vertical direction and $u_1 = 1.4$ Å in the longitudinal direction (on isotropic quartz glass with $\rho = 2.20 \times 10^3$ kg m⁻³, $c_{11} = 7.85 \times 10^{10}$ N m⁻², and $c_{12} = 1.61 \times 10^{10}$ N m⁻²). Compared with the wavelength of the Rayleigh wave of $\lambda = 15.6$ μm the displacement components are five orders of magnitude smaller.

The general characteristics of the solutions of the wave equation for a piezoelectric solid are the following: first, the propagating surface wave is accompanied both inside and outside the solid by a traveling electric field. Second, the inclusion of piezoelectricity for a given solid results in a higher wave velocity than for an elastically similar but non-piezoelectric solid—a phenomenon called piezoelectric stiffening. Third, the decay constants may become complex resulting in oscillatory particle displacement components in depth. The electromechanical coupling coefficient (K^2), which is a measure of the conversion efficiency between

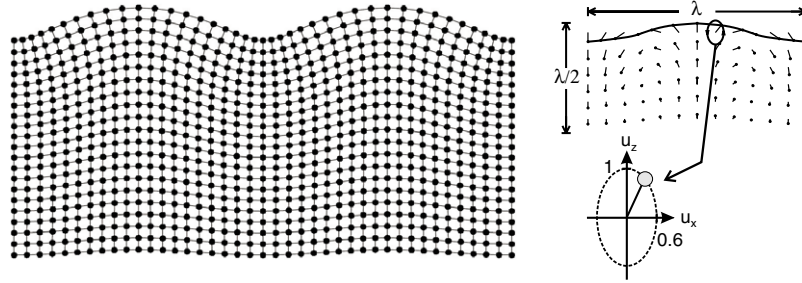


Figure 1. Snapshot of the oscillations within a propagating Rayleigh wave. Note the comparably low penetration depth. On the rhs, the elliptical trajectory of a volume element is highlighted.

electrical and acoustic energy, is defined for surface waves as

$$\frac{K^2}{2} = -\frac{\Delta v}{v_0} = \frac{v_0 - v_{0,s}}{v_0}, \quad (2.4)$$

where v_0 and $v_{0,s}$ are the propagation velocities on the free and the electrically shorted surface, respectively. The definition of K^2 becomes clearer when bearing in mind that the relative velocity change Δv is due to the elimination of energy storage outside the solid by electrical shorting through a massless, perfectly conducting film.

In anisotropic and piezoelectric materials, Rayleigh waves can also exist in certain high-symmetry crystal directions, e.g., YZ-cut lithium niobate (LiNbO_3). In more general cases, Rayleigh-like waves are found with an additional transversal component. These so-called generalized Rayleigh (GR) waves exist, e.g., on ST-cut quartz. When the propagation direction is not aligned with a high-symmetry direction, the excited modes can also show beam steering, i.e. the power flow angle and propagation direction are no longer parallel. This is a great disadvantage for designing a SAW device where the acoustic energy is to be transmitted with low loss between the transducers. On some piezoelectric materials, purely transversally polarized Bleustein–Gulyaev modes are found (e.g. in the $[0\ 1\ 1]$ -direction on GaAs(0 1 1)). In certain crystal directions on piezoelectric materials, modes exist that depend on the electric boundary conditions on the surface (e.g. in the $[1\ 0\ 0]$ -direction on GaAs(0 0 1)). These modes cannot be electrically excited (non-coupling SAW).

Another important property of SAWs is that they are dispersion free on homogeneous substrates. Since the physical problem of wave propagation within the continuum mechanical model is scale-invariant, the phase velocity is independent of wavelength. Modifications of the interface, however, alter the wave propagation properties in a very defined way. One example of electrically influencing the wave is electrical shorting of the free surface, which is used to determine the electromechanical coupling coefficient. The attachment of a layer to the surface of a free, infinite substrate with dimensions comparable to the wavelength of the SAW causes a shift of the phase velocity and, more importantly, the dependence of the phase velocity on the frequency of operation (dispersion). If the perturbed velocity is higher than the unperturbed one, the layer ‘stiffens’ the substrate; in the opposite case the layer ‘loads’ the substrate. Moreover, the addition of thin films to

the elastic system may introduce the existence of other modes, e.g. transversally polarized waves.

All real solids show to a certain degree nonlinear elastic behavior. In this sense the stress–strain relation is the linear approximation for small wave amplitudes. The consequences of elastic nonlinearity are the generation of harmonic frequencies and frequency mixing. From the viewpoint of the wave at the fundamental frequency these effects are sources of unwanted attenuation. Nevertheless, devices have been designed employing nonlinear effects, e.g. correlators and parametric amplifiers.

The attenuation of surface waves may be caused by different effects: interaction with thermal phonons (important in dielectric solids), interaction with electrons in metals and semiconductors, scattering due to changes in material properties such as surface and bulk defects, amplitude dependent conversion of energy from fundamental to harmonic frequencies in a nonlinear medium or loss due to viscous contaminants on the surface.

The scattering of acoustic waves becomes important when the size of an elastic inhomogeneity, such as a surface crack, surface roughness, lattice dislocations or a surface grain boundary, is comparable to the acoustic wavelength. The most important mechanism is elastic scattering accompanied with a change in the propagation direction. This mechanism is of importance for the whole range of SAW frequencies, while roughness-induced damping has to be considered for gigahertz SAWs only.

In order to study the surface acoustic wave propagation in layered structures utilizing materials of arbitrary anisotropy, piezoelectricity and conductivity, Adler’s matrix formalism is commonly used [35]. The software codes based on the matrix method that were used in our group were implemented by Makarov [36]. The general idea of Adler’s approach is to formulate a first-order matrix, ordinary differential equation using field quantities as variables which have to be continuous at the interfaces. For the state space approach including piezoelectricity an eight-component field vector \vec{r} has to be found. The vector of normal stresses and the vector of the three particle displacements are chosen as the six mechanical variables. They must be continuous across the interfaces. For piezoelectric materials, the electric potential and the normal electric displacement component are chosen as the two electric variables which have to be continuous at the interfaces too.

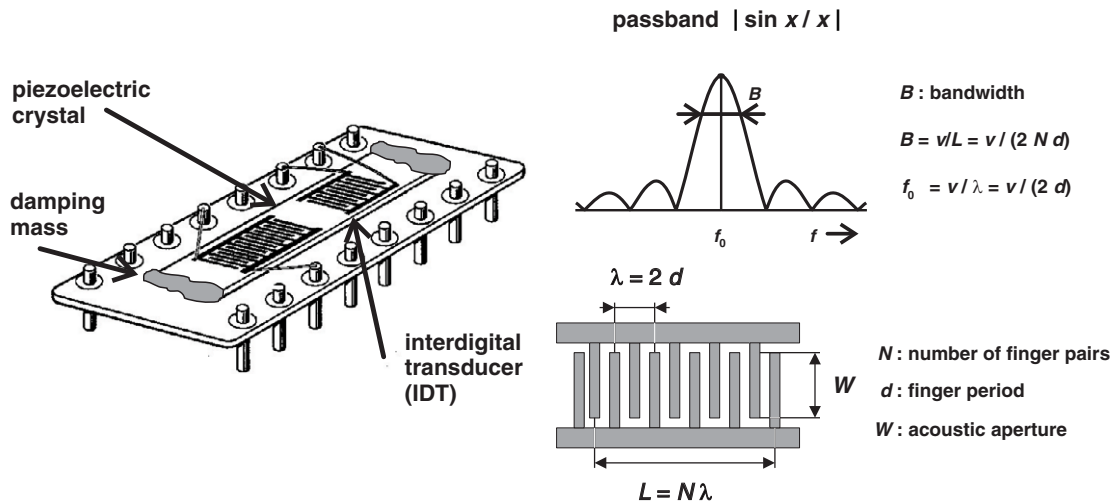


Figure 2. Schematic of a SAW device: planar, interdigital transducers (IDTs) are fabricated on the surface of a piezoelectric crystal by micro- or nanolithography. A damping mass prevents reflection from the chip edges. The transmission of an IDT is shown on the rhs: while the center frequency is determined by the spacing of the interdigitated electrodes, the bandwidth is given by the length of the device (i.e. ‘quality’ of the cavity) at a given phase velocity of the material.

2.2. SAW excitation and detection

SAW excitation. Various physical effects couple to elastic waves and can therefore be exploited for acoustic wave excitation and/or detection. The choice of a certain transduction scheme depends on the required bandwidth, efficiency, environment (air, vacuum, coupling liquid) and substrate (piezoelectric, magnetic). The excitation methods can be roughly separated into piezoelectric, optical, mechanical, magnetic, thermal and piezoresistive transduction, as well as mode conversion. As most excitation processes are reversible, a transducer may be used for both excitation and detection purposes. The most common scheme is the interdigital transducer (IDT), which is restricted to piezoelectric substrates. For materials investigations, optical non-contact excitation and detection on arbitrary substrates are most commonly employed.

The foundation for the commercial success of SAWs was the invention of the IDT by White and Voltmer [37]. IDTs solely rely on surface fabrication techniques and they allow for the efficient and reversible transduction of electric signals. On piezoelectric materials, a pair of conducting electrodes that produces spatially non-uniform and oscillating electric fields acts as a source of varying local stresses which can lead to acoustic waves. To increase the efficiency of an IDT, many of these single electrode pairs have to be placed in an array such that the waves interfere constructively (figure 2, rhs). In figure 2 (lhs) a SAW delay line mounted on a high-frequency chip holder is shown. Usually a cover encloses the chip. To suppress undesired SAW reflections from the edges, acoustic absorbers (damping mass) are employed.

In principle, the behavior of an IDT should be calculable since the geometry of a source, in conjunction with the propagation velocity of the substrate, precisely determines the center frequency. However, an exact mathematical treatment of the IDT behavior over the whole frequency range is not possible due to the complicated boundary conditions. When

treating the problem in two dimensions, diffraction and beam-steering have to be considered too. Today, many elaborated numerical solutions of the IDT problem exist including the so-called 2nd order effects [38]. Nevertheless, the main properties of IDTs can be understood in terms of equivalent circuit models, such as the delta function model [39], the crossed-field model [40] or the impulse response model [41]. Each model describes a restricted number of IDT parameters. Detailed presentations of IDT design can be found in various textbooks, e.g., [42, 43].

The delta function model approximates the complex electric field distribution between adjacent IDT electrodes by a discrete number of delta function sources. A summation over all delta sources then gives the simulated electric field intensity of one IDT. By including a second IDT in the summation procedure, the overall transfer response of a delay line can be obtained. The response function $H_1(f)$ of the input IDT can be written for frequencies close to the center frequency f_0 , and for a single-finger IDT transmission line with equal distance and equal width of the electrode fingers, as $|H(f)| \simeq 2N|\sin X/X|$ with $X = N\pi(f - f_0)/f_0$. The calculated response $|H_1(f)|$ is schematically sketched in figure 2 together with the geometry of a single-finger IDT of finger width $d/2$, acoustic aperture W , number of finger pairs N and IDT length $L = 2Nd$. The bandwidth B decreases with increasing number of finger pairs.

Since conventional IDTs emit SAWs in two directions, a loss of 3 dB is unavoidable (6 dB for a delay line). One solution is unidirectional transducers that break the symmetry of the device. As shown above, the bandwidth of the device is inversely proportional to the number of electrode pairs. One disadvantage of this design is that the IDT also acts as a perfect reflector for waves of the same frequency. These reflections distort SAW-AFM measurements and have to be avoided. A solution is the use of split-finger IDTs. Since the topographic period of the electrodes is different from the wavelength, reflections for waves at the center frequency play a minor role.

Therefore, this transducer type was preferred for SAW-assisted scanning probe microscopy experiments. Another advantage is the fact that double-finger IDTs allow for the excitation of waves at the third harmonic, which is important for dispersion measurements.

As the minimal structural feature size in standard photolithography is on the order of $0.4\ \mu\text{m}$, high performance IDTs are limited in their driving frequency to about 1 GHz. As the frequency range of 2.4 GHz and above was to be explored, other routes were taken. One possibility is the use of costly electron beam lithography, with which IDTs with frequencies in the 10 GHz range have been realized. Another approach is to drive the IDT at higher harmonics. The first excitable higher harmonic of the fundamental frequency f_0 exists in single-finger IDTs at $5 \times f_0$ and in split-finger IDTs at $3 \times f_0$. Recently, a novel piezoelectric interdigital transducer has been introduced that is based on the alternate poling of ferroelectric domains on the nanoscale [44]. Finally, new materials systems with higher phase velocities have been developed. Diamond-like carbon (DLC) thin films can be deposited on silicon and were combined with piezoelectric thin films for SAW excitation [45]. For the integration of electronic and acoustic functions on a single chip, piezoelectric GaAs cuts have been successfully used. Waferbonding for the fabrication of hybrid systems is another successful technique to reduce costs and integrate piezoelectric LiTaO₃ or LiNbO₃ films with silicon [46].

The IDTs used in the SAW-assisted SPM studies were in most cases double-finger IDTs. They were fabricated by optical and electron beam lithography on quartz or GaAs wafers and are composed of 1400 single electrodes and cover a frequency range from 200 MHz to 1.2 GHz. This corresponds to structural feature sizes of $1.3\text{--}0.28\ \mu\text{m}$ or wavelengths of $14.4\text{--}2.24\ \mu\text{m}$. The electrically measured insertion losses were between -30 and -15 dB. The aperture of the IDTs, and thus the SAW beam width, was between 350 and $46\ \mu\text{m}$ and the transducer length between 4 and 0.8 mm. The metallization of the devices was commonly Ti/Al/Ti.

Alternative ways of SAW excitation. Utilizing laser irradiation, acoustic wave pulses can be excited on solid surfaces [47], and even the excitation of continuous waves has been demonstrated [48]. At sufficiently low power densities, where there is no change in the state of the solid, the excitation of acoustic waves is mainly due to thermal expansion [49]. The thermoelastically generated strains exist primarily parallel to the surface. In addition to longitudinal and shear bulk waves, different SAW modes can be generated. However, the bandwidth of the excited SAWs in the film plane is limited due to the traveling time across the laser spot to some 100 MHz. Please note that in thin films, acoustic bulk waves can be excited in the terahertz range and acoustic wavelengths of down to 14 nm have been demonstrated [50].

SAW detection. The acousto-optic interaction is suitable for studying sound waves on solids [51, 52]. SAWs modulate not only the index of refraction in the wave-guiding surface but they lead also to a periodic, dynamic diffraction grid.

Both modulations appear stationary for the fast probing light. Using the wave-guiding surface as a reflecting mirror of an interferometer, displacements as small as $10^{-2}\ \text{\AA}$ can be resolved. Heterodyne techniques based on the interference of the diffracted light field with a reference light field are capable of measuring the amplitude as well as the phase of acoustic waves [53]. Employing an additional frequency shifter, the displacement resolution can be extended to $10^{-3}\ \text{\AA}$. Furthermore, the surface modulation can be transferred to an intensity modulation at the acoustic frequency using a knife-edge technique. The vertical sensitivity is approximately $0.1\ \text{\AA}$ at a frequency of 10 MHz. SAW imaging by optical methods is generally diffraction limited to $\approx 1\ \mu\text{m}$. Another complication for the detection of SAWs in interdigital transducers is the largely different reflection coefficients for the piezoelectric substrate and the metallic structure.

The SAW detection by scanning electron microscopy (SEM) is relying on the modulation of the secondary electron (SE) yield due to the spatially varying electric surface potentials [54]. The applicability of the method is very limited as the piezoelectric substrates are in general poorly conductive and image distortions due to charging unavoidable. The practical lateral resolution is on the order of $1\ \mu\text{m}$ and the frequency detection limit ≈ 500 MHz [55]. Besides optical probing and SEM, other methods have been used for detecting SAWs, such as capacitive probing [56], holographic techniques [57], stroboscopic x-ray topography techniques [58] and mechanical contact transducers [59].

2.3. Determination of elastic constants

Quantitative non-destructive evaluation of a sample by ultrasonic techniques provides access to the elastic constants of the substrate and the attached layers [60]. The study of thin films is particularly important as their mechanical, thermal, optical and electrical properties can be easily tailored and determine the properties of a device. Well-known examples are carbide and nitride hard coatings, diamond-like carbon films for improved hardness and thermal stability, and semiconductor heterostructures for electronic and optical applications [61].

The measurement of stress in thin films and the determination of the elastic constants are important for optimizing the materials properties. Stress in thin film systems arises from interfaces with dissimilar materials or from crystal imperfections, such as grain boundaries, dislocations or impurities [62]. Areas of intense study include the supermodulus effect in superlattices [63] for protective tribological coatings [64], as well as the tailoring of stressor structures on semiconductor surfaces for the lateral confinement of carriers (creating stress-induced quantum wires and quantum dots) [65].

Surface acoustic waves are a well-suited probe for the investigation of elastic constants of thin films and laterally confined micro- and nanostructures. Measuring the SAW interaction with the sample over a wide frequency range allows for the simultaneous investigation of the substrate and the attached layers or structures. To increase the sensitivity,

and to allow for the study of very thin layers, high acoustic frequencies and large bandwidths are required.

The main influence of an elastically inhomogeneous region on the wave propagation is the alteration of the SAW velocity. By measuring the velocity dispersion of different acoustic modes, i.e. the dependence of the phase velocity on the parameter $\gamma = kh$ with k the wave number of the SAW and h the film thickness, the calculation of the elastic constants becomes possible. The parameter γ can be varied either by measuring a frequency spectrum or by measuring samples with different thicknesses. The frequency variation technique, requiring a broadband acoustic source, has obvious advantages as one and the same sample can be investigated. Another possibility is the measurement of $v(kh)$ in dependence of the propagation direction on anisotropic samples. Solving the so-called inverse problem yields the elastic constants from the velocity dispersion data [66].

In the case of an unknown isotropic film on a known anisotropic substrate, four constants (density, thickness, two elastic constants) have to be determined. While determining film thickness and density is relatively easy, Young's modulus E and Poisson's ratio ν are obtained via the measurement of the acoustic velocity dispersion. In general, relying on only one acoustic mode will yield only one elastic constant. However, since Poisson's ratio does not vary very much for many types of samples, Young's modulus can be extracted using a single acoustic mode. In general, however, even small errors in the measurement of the phase velocities of about 0.1% will lead to large errors in the calculated moduli c_{11} and c_{12} of 5% and 30%, respectively. Fortunately, by measuring the dispersion of two acoustic modes and by superimposing their error fields a higher accuracy of $\approx 1\%$ can be reached [36].

3. Scanning probe microscopy of surface acoustic waves

Scanning probe microscopy (SPM) comprises techniques suitable for measuring phenomena on a very small length scale, e.g. atomic force microscopy (AFM) and scanning tunneling microscopy (STM). The main hurdle in detecting ultrasonic waves by scanning probe microscopy—and high-frequency signals in general—is their limited detection bandwidth.

3.1. How to detect a high-frequency (mechanical) signal on the nanoscale?

The key to high-frequency detection in bandwidth-limited systems is nonlinear response characteristics. This means that the output signal is a nonlinear function of the parameter that is modulated by an acoustic wave, e.g. the distance. Bandwidth limits in SPM can have technical or physical reasons. In STM, the inherent bandwidth of the tunneling process is certainly very high and not preventing the detection of gigahertz frequency SAWs. On the other hand, the small tunneling current has to be amplified and the gain–bandwidth product of the amplifier is limited. In AFM, on the other hand, the mechanical resonance of the cantilever is the bandwidth-limiting factor. Although a lot of progress has been made in

the fabrication of mechanical systems resonating at gigahertz frequencies, common AFM cantilevers have for practical reasons much lower resonance frequencies; typically on the order of 100 kHz. One way of overcoming the frequency limit, at least in parts, is the excitation of higher harmonics of the cantilever oscillation [67]. To explore the frequency range beyond some 100 MHz, however, a different approach is required.

A nonlinear signal–distance curve, e.g., the force–distance curve in the case of AFM, leads to diode-like behavior of the physical system (with a subsequent low-pass filter in the case of AFM). Analogous to a crystal radio receiver diode, which demodulates amplitude-modulated RF signals and delivers the modulation signal in the audible frequency range, the nonlinear force–distance relationship can be used for the demodulation of amplitude-modulated RF surface oscillations—resembling a *mechanical diode*. In addition to this homodyne detection scheme, the phase information can be extracted in a heterodyne scheme by mixing an acoustic sample wave with a slightly frequency-detuned reference wave at the mechanical diode. This leads to cantilever oscillations at their difference frequency Δf , which is typically chosen to be well below the cantilever's resonance frequency. In principle, Δf can also be chosen to coincide with a higher cantilever eigenmode [68]. A very similar scheme can be applied to STM imaging of SAWs.

Note that this detection scheme is not limited to the detection of ultrasound [69]. Any combination of high-frequency modulations of the tip–sample interaction can be utilized for new types of microscopy: (I) acoustic-acoustic modulation (heterodyne SAW-AFM), where one wave might propagate through a wave-guiding cantilever, (II) acoustic–electric modulation (SAW-STM, heterodyne SAW-AFM) and (III) electric–electric modulation which can be used to measure the electric field distribution within interdigital transducers [70], to construct a simple and reliable scanning capacitance microscope [71] or to detect wiring errors in integrated circuits thermally without special AFM cantilevers [70].

3.2. SAW-assisted atomic force microscopy—SAW-AFM

The SAW-assisted AFM (SAW-AFM; also: scanning acoustic force microscopy—SAFM) was developed around the same time as most of the other common ultrasonic scanning probe microscopy techniques. The main difference, however, is that the SAW-AFM is detecting waves that have interacted with the elastic system, whereas the other methods are relying on the analysis of the tip–sample contact itself [72]. The nanoscopic tip–sample contact is in general not long-term stable and thus difficult to model. Moreover, SAW-AFM allows for the detailed mapping of SAW amplitudes within SAW devices [73].

A SAW-AFM is based on a conventional atomic force microscope operating in contact mode. Please note that in non-contact mode, the cantilever is responding to both acoustic vibrations as well as electric RF signals [74]. Figure 3 illustrates the experimental situation: a SAW device

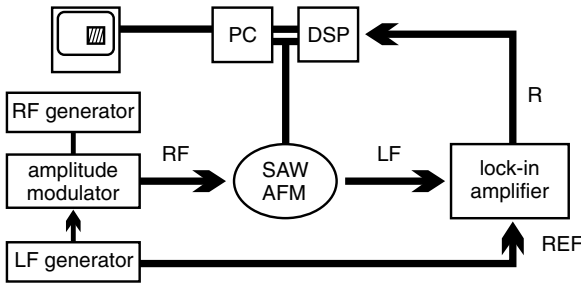


Figure 4. Schematic of amplitude mode SAW-AFM.

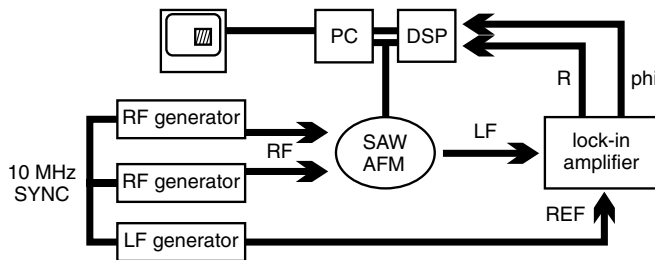


Figure 5. Schematic of phase mode SAW-AFM.

The low-frequency reference signal at Δf is coming from an additional, synchronized signal generator. Finally, the lock-in amplifier analyzes the incoming signal at Δf and feeds the amplitude and phase information into the AFM's DSP.

In an alternative setup, the low-frequency generator can be replaced by a passive frequency mixer (ring modulator), which is driven by the power of the RF generators directly. The mixer then provides the electric signal at the difference frequency which can be, after filtering and amplification, fed to the lock-in amplifier. This alternative has in principle the advantage that the same phase noise and drift of the RF signal generators appear in both the signal and reference path. However, lock-in amplifiers which obtain their internal reference signal by a rather slow PLL (phase-locked loop) circuit from the input reference cannot profit from the mixer approach. Furthermore, the connection of the mixers directly to the RF signal generator outputs poses another problem as the SAW devices are generally poorly impedance matched compared with the mixer element. Therefore, most of the power is dissipated at the mixers and cannot be used for SAW excitation.

To estimate the oscillation amplitudes of the cantilever in a typical SAW-AFM experiment, the deflection signal during a scan over a topographic step was measured. When the feedback loop for the AFM distance control is disabled, the resulting electric deflection signal can be associated with a calibrated step height. In the case of test grids with 25.5 and 105 nm steps, voltages of 1.2 and 4.6 V were measured, respectively. Admittedly, a generalization of a quasi-static deflection obtained this way to SAW-induced amplitudes is critical. By choosing a low modulation frequency of 5 kHz, which is well below the cantilever resonance and which assures that the detector is in its linear regime, the static approximation of $\sim 22 \text{ nm V}^{-1}$ is valid for SAW signals too. Typical SAW-related measurement signals are of the order of 1 mV, i.e. the cantilever oscillation amplitude is $\approx 20 \text{ pm}$.

3.3. SAW-assisted scanning tunneling microscopy—SAW-STM

In contrast to SAW-AFM, the tunneling process inherently offers a large detection bandwidth with corresponding time scales of 10 fs [75, 76], even allowing for phonon detection [77]. Moreover, there is no physical limit to the detection of arbitrarily polarized SAWs given by the cantilever in SAW-AFM (cantilevers have a very limited ability to follow arbitrary surface motions).

To detect SAWs with an STM, several approaches seem feasible. First of all, the direct SAW-induced contribution to the dc tunneling current can be detected, similar to amplitude mode SAW-AFM. For applying the mixing technique, a high-frequency reference signal has to be applied to the tunneling gap. It turned out that this can be simply achieved by direct coupling of the RF signal to the tip up to 100 MHz. Higher frequencies demand a more sophisticated setup, where the RF signal is guided coaxially to the tip. The first ideas for phase-accurate probing of SAWs by the SAW-STM mixing technique were presented by Chilla and coworkers [78, 79]. Amplitude-modulated bulk waves have been detected by STM with a modulation frequency that is higher than the feedback frequency but still within the pre-amplifier bandwidth [80]. The implementation of a boxcar integrator further allows the detection of the traveling time of the wave as a function of distance from the IDT, thus yielding the phase velocity [81].

A block diagram of the SAW-STM setup is shown in figure 6. The signals of the two RF generators are fed without any electrical matching to the IDT and to the tip via a bias-T (capacitive coupling). Typical signal voltages are 1 V and 0.5 V rms, respectively. Additionally, both signals are mixed externally. This difference frequency signal is used as a reference for the lock-in amplifier. The difference frequency is typically between 10 and 50 kHz. After mixing at the nonlinear tunneling curve, the signal at the difference frequency is separated from the other mixing products simply by utilizing the low-pass filtering properties of the operational amplifier. The amplified tunneling signal is then fed to the signal channel of the lock-in amplifier which now delivers the amplitude and the relative phase with respect to the phase of the externally mixed reference signal. The gap distance is controlled by the dc component of the tunneling current. The typical measurement parameters are SAW amplitude $< 1 \text{ \AA}$, SAW frequencies $\leq 700 \text{ MHz}$, dc tip voltage $\approx 100 \text{ mV}$, dc tunneling current $\approx 10 \text{ nA}$, and ac tip voltage $< 0.5 \text{ V}$. The estimated tunneling distance is on the order of 5 \AA .

It has to be noted that the direct detection by transient current recording at the SAW frequency is not easily possible. The bandwidth of the STM electronics is typically 100 kHz, not only as a result of the gain–bandwidth product but also because of the stray capacitances (parallel to the feedback resistance and parallel to the input terminals of the amplifier). Commonly, a trade-off has to be made between the signal-to-noise ratio and the bandwidth of the STM electronics: a desirable gain of 1 V/1 nA leads to a bandwidth in the kilohertz range. Another approach would be to transmit the tunneling signal via a coaxial cable to frequency-selective amplifiers. Unfortunately, the coaxial cable acts as the major noise source for the dc current

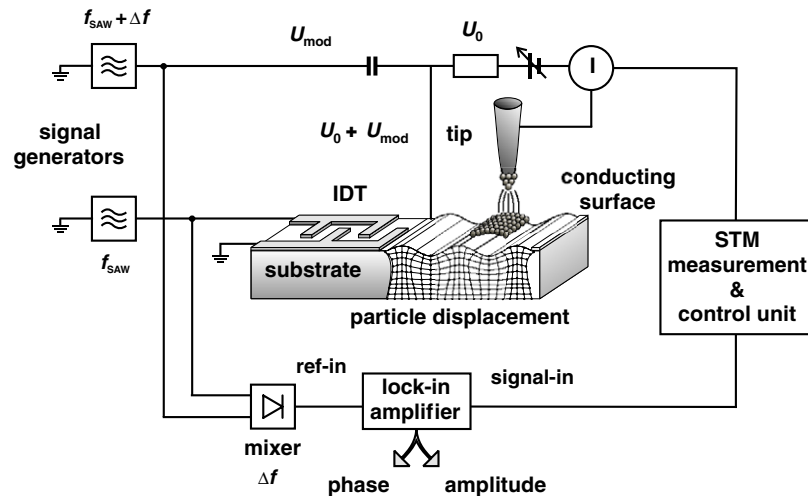


Figure 6. Experimental setup of the mixing type SAW-STM. The RF signals are fed to the IDT and the tip. Their external mixing signal is used as a reference for the lock-in amplifier which is used to analyze the tunneling current.

(microphone effect) [82]. The deformation of the cable due to acoustic vibrations leads to capacitance changes and thus a noise current. By assuming a 1 kHz noise signal with an amplitude of 1 pF (cable capacitance: 100 pF per meter), a noise current of 60 pA will result for a cable voltage of 10 mV.

4. SAW-AFM—amplitude detection

The mapping of the SAW amplitude with sub-micrometer lateral resolution by SAW-AFM is the technologically most important SAW-SPM technique. Since modern SAW devices for the mobile telecommunications industry are operated at gigahertz frequencies, the involved SAWs have wavelengths on the submicrometer scale which cannot be easily detected by optical probing techniques. The lateral resolution of SAW-AFM is the same as for conventional force microscopy, and thus determined by the radius of curvature of the tip (typically 10 nm). Other SAW detection techniques are hampered by the need for single-crystalline samples (x-ray topography) or conducting substrates (electron microscopy). Both limitations are not present for SAW-AFM, since the contrast mechanism is of mechanical nature. As a result, no special sample preparation is needed. SAW-AFM is also capable of characterizing in-plane polarized acoustic modes. These modes are not easily detectable by conventional characterization techniques [83, 84] and, as a consequence, have not been investigated in great detail.

4.1. Wave field imaging

Acoustic beams. As the simplest model system for SAW amplitude mapping, the wave field emitted from an IDT was investigated. For this experiment, a special transducer was fabricated that has a rather small aperture (overlap of the interdigitated electrodes) of five wavelengths. This allows for imaging the propagating and diffracted SAW beams in a single AFM scan. The IDT is a single-finger transducer which was fabricated by photolithography (smallest structural feature size: $1.4 \mu\text{m}$) on the (001) surface of GaAs (propagation

direction along [110]). In this structural configuration, Rayleigh waves with a wavelength of $5.6 \mu\text{m}$ are excited at a center frequency of 538 MHz. The very small aperture width is compromising the electric properties, i.e. the impedance matching of the transducer, which is not relevant for this experiment. To test the transducer performance prior to a SAW-AFM measurement, the IDT is commonly part of a delay line structure (consisting of two IDTs). As it is of interest to observe the emitted wave field without distortions by reflected wave components, the second transducer has to be made inactive by covering it with an acoustic absorber. The influence of reflections will be discussed in section 5.4.

For the measurement, the IDT was powered by an amplitude-modulated RF signal. The AFM tip was placed in the vicinity of the IDT's aperture. Figure 7 shows the topography and the corresponding, simultaneously recorded amplitude signal. The images were scanned with a resolution of 256×256 points at a frequency of 0.2 Hz per line. The aperture of the transducer is clearly visible in the lower lhs corner of the topography scan (a). The thickness of the metallization is 60 nm. The amplitude image (b) is dominated by a bright area stretching across the image, indicative of the propagating acoustic beam. The acoustic beam leaves the transducer well-focused and, following the beam over several millimeters, an increasing widening of the beam can be observed. Inside the IDT, the electrodes can be easily identified in the amplitude image too. The reason for this edge artifact at the edges of the electrodes is the temporary loss of vertical tip-sample coupling. It has to be noted that the non-trivial tip-sample coupling is preventing quantitative conclusions about the absolute amplitude values. Since, however, the amplitude dependences are continuous over a wide power range, a calibration is possible for obtaining relative amplitude distribution data.

Frequency response of acoustic transducers. The pronounced frequency selectivity of IDTs, which find their application as filtering devices in many applications, suggests an investigation of the SAW amplitude pattern as a function

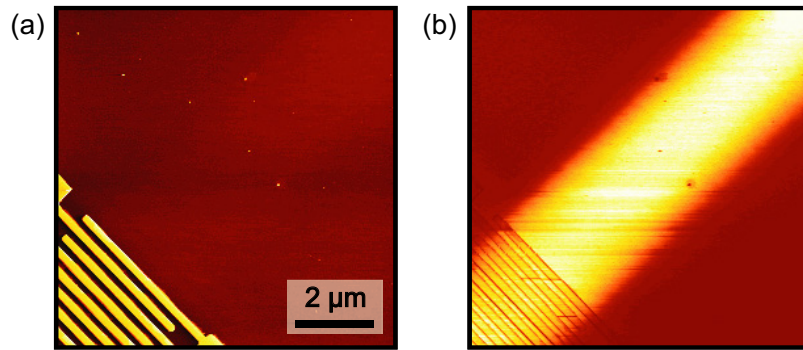


Figure 7. Acoustic beam imaging: (a) topography and (b) SAW amplitude image taken at the edge of an IDT. The electrodes of the IDT are visible in both images in the lower lhs corner. The amplitude image (b) shows the undisturbed SAW beam: bright = large amplitude; dark = low amplitude.

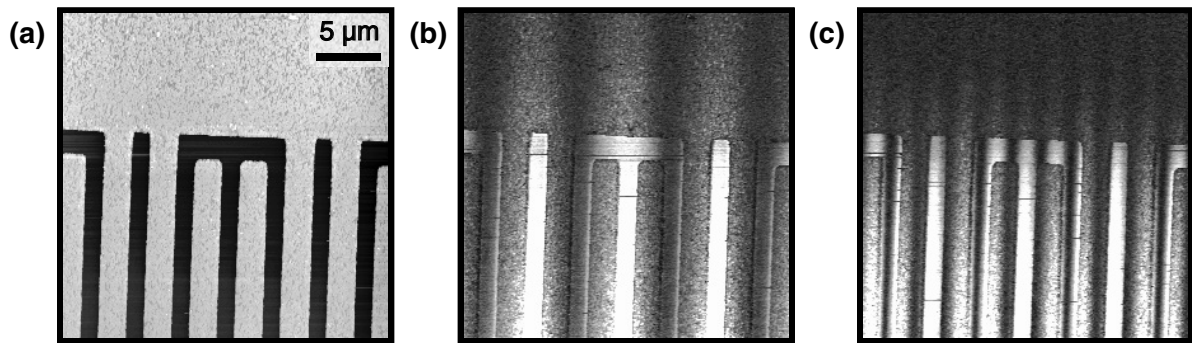


Figure 8. Standing wave field within an IDT: topography (a), SAW amplitude distribution at the fundamental frequency f_0 (b) and the 3rd harmonic ($3 \cdot f_0$) (c).

of frequency. This way, some of the fundamental characteristics of IDTs can be visualized. The first example is a delay line device where the fundamental frequency and its 3rd harmonic can be excited efficiently. The split-finger device was fabricated on GaAs for excitation at 200 and 600 MHz. The resulting SAW wavelengths for the fundamental and third harmonic modes are $14.4 \mu\text{m}$ and $4.8 \mu\text{m}$, respectively.

The topography and the SAW amplitude images obtained in amplitude mode, where one of the IDTs is driven with an amplitude-modulated signal, are shown in (figure 8). The investigated area is located exactly in the center of the device with respect to the propagation direction, and right at the device edge with respect to the perpendicular direction (cf (a)). The amplitude images in (b) and (c) show the typical behavior of a standing wave field, which is formed in the center of the IDT by the counter-propagating wave fields emitted from the individual electrode pairs. The expected period of the standing wave field of $\lambda/2$ is precisely reproduced ($7.2 \mu\text{m}$ (b) and $2.4 \mu\text{m}$ (c)).

The wave amplitude maxima are found to be between the fingers of identical polarity (cf (b)). As the SAW-AFM in the vertical deflection mode is primarily sensitive to the vertical oscillation component, the imaged maxima are those of the vertical oscillation component. For Rayleigh-type waves found in this system, the longitudinal oscillation component (i.e. the oscillation in the propagation direction) is phase shifted by 90° with respect to the vertical oscillation component. The longitudinal oscillation

component maxima—which are invisible for SAW-AFM operated in the vertical detection mode—are located between the electrodes of *different* polarities. This behavior is due to the fact that the electromechanical coupling in this case is facilitated by the longitudinal component of the wave, whose maxima are in the areas of high electric field strength, i.e. between fingers of different polarities [85].

For waves excited at the 3rd harmonic, the amplitude maxima are again found between electrodes of identical potential (cf (c)). Since the wavelength is shorter, only one third of the wave maxima are located between the electrodes of different potentials. Thus, the overlap between areas of high electric field strength and the longitudinal oscillation components is smaller by a factor of three, thereby reducing the effective electromechanical coupling. In the investigated device, this disadvantage is compensated for by optimizing the impedance matching. In general, however, the effective excitation of higher harmonics is limited by the continuously decreasing overlap between electric field and acoustic wave. Higher working frequencies can be realized by smaller structural feature sizes, resulting in smaller wavelengths. By employing electron beam lithography working frequencies in the range 6–25 GHz are easily achievable [86, 87].

To demonstrate the applicability of SAW-AFM for investigations at gigahertz frequencies, SAW delay lines were fabricated by electron beam lithography. The single-finger structures on GaAs have a structural feature size of 250 nm. The resulting wavelength for the excitation of Rayleigh waves

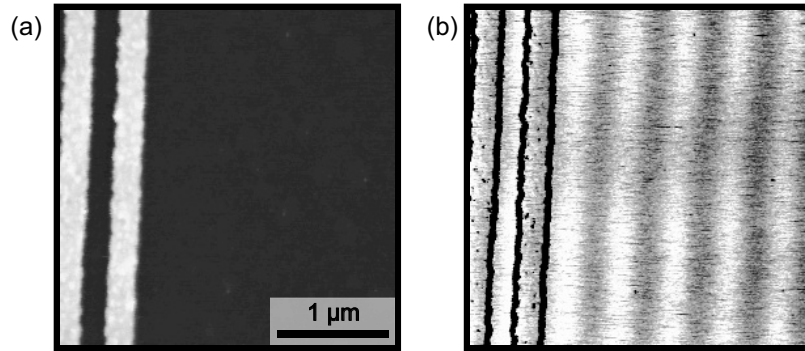


Figure 9. SAW amplitude measurement of a 2.975 GHz device structure. The topography image (a) shows two fingers of the unpowered IDT, which are also visible as artifacts in the amplitude image (b).

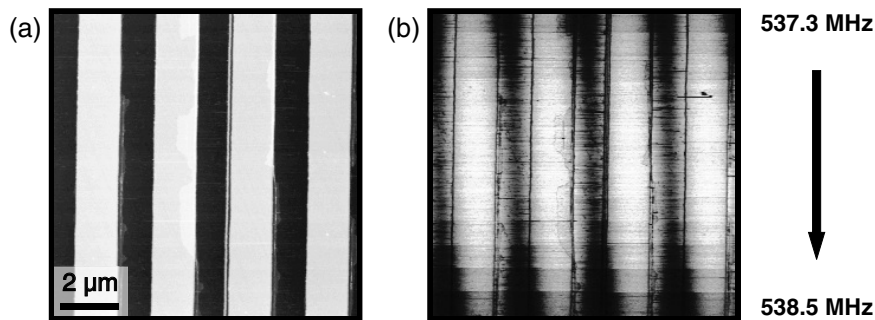


Figure 10. Frequency dependence of the standing wave field within a single-finger IDT: topography (a) and SAW amplitude distribution (b). The working frequency of the applied RF signal was tuned from 537.3 MHz (top) to 538.5 MHz (bottom).

of the 50-finger-pair IDT is thus $1\ \mu\text{m}$. The substrate orientation is the same as for the 540 MHz device. Two IDTs form a delay line with a peak transmission of $-30\ \text{dB}$ at an operating frequency of 2.975 GHz.

Figure 9 shows the amplitude image (b) and the corresponding topography (a). Here, only one IDT was powered, while the other one was acting as a reflector. The $3 \times 3\ \mu\text{m}^2$ scan area lies in front of the reflecting IDT. Thus, the imaged standing wave field is formed by the superposition of the incoming SAW with the reflected wave components. The standing wave field periodicity of $\lambda_{\text{SAW}}/2$ is clearly reproduced. An additional modulation is present in the vertical direction. This is due to deviations in the linear phase fronts, which are present close to the edge of the propagation path and the non-ideal characteristic of the reflector. Additionally, it is noteworthy that the maxima of the standing wave field pattern do not coincide with the positions of the electrodes of the reflecting IDT. This is due to the fact that the distance between the IDTs is not a precise multiple of the excited SAW wavelength.

The investigation of the SAW amplitude distribution inside an IDT during detuning of the applied RF signal is shown in figure 10. The single-finger transducer on GaAs was designed for a driving frequency of 538 MHz ($\lambda = 5.2\ \mu\text{m}$). The $15 \times 15\ \mu\text{m}^2$ scan was recorded at a scan rate of 0.4 Hz. The scan position was chosen to be at $3/4$ of the transducer length. The SAW amplitude distribution with excitation at a fixed frequency is homogeneous in the y -axis direction (not shown). Figure 10 shows the measured topography (a) along with the f -dependent SAW amplitude image (b).

While scanning (slow scan direction along the y -axis), the applied RF voltage was varied between 537.3 MHz (top) and 538.5 MHz (bottom) in steps of 100 kHz every 20 scan lines (256 line scan). The RF power at the generator output was kept unchanged. This frequency range covers roughly the passband of the IDT. It is obvious that the amplitude has its maximum in the middle of the image at this precise center frequency of the device (537.9 MHz). Here, the maxima of the standing wave field pattern coincide with the finger positions. It should be noted that for this propagation direction the vertical oscillation component is 90° phase-shifted with respect to the electrical potential of the SAW, which has its maximum in between the electrodes. This behavior is different from the one found for split-finger transducers, where electrodes have pairwise the same potential and the maxima of the electric field are as a result between two electrodes.

When the excitation frequency is deviating from the center frequency of the device, a linear shift of the positions of the amplitude maxima with frequency can be observed (figure 10(b)). Moreover, the amplitude signal is decreasing significantly. This effect is due to the developing mismatch between SAW wavelength and IDT periodicity, i.e. the positions at which the waves are excited no longer coincide with the amplitude maxima and the constructive interference pattern is lost.

4.2. Tip-sample force interaction

The quantitative investigation of the tip-sample interaction is challenging as many factors contribute that are in part difficult

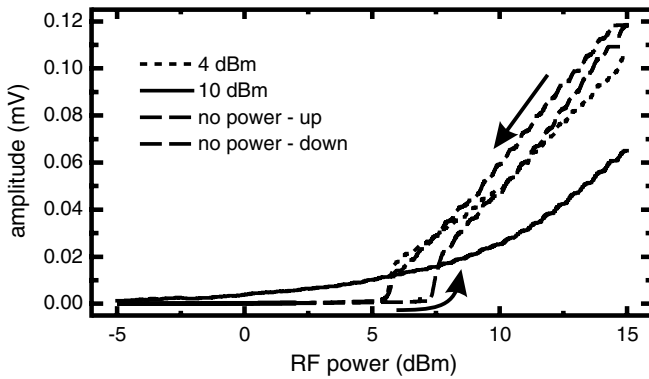


Figure 11. Amplitude dependence of the SAW-AFM signal: measured oscillation amplitude (y -axis) as a function of applied, amplitude-modulated RF power (x -axis). Without an additional unmodulated wave field ('no power'), a wave-induced jump of the working distance (\rightarrow *mechanical diode effect*) is observed. From [88].

to control (tip geometry, surface contamination). In SAW-AFM, the precise knowledge of the force curve is not required, as long as it is nonlinear. In this section, some aspects of the force curve will be highlighted.

Amplitude dependence of the mixing signal. The amplitude dependence of the static mixing term in SAW-AFM was investigated for 198 MHz Rayleigh waves on a GaAs substrate ($\lambda = 14.4 \mu\text{m}$). In the employed delay line structure, one IDT was powered with an amplitude-modulated RF signal ($\Delta f = 7 \text{ kHz}$), while the second IDT was optionally used to supply an unmodulated wave field, resulting in an oscillatory and a static contribution to the deflection signal, respectively. The contact mode AFM cantilevers had a spring constant of 0.25 N m^{-1} and their free resonance frequency was 30 kHz .

Figure 11 shows the vertical deflection signal as a function of the applied, amplitude-modulated RF power (from $-5 \rightarrow +15 \rightarrow -5 \text{ dBm}$). Three sets of data were obtained for an absent unmodulated wave field, and for additional unmodulated wave fields at $+4$ and $+10 \text{ dBm}$. This signal was obtained by the lock-in amplifier at Δf and it represents the oscillation amplitude of the tip. The measurement was performed at a fixed sample position with the sample oscillation amplitude being increased (decreased) in steps of $0.5 \text{ dBm}/10 \text{ s}$.

The behavior in the absence of an unmodulated wave field (dashed line, 'no power—up') is characterized by a small response for low applied power ($< 7 \text{ dBm}$). Once the threshold power of $+7 \text{ dBm}$ is reached, the signal shows a jump and increases logarithmically with power (logarithmic x -axis). Upon decreasing the driving power again (dashed line, 'no power—down'), the amplitude response is comparably large at and below the initial power threshold of $+7 \text{ dBm}$. This hysteretic behavior is rather typical for an oscillator with nonlinear restoring forces. In particular, an analogy with the so-called *mechanical diode effect* in UFM can be established [11]. In UFM, bulk waves are employed in the megahertz range with an acoustic modal structure that is different from SAWs. However, the qualitative behavior in

SAW-AFM and UFM is rather similar in the respect that a threshold power is observed and that the further increase in the response with power is logarithmic.

The explanation for this behavior can be found in the force–distance curve. The chosen set-point for the distance control in contact mode AFM defines a starting point which lies in the repulsive force regime. The surface oscillations are then modulating the distance between tip and sample. In the repulsive force regime, the force–distance curve is locally quite linear and relatively large amplitudes have to be applied in order to drive the system entirely into the nonlinear regime. Nevertheless, already average SAW amplitudes induce a small shift of the static force toward the attractive force regime. This is complemented by the fact that the surface oscillations lead to a 'sampling' of the force curve. If the sampled effective forces are including the minimum of the force curve where the nonlinearity is largest, the rectified force shows a jump of the set-point away from the surface.

In UFM, the jump of the set-point becomes visible by the additional static cantilever deflection. In SAW-AFM, this 'static' effect is made visible via the amplitude modulation—which leads to a similar characteristic of the SAW-AFM amplitude signal. For large SAW amplitudes, however, this analogy is no longer valid as also the cantilever oscillations at Δf are rectified. Therefore, a second, unmodulated wave field is excited at a power of $+4 \text{ dBm}$ (dotted curve) and $+10 \text{ dBm}$ (solid curve). For $+4 \text{ dBm}$, the onset of the hysteresis is shifted to lower modulated RF powers and the jump in the amplitude is becoming smaller, as the rectified static force component of the unmodulated field is shifting the set-point toward the force curve minimum. A similar effect is observed in UFM for a variation of the set-point force. At an unmodulated power of $+10 \text{ dBm}$, the jump has completely vanished and a continuous increase in the amplitude signal with applied power is observed. Please note that the observed maximum amplitude for $+10 \text{ dBm}$ is only half of that observed for the case of no additional wave field. This is a result of the unmodulated wave shifting the set-point to the vicinity of the force minimum—or even beyond. This effect has not been observed in UFM as there are no stable force feedback conditions for the required force values.

The tip–sample contact. One important property of the tip–sample contact is the appearance of the so-called contact resonance for external mechanical excitation. In principle, this is the modification of the cantilever resonance by the forces that act between tip and sample surface. In a simple picture, the contact can be viewed as an additional spring and a dashpot, which couples the tip to the surface. The value of the spring constant is given by the contact parameters (geometry, elastic constants).

To compare the results for low-frequency acoustic modes and SAWs, a series of mixing experiments were conducted for Si_3N_4 tips on quartz surface. Two excitation frequencies were chosen: a 400 kHz surface vibration excited by a bulk wave in the sample and 220 MHz SAWs. The excitation frequencies were slightly detuned from one another and the resulting cantilever oscillation signal at the difference frequency Δf

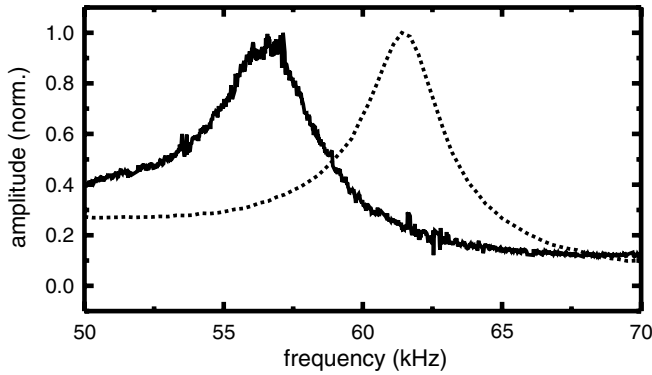


Figure 12. Cantilever resonance curves in contact with a quartz surface. Dotted line: 400 kHz bulk wave excitation, solid line: 220 MHz SAW excitation. From [88].

was measured with a lock-in amplifier. The reference signal was obtained by an external frequency mixer. The variation of Δf now allows for a selective excitation of the cantilever resonance. Figure 12 shows this resonance behavior for the tip in contact with the surface for both experimental configurations. The contact resonance is roughly a factor of 4 higher than the free resonance of the cantilever of 15 kHz. The measured resonance frequencies for both experimental configurations are not identical as two cantilevers had to be used (with slightly different mechanical parameters within the manufacturing tolerances). Nevertheless, the shape of the resonance curves (slightly asymmetric) and the broadening of the resonance peak are similar for both experimental configurations. This indicates that the tip–sample contact mechanics is generally the same for the frequency region between some 100 kHz to some gigahertz.

The investigation of the amplitude dependence of the acoustic mixing signals offers an elegant way to characterize the force–distance curve. In a simple approximation, the force–distance curve can be described in the repulsive regime by a power law. The static force term of the mixing products will then depend on the power law exponent n and other, unknown parameters. By analyzing how the individual contributions of the high-frequency surface oscillations sum up to the low-frequency cantilever vibrations, one can obtain the power law exponent n . To obtain n , the individual low-frequency oscillation amplitudes have to be set into relation with the summed amplitudes whereby the constants are canceled out [89]. The resulting implicit equations for n and the oscillation amplitude lead for the example of Si_3N_4 cantilevers on quartz to a value of $n = 1.5 (\pm 0.5)$ under ambient conditions. This is the exponent one would expect from an ideal Hertzian contact. Different values are found for measurements under reduced humidity conditions.

5. SAW-AFM—phase detection

The precise measurement of the SAW's phase velocity gives access to the elastic properties of the wave-carrying film–substrate system [90]. SAWs are especially suited

for the determination of the elastic properties of thin films and layered structures [91]. Common SAW excitation and detection schemes, such as optical techniques, have the critical disadvantage of diffraction-limited lateral resolution. SAW-AFM, on the other hand, has in principle the same, nanometer-scale lateral resolution as conventional atomic force microscopy [92].

5.1. Phase velocities on the nanoscale

Figures 13(a) and (b) show two examples of the SAW-AFM phase measurements of Rayleigh waves on GaAs ($f = 538 \text{ MHz}$, $\lambda = 5.2 \mu\text{m}$). For phase measurements, both transducers are actively powered at two slightly detuned frequencies f and $(f + \Delta f)$ with $\Delta f = 5 \text{ kHz}$. A third, phase-locked low-frequency generator delivers the reference signal at Δf for the lock-in amplifier. To obtain a useful signal-to-noise ratio, the time constant of the lock-in amplifier was set to 1–10 ms (typically 3 ms). The scan frequency was typically between 0.1 and 0.4 Hz.

The investigated $10 \times 10 \mu\text{m}^2$ area presented in figure 13 is located right in the middle of the delay line, slightly rotated with respect to the k -vector of the SAW. The linear SAW phase is mapped onto the 360° range of the lock-in amplifier, resulting in phase jumps. The lines of constant phase are along these discontinuities and perpendicular to the propagation direction of the SAW. Since the aperture of the IDTs is large compared with the mapped area dimensions, the phase images are homogeneous and the waves can be treated as plane waves. The cross-sections through the phase images show that the phase delay is almost linear between the phase jumps (figure 13(c)). The propagation-dependent phase slope has a value of $(2 \cdot k)$. At Δf , the phase jumps occur with a period of $\lambda/2 = 2.6 \mu\text{m}$ ($k = 2\pi/\lambda$). As the frequency is known very precisely, the phase velocity of the wave can be determined with great precision and high lateral resolution by measuring the local slope of the SAW phase signal [93].

The measurement at $(2\Delta f)$ delivers a much smaller signal as it is due to a 4th order mixing term (cf figure 13(b)). The phase signal as a function of propagation distance is given by $4 \cdot |\vec{k}|$, which was confirmed in the experiment: $\lambda/4 = 1.3 \mu\text{m}$ (cf dashed line in figure 13(c)). Higher multiples of Δf are very difficult to detect.

Figure 14(a) shows a $60 \times 60 \mu\text{m}^2$ scan of the linear phase delay for a $93 \pm 4 \text{ nm}$ thick Au layer on ST-X quartz. The scan window is again slightly rotated with respect to the wave vector. The inset (figure 14(b)) shows a $5.1 \times 5.1 \mu\text{m}^2$ zoom of a phase jump. The stability of the phase measurement reaches almost single pixel resolution. The phase velocity that can be extracted from averaging over the phase jumps is $v = 2989 \pm 10.3 \text{ m s}^{-1}$ (cf line scans in (c)). Since the phase velocity can be defined as the phase variation as a function of propagation length, the velocity can be measured on scales much smaller than the SAW wavelength. For a lateral distance of $\Delta x = 19.9 \text{ nm}$ the phase variation $\Delta\varphi = 1.110^\circ$ was determined leading to a SAW phase velocity of 2827 m s^{-1} . Compared with 2989 m s^{-1} obtained for the $60 \mu\text{m}$ scan, the deviation is about 5.4%. This can be due to locally varying elastic constants or a result of

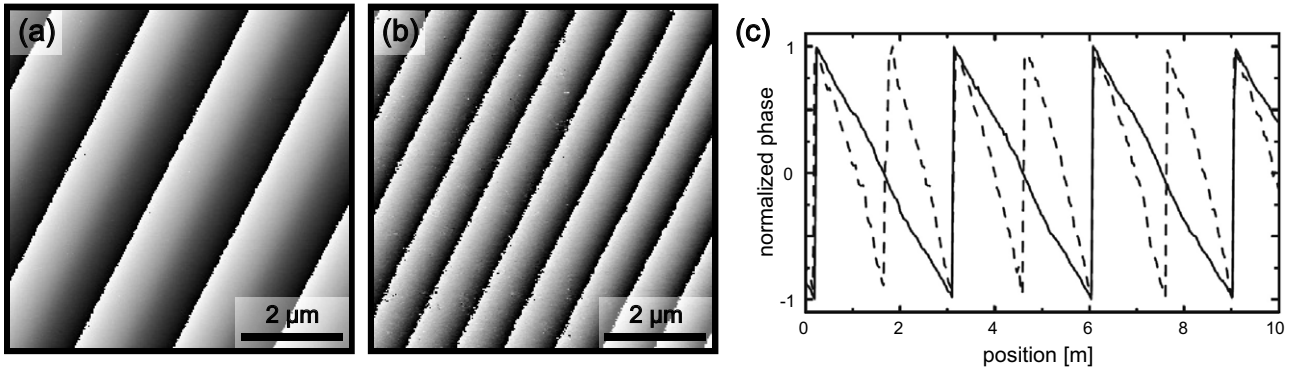


Figure 13. SAW-AFM phase images obtained on a 538 MHz delay line structure on GaAs at Δf (a) and $(2\Delta f)$ (b). The corresponding line scans are shown in (c) for Δf (solid line) and $(2\Delta f)$ (dashed line). Please note that the scan window is not aligned with the propagation direction of the SAW.

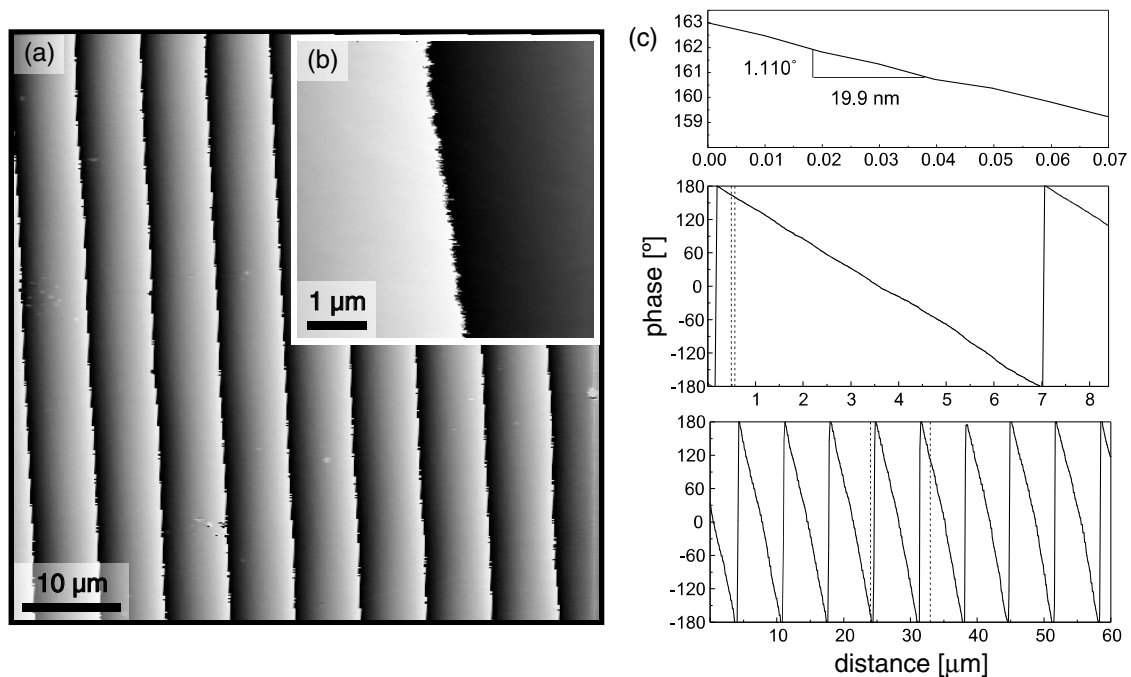


Figure 14. High-resolution SAW-AFM phase measurement (a). The inset (b) shows details of a phase jump demonstrating the stability of the phase measurement. Line scans (c) present scans over 60 μm (below), 8.4 μm (middle) and 70 nm (top). The dotted lines mark the lateral positions where the zooms were obtained.

topographic variations that lead to artifacts in the phase image. As known from SAW-STM imaging, a detailed knowledge of the topography is needed to separate phase artifacts from true elastic inhomogeneities. It has to be noted that the scanner resolution is limited by the noise of the high-voltage amplifiers and can be in modern positioning systems as low as 25 pm [94].

5.2. Measurement of in-plane polarized waves

Phase measurements on SAWs are not limited to waves with an out-of-plane oscillation component [95]. Especially purely in-plane polarized SAW modes have attracted a great deal of attention in the past years since these transversal [96] or quasi-longitudinal [34] modes have a factor of two higher phase velocity than Rayleigh waves on the same materials system.

This way, larger structural feature sizes are acceptable for high-frequency operations, thus cutting the device fabrication costs. Moreover, the measurement of more than one acoustic mode is necessary for the precise determination of elastic constants. The main challenge with in-plane waves is their detection, as common methods often rely on a non-vanishing out-of-plane oscillation component. Laterally resolved imaging of in-plane modes was for the first time possible with SAW-AFM.

Transversally polarized modes were excited on Au/SiO₂ on quartz. On ST-quartz, Rayleigh waves can be excited in the crystalline X -axis direction and a transversally polarized pseudo-SAW (surface transverse wave—STW) in a 90°-rotated direction. The STW converts into a Love wave if the substrate is covered by a layer with lower bulk wave velocity. The film material of choice is SiO₂, as high quality films can be easily sputtered onto a quartz surface [97]. Since

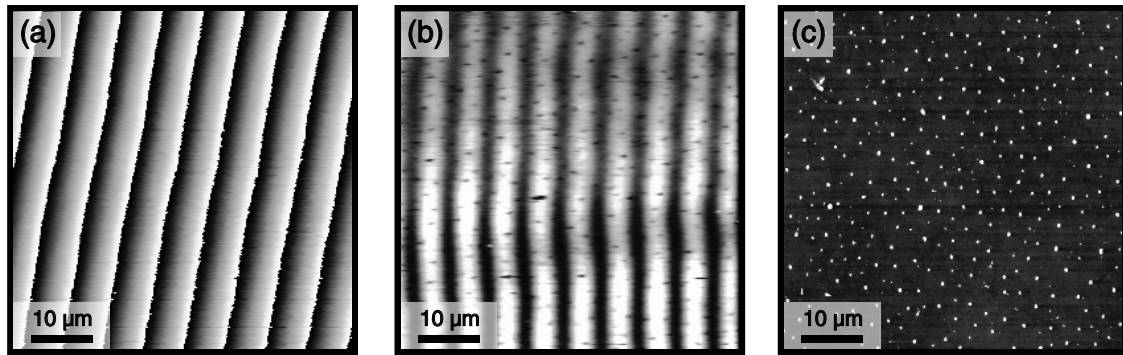


Figure 15. SAW-AFM investigation of Love waves. Phase image (a), amplitude distribution of the standing wave field (b) and corresponding topography (c). In contrast to conventional SAW-AFM, the torsional oscillation modes of the cantilever were analyzed which are superimposed onto the frictional LFM signal.

stoichiometric SiO_2 is an insulator it can be sputtered over the whole device, which simplifies the fabrication process. Love waves are transversally polarized true SAWs, which were originally discovered in the context of earthquake research [98]. They are also of great importance for liquid sensor applications [99], since their propagation is not damped at the liquid–solid interface by the excitation of shock waves into the liquid.

The operating frequency for exciting STWs with $\lambda = 14.4 \mu\text{m}$ is 349 MHz. By covering the whole device with a 600 nm thick SiO_2 layer, Love waves can be excited and the frequency shifts to 340 MHz. In the center of the structure, a 40 nm thick gold pad was fabricated to study the dispersion of the waves. The IDTs of the delay line were operated at their center frequency f and $(f + \Delta f)$ with $\Delta f = 5 \text{ kHz}$. Since vertical deflection SAW-AFM is by a factor of 10 less sensitive toward in-plane oscillations, the LFM signal (torsional cantilever oscillations) is used instead (SAW-LFM). In order to increase the sensitivity toward torsional oscillations, very thin and soft cantilevers were employed.

Figure 15(a) shows a $55 \times 55 \mu\text{m}^2$ SAW-LFM phase image of the gold pad. Analogous to the phase image, a SAW-LFM amplitude image is obtained (b) that yields a standing wave field. The topography (c) shows a number of surface defects (bright) that appear as dark spots in the amplitude image. The phase image, however, is not affected by these defects. Inhomogeneities in the elastic properties of the gold layer, on the other hand, lead to a slight deformation of the phase fronts in (a). The phase slope yields a SAW wavelength of $13.3 \mu\text{m}$ and, with a SAW frequency of 340 MHz, a phase velocity on the gold pad of 4520 m s^{-1} . The velocity on the free surface can be estimated by the electrode period and the frequency to 4900 m s^{-1} .

The existence of a mechanical coupling mechanism between in-plane surface oscillations and the torsional movement of the cantilever appears trivial at first sight. However, two important inconsistencies are evident when taking a closer look. First, the mixing signal vanishes when the scan is interrupted. This is not the case for the vertical detection of Rayleigh waves. Second, the LFM-detected mixing signal vanishes when the torsional axis is parallel to the propagation direction of the wave. In this constellation, the maximum

contrast should be expected as the surface oscillation is exactly in the direction of the torsional movement (on the surface). A detailed explanation of the origin of the torsional coupling is given in section 8.

High-velocity modes. Besides the transversally polarized pseudo-SAWs (PSAWs), quasi-longitudinally polarized PSAW modes are promising candidates for high-frequency device applications due to their very high phase velocities. These so-called high-velocity pseudo-SAWs (HVPSAWs) are surface modes with a strong bulk character [34], and they have therefore a rather large propagation damping and show strong beam-steering effects. In order to find useful HVPSAW materials, intense numerical studies are required [100, 101]. Since there is a lack of suitable characterization tools for in-plane modes, only very few experimental studies of HVP-SAWs were published (transmission line measurements [102]) before the initial SAW-AFM experiments [103].

Figure 16 shows a SAW-AFM phase measurement of a HVPSAW on $\text{SiO}_2/\text{quartz}$, and for comparison, a Love wave. The images were obtained in the SAW-LFM mode. The same basic IDT structure with $\lambda = 14.4 \mu\text{m}$ is used such that the different phase velocities lead to different operating frequencies. The goal of this study was to prove the existence of HVPSAWs by a method different from the direct electric measurement. First, numerical studies have been conducted for the common materials and cuts. For ST-cut quartz, a HVPSAW was predicted under 0° , i.e. in the direction of the common Rayleigh wave [104].

The prominent property of HVPSAW modes is their large penetration depth of up to several 100λ . Figure 16(c) proves the decay behavior of the longitudinal oscillation component of a HVPSAW on ST-quartz (oscillation component u_1) by numerical simulations. As only a fraction of its energy is confined at the surface, SAW-AFM detection is impossible. Nevertheless, HVPSAWs are very sensitive to cover layers such as SiO_2 . Numerical investigations for increasing Al cover layer thicknesses have shown that the HVPSAW first converts into a PSAW and then into a higher order SAW mode while the wave is increasingly confined at the surface [104].

Numerical investigations of a 200 nm thick SiO_2 layer on ST-X quartz show a penetration depth which is by an order of magnitude smaller compared with the blank surface

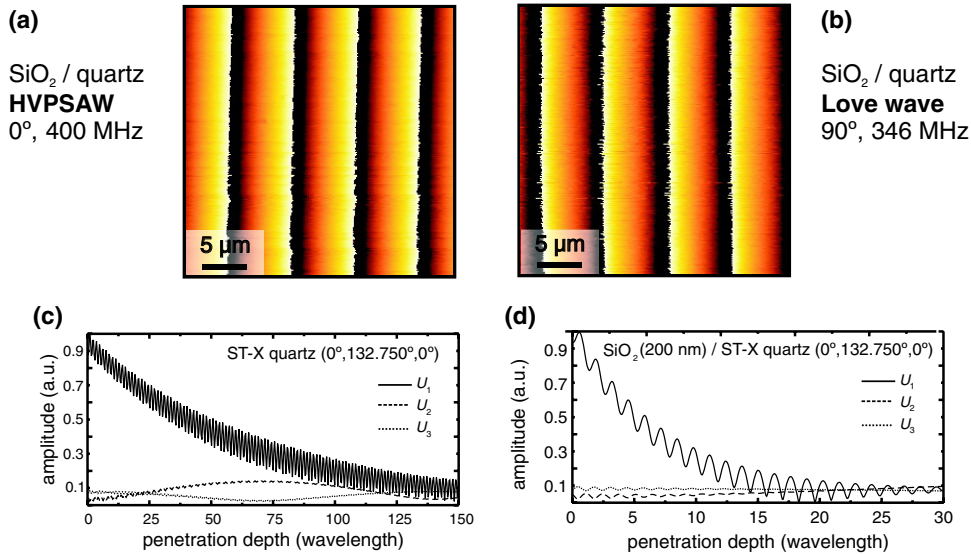


Figure 16. SAW-AFM phase measurement of high-velocity SAW modes. HVPSAW on quartz (a). For comparison, the phase measurement of a Love wave sample is shown in (b). (c) and (d) show the depth dependence of the oscillation amplitudes on blank and SiO₂ covered ST-X quartz. From [88].

(cf figures 16(c) and (d)). On such a materials system, SAW-AFM phase measurements can be carried out (a). Since the longitudinal bulk wave and the HVPSAW have almost identical velocities in the investigated direction, electric transmission measurements cannot distinguish between the two. Nevertheless, the measurement of the wave parameters by SAW-AFM as a function of cover layer thickness will allow one to identify the surface-confined mode quite easily. Indeed, this way the existence of a HVPSAW on ST-quartz could be confirmed.

5.3. Investigation of non-collinear waves

So far, the presented SAW-AFM investigations were limited to collinear geometries, in which commonly only a single acoustic mode can be excited. For determining the elastic parameters of thin films, however, it is necessary to include several modes—ideally all measured simultaneously. As mentioned above, back reflections are a limitation of collinear excitation geometries. Both problems can be solved simultaneously by exciting the waves along *different* directions in a non-collinear geometry [105]. A very simple system for the demonstration of the principle is a crossed delay line on GaAs(001). Owing to its four-fold symmetry, identical waves can be excited in directions 90° with respect to each other. For the common case of the [110]-propagation direction, a Rayleigh wave with a velocity of 2850 m s⁻¹ is excited. With $\lambda = 14.4 \mu\text{m}$, the center frequency is $f = 198 \text{ MHz}$.

Figure 17(a) shows the crossed arrangement of the two delay lines. For the wave field excitation, IDTs 1 and 4 were powered by RF generators at f and $(f + \Delta f)$ with $\Delta f = 5 \text{ kHz}$. The SAW-AFM phase image of the crossed beams is shown in (b). The $50 \times 50 \mu\text{m}^2$ large scan field was perfectly aligned with the transducer edges. The phase fronts appear rotated by an angle of 45°, which is a result of the influence of the two k -vectors on the phase signal. For the

general case of two crossed SAWs follows:

$$S = \sin[(\omega_1 - \omega_2) \cdot t + \vec{k}_1 \vec{r}_1 - \vec{k}_2 \vec{r}_2]. \quad (5.1)$$

In the present case, the wave propagation is chosen to be along the x - and y -directions. As the magnitudes of \vec{k}_x and \vec{k}_y are identical, it follows: $S = \sin[\Delta\omega \cdot t + k(x - y)]$. As a consequence, the phase image again shows a linear spatial dependence and the phase slope is given by the k -vector. Since both k -vectors have the same magnitude, the phase fronts ($\lambda = 14.4 \mu\text{m}$) are exactly rotated by 45° with respect to the propagation directions. The minimum distance between the phase fronts is thus $(1/\sqrt{2}) \cdot 14.4 \mu\text{m} = 10.2 \mu\text{m}$. The sign of the phase is different in both directions, i.e. the phase decreases in the x -direction and increases along the y -direction. This behavior is inverted when the working frequencies are switched [$f \leftrightarrow (f + \Delta f)$].

Simultaneous measurement of Rayleigh and Love waves. An ideal materials system for demonstrating the mixing of *different* acoustic modes is SiO₂/quartz. As mentioned above, the ST-cut quartz surface allows for the excitation of a Rayleigh wave (0°-direction) and a Love wave (90°-direction) (cf figure 18(a)). In this setup, a thin film material can be characterized by placing it in the intersection of the two SAW beams [106]. Both SAWs exhibit a different phase velocity: $\sim 3160 \text{ m s}^{-1}$ for the Rayleigh wave and $\sim 4990 \text{ m s}^{-1}$ for the Love wave (function of the film thickness). Consequently, different IDTs have to be used. The Rayleigh wave IDT was designed with a structural feature size of $0.7 \mu\text{m}$, resulting in a wavelength of $5.6 \mu\text{m}$ ($f = 563 \text{ MHz}$). The Love wave IDT has a structural feature size of $1.1 \mu\text{m}$, which gives a wavelength of $8.8 \mu\text{m}$ ($f = 569 \text{ MHz}$), which is some megahertz higher than the Rayleigh wave frequency. As both modes have a different velocity dependence on cover layer thickness, a thin SiO₂ layer was deposited in order to match both frequencies. Figure 18(b) shows the dependence of the

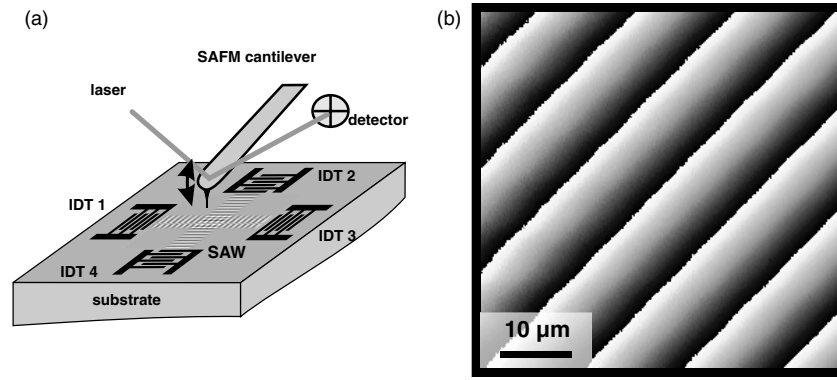


Figure 17. SAW-AFM phase measurement of crossed Rayleigh wave fields. (a) Schematic of the experimental setup. (b) Phase image.

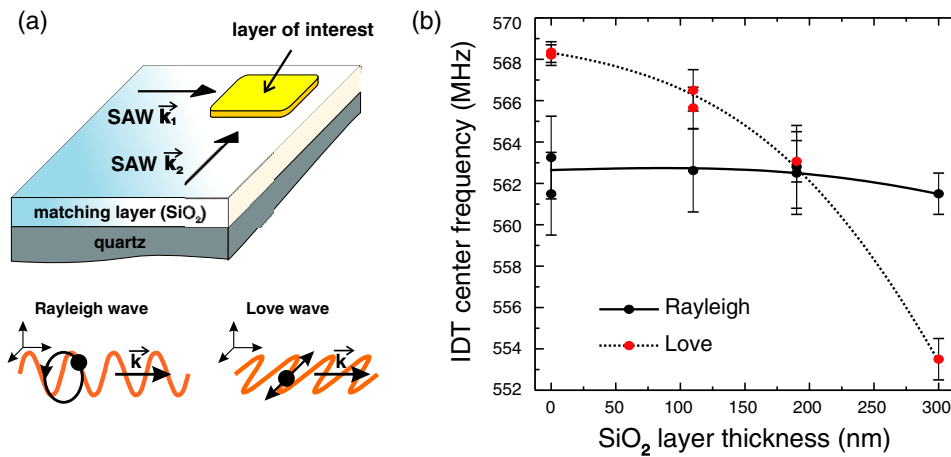


Figure 18. (a) Sample design for the simultaneous excitation of Rayleigh and Love waves at identical frequencies. On ST-quartz, Rayleigh and Love waves can be excited under an angle of 90° . (b) By employing a SiO_2 cover layer, the frequency difference between the two waves that is present on the bare substrate can be reduced to the kilohertz range—allowing for SAW-AFM mixing experiments.

two center frequencies as a function of SiO_2 film thickness. For a thickness of 190 nm, a sufficient agreement of both frequencies is reached ($f = 563$ MHz), corresponding to phase velocities of 3150 and 4950 m s^{-1} for the Rayleigh and Love waves, respectively.

The generalization of the expression for the SAW-AFM phase signal for two modes is

$$S = \sin[\Delta\omega \cdot t + k_{\text{Rayleigh}} \cdot x - k_{\text{Love}} \cdot y]. \quad (5.2)$$

Again, the wave propagation is assumed along the x - and y -directions. As a result of the different phase velocities, different phase slopes can be expected in the x - and y -directions. The resulting phase fronts will thus appear under an angle that is characteristic for the ratio of the two velocities.

Figure 19(a) shows the simulation of the SAW-AFM phase for Rayleigh and Love waves with wavelengths of 5.6 μm and 8.8 μm , respectively. In (b), experimental data for a working frequency of 562.7 MHz are shown. The simple linear model describes the experimental result sufficiently well. The top transducer was used to excite the Love waves, while the Rayleigh waves were launched by the rhs transducer. The frequency difference between the excitation frequencies was 5 kHz. The mixing signal was detected by vertical mode SAW-AFM, since the Rayleigh wave-related

signal was very strong and the in-plane oscillation was made visible by the in-plane coupling mechanism (for details, see section 8).

The experimental data are processed by removing the phase jumps from the images and by fitting the resulting plane using the x - and y -axis slopes as fitting parameters. From figure 19(b), wavelengths of 5.5 and 9.1 μm , and consequently phase velocities of 3090 and 5120 m s^{-1} , were extracted, which deviate clearly from the expected values. By correcting the rotation of the measurement area with respect to the transducer edges (1.3°), velocities of 3140 and 4940 m s^{-1} are obtained which agree well with the expected values within the measurement error of $\sim 1\%$. In order to achieve a useful precision, the misalignment angle has to be determined very carefully. Note that an unintentional misalignment of only 1° already leads to a deviation of 50–100 m s^{-1} in the phase velocity.

Investigation of elastic film parameters. The goal of the methodological developments presented in this section is the determination of the elastic parameter and the investigation of their local variation [103]. For the visualization of elastic contrast, a Love wave sample was coated with a 60 nm thick Au pad. The topography (figure 20(a)) shows the metal film as a bright area (on the rhs). The edge is rotated by $\sim 7^\circ$

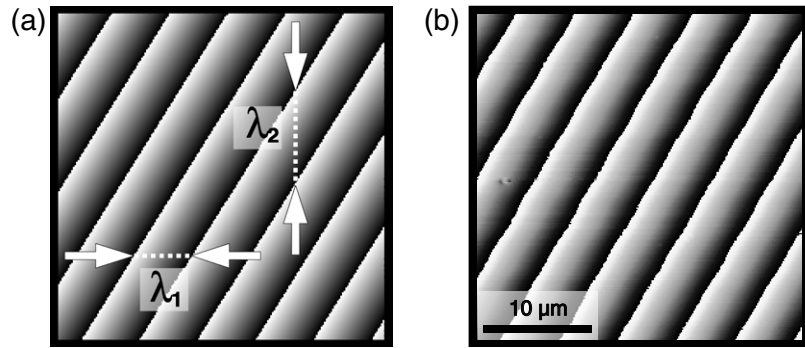


Figure 19. Simultaneous SAW-AFM phase measurement of Rayleigh and Love waves in the materials system SiO_2 (190 nm)/ST-quartz at 563 MHz: simulation (a) and measurement (b). The orientation of the scan is perfectly aligned with the propagation directions of the two SAWs. The arrows in (a) illustrate the different periodicities of the phase jumps in the two propagation directions. From [88].

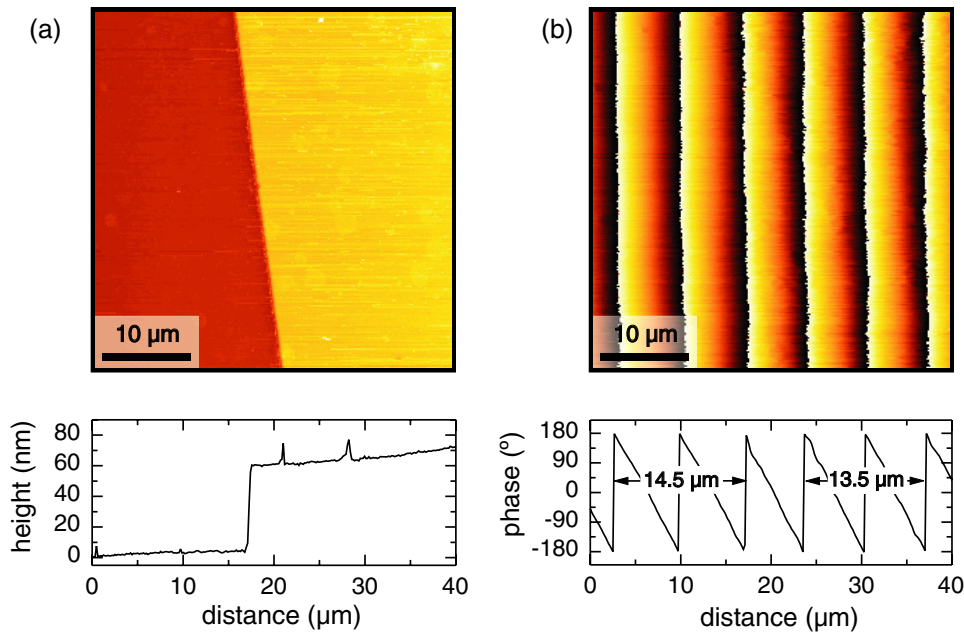


Figure 20. Elastic contrast of a Au pad: (a) topography and (b) phase image. As can be seen from the phase cross-section below, the wavelength on the Au pad is about $1 \mu\text{m}$ smaller than on the uncovered substrate.

with respect to the propagation direction of the waves. The linescan below shows the abrupt film edge (height 60 nm). The SAW-AFM image (b) was obtained in conventional collinear geometry using the torsional detection scheme (LFM signal). Looking in detail at the phase image, different slopes are obvious for the free surface and on top of the metallized pad. The different wavelengths of $14.5 \mu\text{m}$ and $13.5 \mu\text{m}$ correspond to phase velocities of 5000 m s^{-1} and 4700 m s^{-1} , respectively. The change in phase velocities is discontinuous across the edge.

By measuring the phase velocity of both wave types, assuming known values for the thickness and density of an isotropic layer, the remaining two elastic constants can be determined. In the presented model system on ST-quartz, the SiO_2 layer is 545 nm thick (density 2.52 g cm^{-3}). Using a numerical method for solving the inverse problem [36], the resulting values for the elastic modulus and the Poisson ratio are $E = 68 \text{ GPa}$ ($\pm 5\%$) and $\nu = 0.27$ ($\pm 10\%$), respectively [107]. Both values are in reasonable agreement with the strongly scattering reference values [108].

5.4. Distortions and nonlinear effects

Distortions and nonlinear effects are limiting the precision with which the phase velocity can be determined. Ideally, the precision is only limited by the accuracy of the length measurement. In reality, there are a number of physical effects that compromise the linearity of the phase signal, such as edge effects and roughness, electromechanical mixing, undesired wave reflections and electric cross-talk. The most prominent effects are the latter two, whereby the cross-talk becomes more of an issue for higher frequencies. In any case, a properly shielded sample setup and optimal matching between generator and device is essential. Back reflections can be avoided in non-collinear transducer geometries.

Undesired wave reflections and electric cross-talk both lead to the presence of additional waves in the investigated region and can thus be discussed together. In the case of a collinear arrangement of the IDTs, wave reflections originate from both direct mechanical wave reflections, as well as an intermediate electric signal generation and re-emission of a

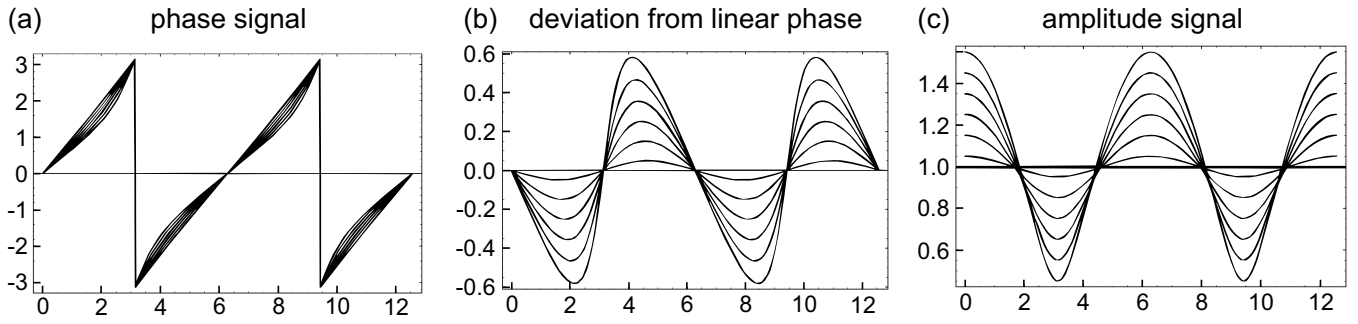


Figure 21. Effects of undesired wave reflections and electric cross-talk on the SAW-AFM signals: simulated phase (a), deviation from the linear phase behavior (b) and (induced) amplitude signal (c). The curve parameter is the amplitude of the distortion in relation to the primary signal (0–0.5 : 1). From [88].

secondary wave. Direct electric cross-talk, on the other hand, leads to the emission of secondary SAWs by the reception of RF signals from the primary IDT.

Apart from the initially excited waves at the frequencies f_1 and f_2 and the k -vectors k_1 and k_2 , additional waves with considerably reduced amplitude exist with k -vectors $-k_1$ and $-k_2$. The quadratic mixing term now delivers four terms at the difference frequency Δf by combination of these components:

$$S = a_1 \sin[\Delta\omega t + 2kx] + a_2 \sin[\Delta\omega t + \Delta kx] + a_3 \sin[\Delta\omega t - \Delta kx] + a_4 \sin[\Delta\omega t - 2kx]. \quad (5.3)$$

The last term is the mixing product of the small, reflected components. Its presence was not detected, although it gives rise to a very characteristic double period. The two middle terms show, in principle, no spatial variation, since the difference in the magnitude of the k -vectors is negligibly small. They can thus be summarized as a constant phase contribution. Its influence becomes clear when looking at the SAW-AFM phase simulations. As discussed earlier, no useful phase information is contained in the SAW-AFM phase signal when more than one component contributes to the contrast. Nevertheless, a phase can be formally defined and detected by the lock-in amplifier. Figure 21(a) shows the expected phase signal for varying distortion amplitude. The distortion amplitude was increased from 0% to 50% of the primary signal amplitude. In principle, the sawtooth-like appearance of the phase signal remains intact; however, in detail, the deviation from the linear behavior is significant. In (b), the linear phase slope has been subtracted and only the deviation from the linear phase is shown.

Another important consequence is illustrated in figure 21(c). The amplitude of the oscillation signal at Δf is constant for the mixing of two waves. By adding a spatially constant phase term to the phase signal, the amplitude of the total signal becomes position dependent, since the signals add up alternately in-phase and out-of-phase. The result is a standing wave-like contrast in the amplitude signal. This means that the appearance of a signature in the amplitude image in SAW-AFM mixing experiments is a proof of the existence of (unwanted) spurious reflections and cross-talk.

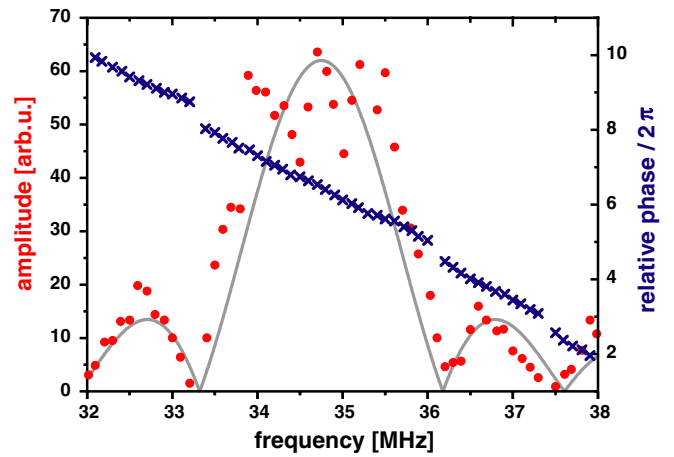


Figure 22. SAW-STM measurement of an IDT passband curve ($f_0 = 34.8$ MHz): Amplitude (red circles) and relative phase (blue crosses).

6. SAW-STM—‘seeing’ atoms oscillate

The investigation of ultrafast phenomena by scanning probe microscopy [109] can be achieved with AFM [110]; however, the more flexible tool with an inherent faster response time is scanning tunneling microscopy (STM) [111–115]. In this section, SAW-STM amplitude and phase measurements will be discussed that show how oscillations on an atomic scale affect the STM contrast. Finally, a fascinating insight into an oscillating atomic lattice will be given.

To prove the SAW detection capabilities, the frequency-dependent IDT characteristics were investigated by placing the (non-scanning) STM tip within the metallized cavity of a delay line structure. A dual-channel oscilloscope was used to record the phase and the amplitude at the difference frequency.

The amplitude (figure 22, lhs ordinate) reproduces the expected passband curve. The relative phase (rhs ordinate) shows a linear behavior over frequency. It is in general more stable than the amplitude. With the known distance between the measurement point and the IDT center ($x = 4383 \pm 10 \mu\text{m}$), as well as the gradient of the (linear) phase curve ($d\varphi/df = 6.980 \pm 0.087 \text{ MHz}^{-1}$), the SAW velocity can be calculated to $v = 2\pi x \cdot df/d\varphi = 3944 \pm 49 \text{ m s}^{-1}$, which is in good agreement with the calculated value of $v = 3955 \text{ m s}^{-1}$ [116].

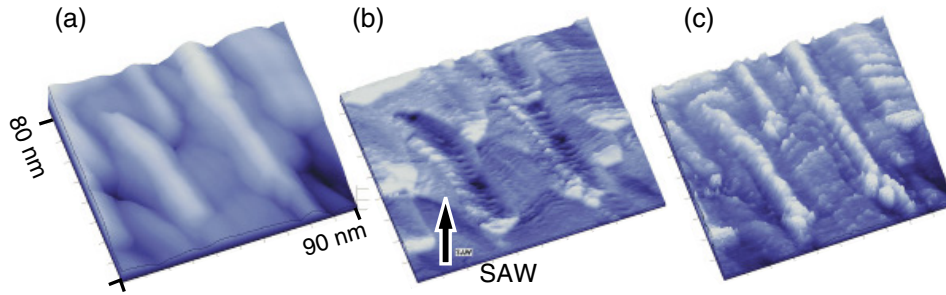


Figure 23. SAW-STM topography (a), phase (b) and amplitude (c) images of a corrugated Au surface. The SAW propagation direction was slightly inclined with respect to the elongated Au grains.

6.1. Contrast model

The first SAW-STM measurement on a corrugated Au surface showed phase and amplitude images that exhibited unexpected details which are correlated with the measured topography (see [117]; similar to figure 23). At first sight, however, the measured phase signal should reflect the linear SAW phase delay with increasing distance from the IDT, and the amplitude signal on that scale should be simply constant. In this subsection, it will be shown how the phase and amplitude contrasts are influenced by the topographical features.

Topographical contrast enhancement. In order to enhance the contrast in STM measurements in noisy environments, phase-sensitive techniques have been introduced for obtaining differential surface topography data [118]. For this purpose, the piezo-position is modulated with a frequency that is higher than the response frequency of the control circuit. From the measurement of the differential topography, the real topography can be reconstructed [119].

SAWs propagating along the surface force the surface atoms to oscillate on elliptical trajectories. In other words, the SAW leads to a dithering in the propagation direction, and in the vertical direction, with respect to the mean tip position. The SAW-STM measurement of a corrugated Au surface is presented in figure 23. The $90 \times 86 \text{ nm}^2$ topography scan (a) shows grains with a typical length of some 10 nm and a width of 15–20 nm. The simultaneously measured phase (b) and amplitude (c) clearly reveal steps and grain boundaries which cannot be seen in the native topography image. Furthermore, it has to be noted that the contrast is quite different for amplitude and phase and the grains appear to be ‘illuminated’ from different directions.

The grains appear smooth in the topography image; however, the phase image clearly resolves a stepped terrace structure on and between the grains. The steps have a separation of $\approx 2 \text{ nm}$. The phase image exhibits the largest contrast in the direction parallel to the wave propagation direction. Consequently, the resolution of the details of the grain structure depends on the relative orientation of the grains with respect to the wave propagation direction. In contrast to the phase signal, the main amplitude contrast is in the perpendicular direction. Moreover, the amplitude signal is more noisy.

In an STM, SAWs propagating along the surface of a solid strongly affect the tunneling current by modulating

the tunneling distance. SAW frequencies pose in general a problem for the bandwidth-limited electronics of a commercial STM (100 kHz). However, with the tunneling current being nonlinearly dependent on the tip–sample distance, the heterodyne detection scheme can be applied. Different from SAW-AFM where a mechanical trigger close to the SAW frequency is needed as a reference signal, an electrical solution can be easily implemented. The SAW-assisted tunneling process will be described by a one-dimensional model below. This is sufficient for a basic understanding of SAW-STM, since the major part of the tunneling current flows normal to the sample surface along the shortest path [120]. For a more rigorous treatment see [121, 122].

Flat surface model. In the case of corrugated surfaces, the tunneling current path is not necessarily parallel to the film normal and the local topography (slope) will affect the tunneling signal. The time-dependent tip-to-sample distance d is now made up of the undisturbed tip-to-sample distance d_0 , as given by the static tunneling parameters, and an oscillating component due to the SAW at the frequency ω_1 :

$$d = d_0 + d_1 \sin(\omega_1 t + \varphi), \quad (6.1)$$

where d_1 is the normal amplitude and φ the local phase of the SAW with $\varphi = 2\pi x/\lambda$ (x is the distance in the propagation direction and λ the SAW wavelength). The reference or clock frequency which is needed for the heterodyning technique is applied as a high frequency voltage at a frequency ω_2 across the tunneling gap, in addition to the static gap voltage U_0 :

$$U = U_0 + U_1 \sin(\omega_2 t), \quad (6.2)$$

with U_1 the amplitude of the clock voltage.

Inserting equations (6.1) and (6.2) in the expression for the tunneling current density $j = e^2/(2\pi h) \cdot U/d \cdot \kappa \cdot \exp(-2\kappa d)$ [123], with $\kappa \approx 2\pi/h \cdot \sqrt{2m\phi}$ the reciprocal decay length of the electron wave function, yields the normalized tunneling current density:

$$\frac{j}{j_0} = \frac{1 + U_1/U_0 \sin(\omega_2 t)}{1 + d_1/d_0 \sin(\omega_1 t + \varphi)} \exp[-2\kappa d_1 \sin(\omega_1 t + \varphi)]. \quad (6.3)$$

$j_0 = j(U = U_0, d = d_0)$ is the undisturbed tunneling current density.

In the case of typical SAW amplitudes, where d_1 is small compared with the undisturbed tunneling distance d_0 , $d_1/d_0 \ll 1$, j/j_0 can be expanded and recondensed to:

$$\begin{aligned} \frac{j}{j_0} = & P_{00} + P_{01} \sin(\omega_2 t) + P_{10} \sin(\omega_1 t + \varphi) \\ & + P_{11}^{\pm} \cos[(\omega_1 \pm \omega_2)t + \varphi] \\ & + \dots + P_{n0} \sin(n\omega_1 t + n\varphi) \\ & + P_{n1}^{\pm} \cos[(n\omega_1 \pm \omega_2)t + n\varphi], \end{aligned} \quad (6.4)$$

with the P_{ij} s being nonlinear functions of d_0 , d_1 , U_0 , and κ .

Further, as $d_1 \ll d_0$ (typical parameters: $d_0 = 5 \text{ \AA}$, $U_1/U_0 = 0.1$, $\kappa = 1.1225 \text{ (\AA}^{-1}\text{)}$ for Au surfaces), the higher order terms in d_1/d_0 can be neglected and the normalized current density at the difference frequency, as given by $P_{11}^{-(0)} = -\frac{1}{2} \cdot (d_1/d_0) \cdot U_1/U_0[1 + \zeta]$, can be written as:

$$I_t(\Delta\omega) = -\frac{1}{2} j_0 A_t \frac{d_1}{d_0} \frac{U_1}{U_0} (1 + 2\kappa d_0) \cos[(\omega_1 - \omega_2)t + \varphi], \quad (6.5)$$

with A_t being the effective tunneling area of the tip. In other words, by measuring the tunneling current at the difference frequency it is possible to obtain both an amplitude—which is proportional to the wave amplitude—and a phase—which reflects the local SAW phase.

For homodyne SAW-STM probing, i.e. in the absence of a reference signal ($U_1 = 0$), equation (6.3) yields, after expansion and recondensing:

$$\left. \frac{j}{j_0} \right|_{\text{SAW}}^{\text{dc}} = 1 + \sum_{n=1}^{\infty} \frac{1}{2} \frac{3}{4} \dots \frac{2n-1}{2n} \sum_{l=0}^{2n} \frac{\zeta^l}{l!} \left(\frac{d_1}{d_0} \right)^{2n-l} \quad (6.6)$$

as the normalized dc tunneling current density contribution, and

$$\begin{aligned} \left. \frac{j}{j_0} \right|_{\text{SAW}}^{\text{ac}}(\omega_1) = & -2 \cdot \sin(\omega_1 t + \varphi) \cdot \sum_{n=1}^{\infty} \frac{1}{2} \frac{3}{4} \\ & \dots \frac{2n-1}{2n} \sum_{l=0}^{2n-1} \frac{\zeta^l}{l!} \left(\frac{d_1}{d_0} \right)^{2n-1-l} \end{aligned}$$

as the normalized tunneling current contribution at the SAW frequency ω_1 .

As the tip–surface system represents a capacitor, the displacement current has to be taken into account too. The capacitor is periodically modulated by both the distance modulation and the additionally supplied reference voltage. The displacement current is obtained from $I_{\text{disp}} = (d/dt)(CU)$ with the capacitance C given by $C = C_0/(1+d_1/d_0 \sin(\omega t + \varphi))$ with $C_0 = \varepsilon A/d_0$; A is the effective area of the tip and ε is the permittivity of air. In the case of simple homodyne SAW-STM, i.e. without applying an additional reference voltage, the displacement current is given by:

$$I_{\text{disp}}(\omega_1) = -C_0 U_0 \omega_1 \frac{d_1}{d_0} \cos(\omega_1 t + \varphi), \quad (6.7)$$

and the displacement current at the difference frequency $\Delta\omega$:

$$I_{\text{disp}}(\Delta\omega) = \frac{1}{2} C_0 U_0 \Delta\omega \frac{U_1}{U_0} \frac{d_1}{d_0} \sin(\Delta\omega t + \varphi). \quad (6.8)$$

The displacement current—which is proportional to the involved frequencies—poses a serious problem for the direct SAW measurement by, e.g., a broadband high-frequency STM. Measuring at the difference frequency $\Delta\omega$, on the other hand, has the advantage of a displacement current $I_{\text{disp}}(\Delta\omega)$ being up to five orders of magnitude smaller than $I_{\text{disp}}(\omega_1)$ at the SAW frequency.

As an example, the following, quite typical SAW-STM parameters will be considered: $d_0 = 5 \text{ \AA}$, $U_0 \approx 0.1 \text{ V}$, $I_0 = 0.1\text{--}1 \text{ nA}$ and the SAW parameters $d_1 = 1 \text{ \AA}$ and $\omega_a/2\pi = 35 \text{ MHz}$. For pure SAW modulation and for using the tunneling parameters for Au surfaces ($\zeta = 11.225$), a dc tunneling current of $I_{\text{SAW}}^{\text{dc}} \approx 3.2 \cdot I_0$ and a tunneling current at the SAW frequency of $I_{\text{SAW}}^{\text{ac}}(\omega_1) \approx 4.8 \cdot I_0$ are obtained. The displacement current for this case is then $I_{\text{disp}}(\omega_1) \approx 0.1 \text{ nA}$ assuming an effective tunneling area of 1000 nm^2 . In the case of gap voltage modulation with typical parameters of $U_0 \approx 0.1 \text{ V}$ and a difference frequency of $\Delta\omega = \omega_1 - \omega_2 = 10 \text{ kHz}$ a tunneling current of $I(\Delta\omega) = P_{11}^- \cdot I_0 \approx 2.4 \cdot I_0$ is obtained, while the displacement current at $\Delta\omega$ is as small as $I_{\text{disp}}(\Delta\omega) \approx 1.1 \times 10^{-5} \text{ nA}$. Although the heterodyne technique circumvents the problems of STM bandwidth and the influence of the displacement current, the challenge of feeding a high-frequency voltage well isolated and without loss to the tip still remains.

Corrugated surface model. According to the flat surface model the measured SAW-STM phase directly yields the phase of the SAW. However, on corrugated surfaces—even if the corrugation is of atomic dimensions—the tunneling direction is dependent on the local topography since tunneling takes place on the shortest path between tip and surface. The spherical wave-assisted tunneling model that will be presented is still a one-dimensional model in terms of the tunneling process. In figure 24(a), the tunneling parameters are illustrated.

Here, it is suitable to express the tip–sample distance vector in spherical coordinates: $\vec{d} = (d_0, \Phi, \Theta)$, with the undisturbed tip–sample distance. The polar axis is chosen parallel to the z -direction, which is normal to the sample and lying in the x – y plane.

A SAW propagating along the surface is moving the atoms, and thus all surface objects, periodically leading to a particle displacement vector $\vec{d}' = [u_x \sin(\omega_1 t + \varphi_0), u_y \sin(\omega_1 t + \varphi_1), u_z \sin \omega_1 t]$. The u_i are the components of the SAW with φ_0 and φ_1 being the phase differences of u_x and u_y with respect to u_z . As all surface corrugation dimensions are in general much smaller than the SAW wavelength of at least $10 \mu\text{m}$, the part of the surface under investigation can be assumed to oscillate in phase. When scanning over larger distances, the SAW propagation phase has to be included too (see figure 26). Neglecting nonlinear SAW propagation effects (see SAW-AFM), the time-dependent tip-to-sample distance $d(t)$ in linear approximation, i.e. $u_i \ll d_0$ with $i = x, y, z$, is given as:

$$d(t) \approx d_0 \left[1 - \sum_i \frac{d'_i d_i}{d_0^2} \right]. \quad (6.9)$$

When applying the SAW-STM heterodyne mixing technique, an additional clock voltage at the frequency ω_2 is

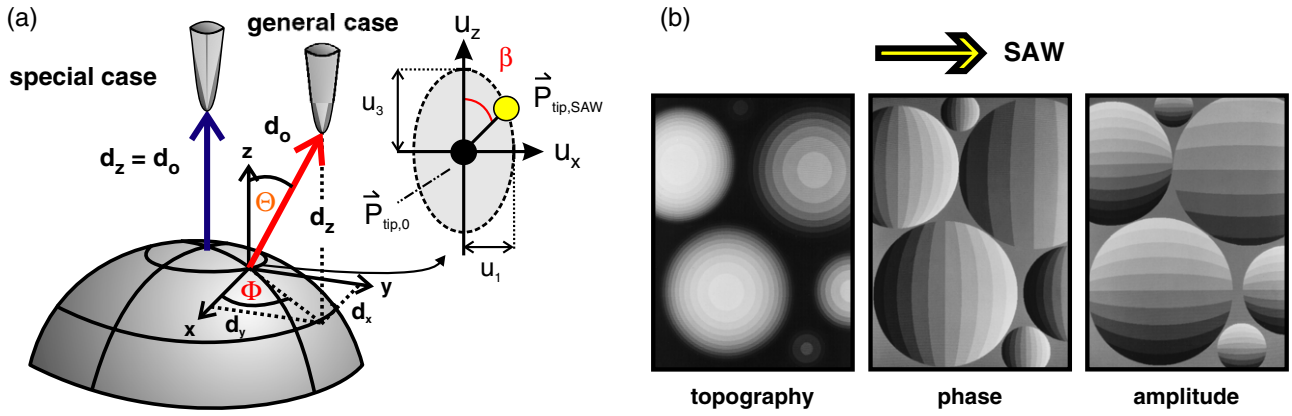


Figure 24. (a) Schematic drawing of the three-dimensional tunneling geometry. (b) Influence of topographic features of different radii and heights on the phase and the amplitude contrasts (simulations).

superimposed, leading to the effective gap voltage $U = U_0 + U_1 \sin \omega_2 t$. Now, the tunneling current density vector $\vec{j}(\Delta\omega)$ at the difference frequency can be written as:

$$\vec{j}(\Delta\omega) \sim \begin{pmatrix} u_x \cos \Phi \sin \Theta \sin(\Delta\omega t + \varphi_0) \\ u_y \sin \Phi \sin \Theta \sin(\Delta\omega t + \varphi_1) \\ u_z \cos \Theta \sin \Delta\omega t \end{pmatrix}. \quad (6.10)$$

Assuming the particle oscillation in the sagittal plane (x - y plane, with $u_y = 0$) and the phase difference between the particle displacement components u_x and u_z to be $\pi/2$, the amplitude A and the phase variation Ψ of the tunneling current at the difference frequency can be written as:

$$A = \sqrt{u_x^2 \cos^2 \Phi \sin^2 \Theta + u_z^2 \cos^2 \Theta} \quad (6.11)$$

$$\Psi = \arctan \left(\frac{u_x}{u_z} \cos \Phi \tan \Theta \right). \quad (6.12)$$

Numerical results of the amplitude A and the difference phase Ψ using equations (6.11) and (6.12) are plotted for six spherical structures embedded in a flat surface in figure 24(b) [124]. The SAW was propagating from the left to the right. The particle oscillation trajectory is assumed to be elliptically polarized in the x - z plane with $u_x/u_z = 0.6$ and $u_y = 0$. The highest phase contrast appears parallel to the SAW propagation direction where the topography shows steep transitions. The amplitude shows a smaller contrast parallel to the propagation direction, too, but a much larger one perpendicular to it. The amplitude contrast is also strongly influenced by steep topographic transitions. If the tunneling on top of the sphere is chosen to define zero phase, the positions at the borders of the sphere along the propagation direction give the extreme positive and negative phase values. These are then seen as phase jumps due to the 360° range limit of the lock-in amplifier.

Comparing the results for the six different spheres in detail, it is obvious that phase and amplitude contrasts are a strong function of local curvature, rather than absolute size. In the topography image, the smaller spheres are barely visible, however, due to their steep slopes they appear very bright on the phase and amplitude. On top of grains only the normal component of the oscillation trajectory is measured.

When scanning over troughs also the in-plane component of the oscillation is contributing. Hence, a phase shift results which depends on the inclination of the tangential plane at the tip position as well as on the orientation of the oscillation trajectory. The maximum effect appears at the bottom of the troughs, when the tip is scanning the neighboring grain, accompanied by a sudden change in the sign of the phase.

There are two ways to obtain the propagation phase on rough surfaces. First, measurement points can be chosen where the difference phase Ψ vanishes. This is, for example, the case for topographical maxima with only a tunneling component parallel to the polar axis ($\Theta = 0$). Second, from the measurement of the difference phase and the simultaneously measured topography this model allows for a phase subtraction of the topography-induced components delivering the pure propagation-induced phase.

In order to model the atomic phase and amplitude contrasts, the atom is treated as a small and spherical grain. Using equations (6.11) and (6.12), and assuming an atom being a Gaussian-shaped electron distribution, the phase and amplitude contrasts are obtained (cf figure (25)). The modeled SAW is propagating from the left to the right, as indicated in the figure. Below, the corresponding linescans of the topography, phase and amplitude are shown for a cut along the horizontal symmetry line. The phase image is characterized by a jump at the position of the atom with its maximum contrast along the direction of SAW propagation. The amplitude, on the other hand, now shows an almost point-symmetric image with a characteristic high contrast spot at the center position of the atom.

As the typical STM scan size (some 10 nm) is very small compared with the typical SAW wavelength (several micrometers), the local phase contrast of the in-phase oscillating atoms can be seen as the stroboscopic snapshot of a frozen state of oscillation within the SAW. For another measurement window, which lies at another position along the wave's propagation path, a different state of oscillation is seen. The SAW-induced phase, i.e. the linear phase behavior with respect to the distance from the wave source along the propagation direction, is introduced for the component of the tunneling current at the difference frequency in equation (6.5).

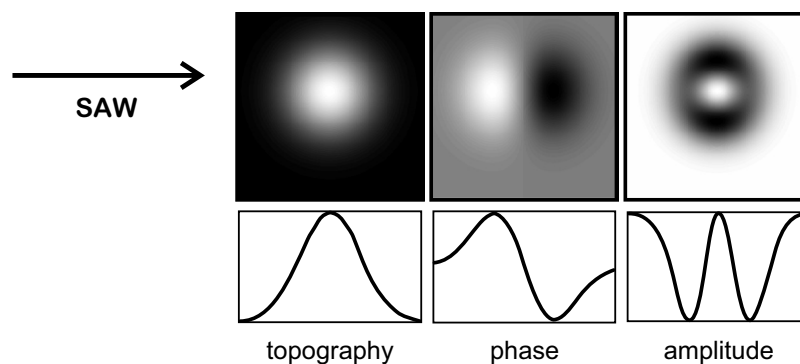


Figure 25. Modeled phase and amplitude contrasts for a single spherical atom (below: line scans along the symmetry axis).

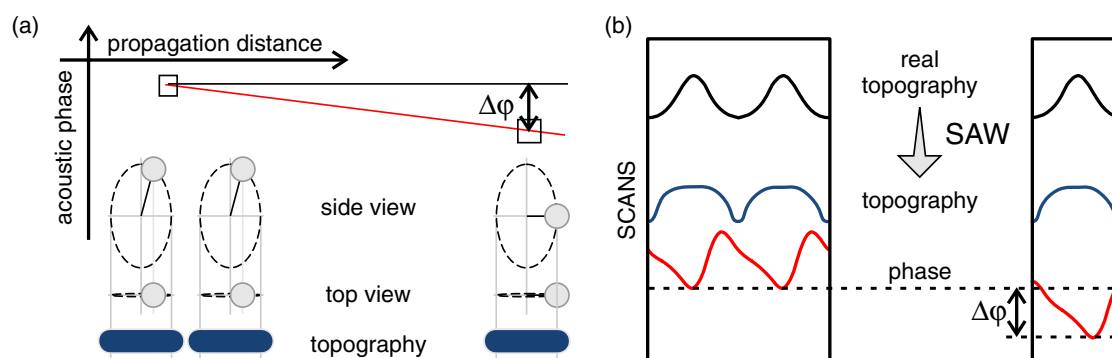


Figure 26. Illustration of the origin of the phase contrast. (a) Within a small scan area, the SAW-induced phase contribution is constant and the measured phase reflects the topography-induced part only. At some distance along the propagation of the SAW away, a different relative oscillation phase snapshot is imaged. (b) Topography, amplitude and phase scans for two locations where the SAW-related phase differs by $\Delta\varphi$.

In contrast to that, the topography-induced phase as introduced in equation (6.12) solely depends on the spherical tunneling coordinates. The absolute phase difference is given as the SAW-induced phase contrast $\Delta\varphi$. In the lhs panel of figure 26, side-view and top-view snapshots of the oscillation ellipse of a single atom (not to scale) are shown. The oscillation induced by the SAW is assumed to be stemming from a Rayleigh wave, i.e. the in-plane displacement component that is not in the sagittal plane is vanishing. Additionally, the SAW-induced topographic contrast is shown as a time-averaged projection of the oscillation ellipse on the sample plane. The first two ellipses belong to the propagation phase as indicated by the window in the leftmost plot, while the ellipse on the right belongs to a different propagation phase ($\Delta\varphi$). In the rhs panel, the corresponding line scans of the modeled real topography, the measured smeared-out topography and the phase along a mirror axis of the atom row are plotted. Looking at the phase contrast on the right, the whole contrast is shifted with respect to the position of the atom in the undisturbed lattice, as the frozen state of oscillation has changed. Additionally, the absolute phase value is shifted by $\Delta\varphi$ as the propagation phase has decreased.

6.2. Surface oscillations on the atomic scale

The measurement of atomic scale surface features in real space has been a great challenge in surface physics. A lot of effort has been devoted to reducing mechanical vibrations. Even SAWs,

as a special form of acoustic vibration, were known to reduce the STM contrast drastically [125]. Despite such averaging effects, the study of atom or molecule motions due to thermal or high-frequency excitations is of considerable interest. For instance, frequency spectra were recorded with an AC-STM in order to investigate adsorbed organic compounds [126], and the study of SAW-induced oscillations of self-assembled monolayers is important for SAW sensors [127]. Here, measurements of single, oscillating atoms are discussed [128].

The experiments were carried out on thermally evaporated and annealed 100 nm thick Au films on LiNbO_3 in ambient air at room temperature. The flat Au(111)-terraces exhibit large (111) facets which are a few 100 nm wide [129]. Rayleigh-type SAWs were excited on YZ- LiNbO_3 and at a frequency of 39.5 MHz ($\lambda = 88 \mu\text{m}$). The oscillation ellipse is polarized in the sagittal plane. Thus, the oscillation is described by the displacement components u_y and u_z . Within the $10 \times 10 \text{ nm}^2$ scan window, all the atoms oscillate with the same SAW propagation-induced phase. The excitation level at the signal generator output was +12 dBm. As the IDT is not electrically matched, the oscillation amplitude is $\approx 0.1 \text{ \AA}$.

In figure 27(a), a $2.8 \times 2.8 \text{ nm}^2$ topography image of the Au(111) surface is shown. With increasing SAW amplitude, the topography contrast is smeared-out due to the slow response of the electronic control unit compared with the SAW frequency (b). As the Rayleigh-type waves are polarized in the sagittal plane, this smearing-out is directed and can be seen as

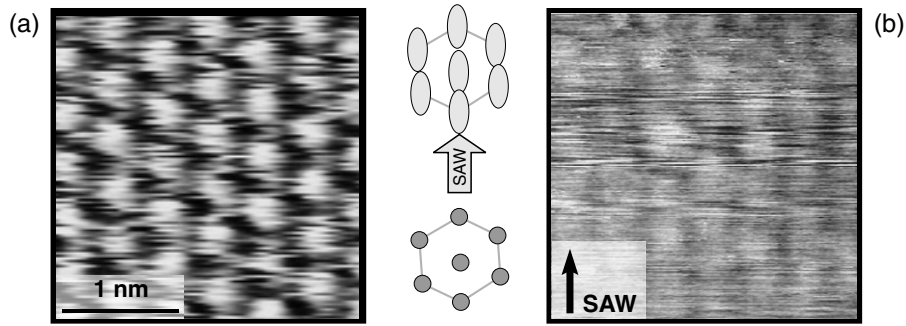


Figure 27. Undisturbed topography (a) of a Au(111) surface. An elliptically polarized particle displacement due to a propagating SAW (wave vector indicated by the arrow) leads to a directed smearing out of the atomic contrast (b).

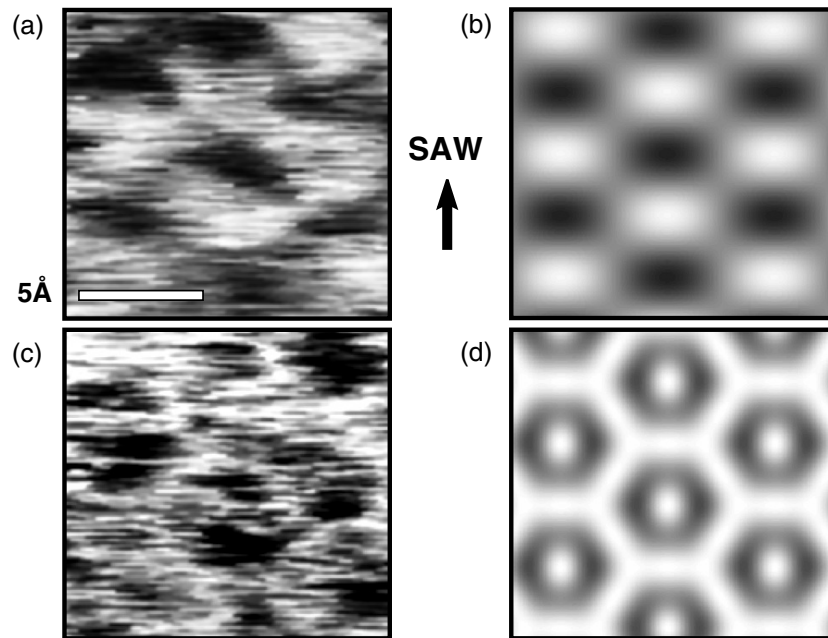


Figure 28. Comparison of the measured and slightly smoothed (a) and (c) with the modeled (b) and (d) phase and amplitude, respectively, revealing the hexagonal lattice structure. The wave's propagation direction is indicated by an arrow (b).

the time-averaged projection of the oscillation trajectory on the undisturbed sample plane.

For the heterodyne SAW-STM measurements, a 1 V rms clock signal at 39.51 MHz was applied to the tunneling gap and Δf was set to 10 kHz. The dc sample bias was 0.6 V and the tunneling current was kept constant at 11.4 nA. The scans were performed with 1000×1000 data points. No filtering procedures were applied. Figure 27(a) shows the undisturbed hexagonal lattice of the Au(111) surface with a lattice spacing of approximately 5 Å. Although the atomic resolution of the topographical image vanishes when the SAW is applied to the sample, the phase signal shows a periodic distribution of structures with high contrast (cf figure 28(a)) and the amplitude shows areas of different brightness (c) at the atom positions in the hexagonal lattice.

To model the contrast of the Au(111) lattice, the single atom model is expanded to the hexagonal lattice. The wave's propagation direction is indicated by the arrow in figure 28(b). For a sagittally polarized oscillation trajectory, and for a phase difference of the oscillation components u_y and u_z of $\pi/2$, the phase and the amplitude images are presented in (b) and (d),

respectively. The ratio of the axes of the oscillation ellipse is chosen as $u_z : u_y = 0.6 : 1$, which is in agreement with the calculated value for YZ-LiNbO₃ [108]. The phase and the amplitude depend on the topography (Θ , Φ), as well as on the wave properties u_y and u_z . While scanning over one atom, the phase shows a relative maximum at the point where the tunneling vector is collinear to the displacement vector—which is static for this stroboscopic measurement mode. The phase is leading before passing the atom, and retarded after passing the atom. This behavior is more pronounced along the SAW propagation direction than perpendicular to it. The modeled amplitude reproduces the hexagonal shape of the reciprocal elementary lattice cell projected around the single atom with a bright maximum on the top of the atom. Both measurement and simulation agree quite well, thereby confirming atomic phase resolution.

7. Investigation of elementary wave phenomena

The nanometer-scale lateral resolution of SAW-AFM, in combination with the extremely high vertical detection

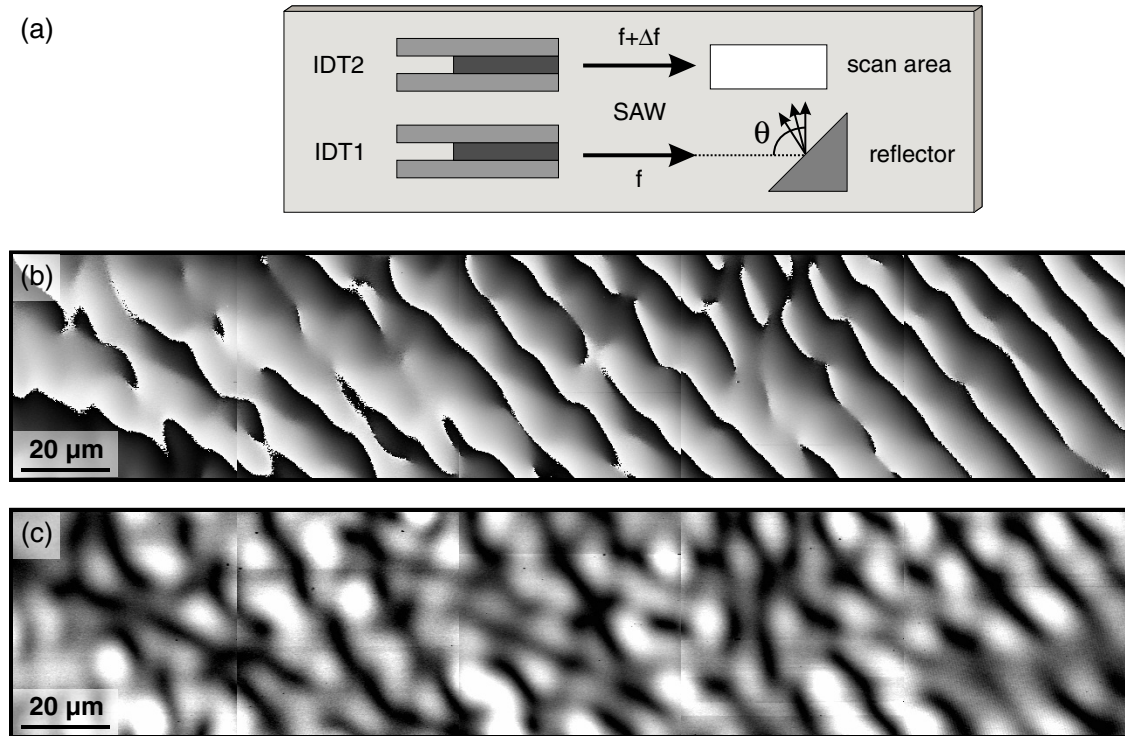


Figure 29. (a) Sample geometry for reflection and mode conversion studies. IDT 1 is illuminating a reflector that deflects waves into the propagation path of IDT 2. At the intersection of both wave contributions, the SAW-AFM mixing experiment is performed. Reflected wave field imaging: (b) SAW-AFM phase and (c) amplitude.

sensitivity, allowed for the first time the investigation of elementary SAW excitation and propagation phenomena. The first parts of this section deal with reflection and scattering phenomena, and the last part with the excitation of SAWs in the extreme limit of individual electrode pairs.

The investigation of elementary SAW phenomena, such as scattering from point-like objects or the excitation by single electrode pairs, was until the development of SAW-AFM an unsolved problem, despite the relevance of the accessible information for the design and optimization of SAW devices. Especially the sensitivity of SAW-AFM to all possible surface-guided modes makes the SAW-AFM an ideal tool for SAW studies. For example, SAW-AFM mixing experiments are possible even if the applied acoustic power differs by as much as 40 dB. This enables the study of minute acoustic features by sampling the wave of interest with a well-defined plane reference wave. This approach is common to all experiments presented in this section.

7.1. Reflection and mode conversion

To investigate wave reflection phenomena, the area into which the wave is reflected and scattered is illuminated by the reference wave field [130]. Figure 29(a) shows a schematic of the experimental setup. On a SAW substrate (here: ST-quartz), two parallel delay lines were fabricated. Only one IDT is active in each of the delay lines. Within the propagation path of one of the delay lines, the object of interest—in this case a reflecting wedge—is placed. The 60 nm thick Au wedge includes an angle of 45° with the incoming beam direction. The IDTs are oriented along the crystal's x -axis, such that

Rayleigh waves are excited at 219 MHz for $\lambda = 14.4 \mu\text{m}$. In order to allow for the propagation of Love waves in the perpendicular direction, the IDTs as well as the propagation path were covered with a 200 nm thick SiO_2 film, except for the area of the Au reflector pad.

Both IDTs were driven with a large power of +10 dBm. All wave components that are not relevant for the experiment were damped out by damping masses. This way, only the waves reflected from the object and the reference wave are present in the scan area. Figure 29(b) shows the phase and (c) the amplitude image of the reflected wave components. The images consist of five $50 \times 50 \mu\text{m}^2$ scans taken in the middle of the reference beam (width: $350 \mu\text{m}$). The position of the waves reflected exactly under an angle of 90° with respect to the center of the beam are located on the rhs of the image. In this area, the inclined phase fronts resemble the results of the crossed-beam mixing experiments. Toward the lhs, the phase images show an increasingly complex pattern as a result of non- 90° wave reflections. As the scattering angle θ becomes smaller than 90° , the distance between the phase fronts increases. Moreover, the distortions caused by the superposition of multiple waves become significant. The amplitude image (figure 29(c)) shows a strong, almost irregular spatial modulation. As mentioned previously, the appearance of an amplitude modulation is the result of the presence of more than two waves. The origin of this modulation becomes obvious by analyzing a smaller area of 'regular' phase fronts ($\theta = 90^\circ$) in more detail.

Figure 30 shows details for waves scattered under $\theta = 90^\circ$. It is apparent that the phase (a) and amplitude (b) patterns

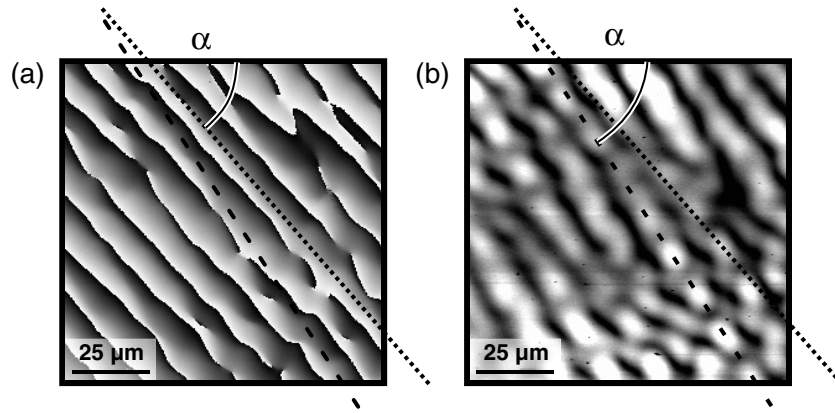


Figure 30. Reflected waves in areas of 'regular' phase fronts ($\theta = 90^\circ$). The phase fronts (a) are primarily parallel to the dotted line, and the amplitude maxima (b) are parallel to the dashed line.

include a different angle with respect to the incoming k -vector. The phase fronts are parallel to the dotted line ($\alpha = 49^\circ$), while the amplitude maxima are predominantly parallel to the dashed line ($\beta = 57^\circ$). The angles refer to the x -axis direction. Obviously, the modulation of the amplitude signal, which is the result of a perturbation in the mixing experiment, has to be caused by a different wave mode from the primary mixing signal which is visible in the phase image.

At this point it is necessary to analyze the existing wave types. In the 0° -direction, a Rayleigh wave exists which is excited by the transducers at a wavelength of $14.4 \mu\text{m}$. In the 90° -direction, two relevant wave modes exist. One is an electrically non-coupling Rayleigh wave ($v = 3510 \text{ m s}^{-1}$) and the other a Love wave ($v = 4980 \text{ m s}^{-1}$). Since the frequency for all modes is the same, the resulting wavelengths of the additional modes at 219 MHz are $16.0 \mu\text{m}$ and $27.7 \mu\text{m}$, respectively. Mixing these wave modes with the reference Rayleigh wave ($\lambda = 14.4 \mu\text{m}$) in a 90° geometry leads to an inclination angle of the phase fronts of $\alpha = 48^\circ$ and $\beta = 58^\circ$, respectively. These values are in very good agreement with the angles extracted from the phase and amplitude images. Thus, it can be concluded that the reflection of the primary Rayleigh wave beam at the Au wedge indeed leads to a mode conversion, such that the outgoing acoustic energy is distributed into two acoustic modes. As the measurements were performed in vertical detection mode, the mixing experiment is dominated by Rayleigh waves. The phase slope is therefore determined by the wavelength of the non-coupling Rayleigh mode of $\lambda = 16 \mu\text{m}$. The mixing of the Love wave and reference wave is obviously much weaker and leads to a distortion of the phase signal only. The amplitude image, on the other hand, is dominated by this additional contribution to the mixing signal.

7.2. Scattering

The spatially resolved investigation of wave scattering is of great fundamental as well as technological interest [131]. Efficient scattering occurs when the size of the elastic inhomogeneities is on the order of the wavelength. An inherent problem for the design of SAW devices is that the IDT electrodes are perfect scatterers, as are the terminations of the

electrodes. Other scattering sources are the inhomogeneities in the metallization and other layers. Conventional analysis tools usually fail to detect scattering phenomena.

The influence of an elastic inhomogeneity, in this case a jagged defect in a 40 nm thick Au layer, on the propagation of a Love wave is shown in figure 31(a). The Love waves were excited at 340 MHz ($\lambda = 14.4 \mu\text{m}$). The phase deviation image ((b), linear phase subtracted and phase jumps removed) shows the scattered wave pattern. The position of the metal pad edge is indicated by a dashed white line. The waves were coming from the left and the right and their k -vectors were perpendicular to the phase fronts that are still visible as artifacts in (b), i.e. rotated with respect to the scan window. The scattered waves are visible as a distortion to the primary mixing signal. The jagged structure obviously acts as a scattering center and diverts the acoustic energy in different directions. Due to the anisotropy of the substrate, the scattered waves are not spherical, but propagating along the preferred 45° directions with respect to the incoming wave vectors. The complicated geometry of the object renders a detailed investigation of the fundamental process difficult.

Less complex model systems, i.e. metallic structures with a simple geometric shape, were fabricated by electron beam lithography. To allow for the wave excitation in the non-collinear geometry, GaAs was chosen as a substrate. The non-collinear geometry has the important advantage that forward and backward scattered components can be easily distinguished.

Figure 32 illustrates the effect of scattering off a circular Au dot (diameter: $5 \mu\text{m}$, thickness: 45 nm). Rayleigh waves were launched from the right and from the top (as illustrated in the sketch on the rhs) at a frequency of 860 MHz ($\lambda = 3.3 \mu\text{m}$). For the measurement, IDT 1 was powered with +5 dBm and IDT 2 with -5 dBm. Therefore, the amplitude signal (b) is dominated by the higher amplitude wave coming from the top. In the wave shadow of the dot, a bright area of high amplitude is visible, which is adjacent to dark areas of low amplitude which surround the entire dot. A smaller wave maximum is apparent in front of the scatterer (toward IDT 1) which resembles a bow wave. More, weaker wave fronts follow in the vicinity of the scatterer. An analogous wave pattern is found for a pole

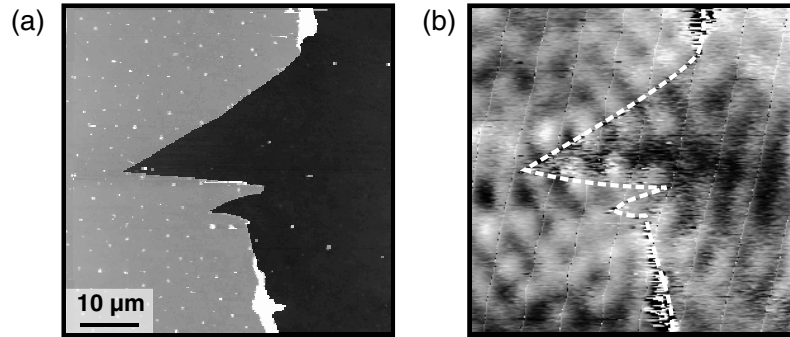


Figure 31. Distortion of the wave field by scattering off of a topographic inhomogeneity. The topography (a) shows the jagged gold pad edge on the lhs The phase deviation image (b) reveals the scattering of the waves incident from the left and the right by the spike.

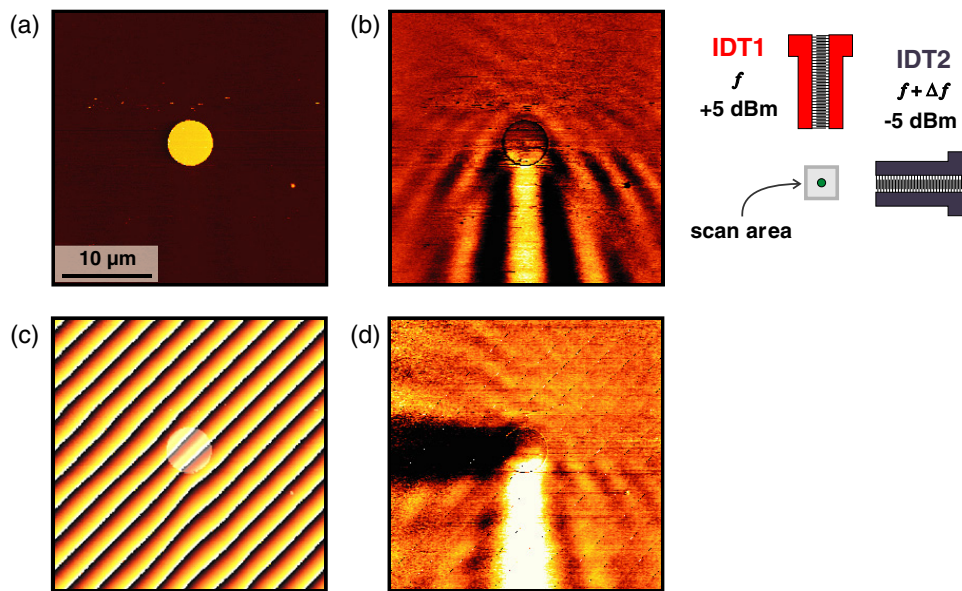


Figure 32. Scattering off a circular dot in the non-collinear geometry (rhs): (a) topography, (b) SAW-AFM amplitude, (c) SAW-AFM phase and (d) phase deviation image. The wave fields are launched from above (higher amplitude) and from the right (lower amplitude).

in streaming water. Here, however, we are not looking at a snapshot of the movement, but the image of the envelope of the RF surface oscillations.

The phase image (c) shows the rotated phase fronts that are characteristic for the nonlinear geometry. At the position of the scatterer (indicated by a bright disk), the phase fronts are slightly distorted. The origin of these primary distortions are the different phase velocities on Au and GaAs (2700 m s^{-1} versus 2870 m s^{-1}). The phase deviation image in (d) shows this behavior even clearer. In the phase image, the power dependence of the scattering effect is less pronounced and a scattering-induced contrast is also visible in the horizontal direction. In both perpendicular directions the waves scattering in the respective forward direction suffer from a phase lag. In the mixing process this leads to a bright contrast in one direction and to a dark contrast in the other direction. The substrate anisotropy results in non-trivial wave fronts in the amplitude and phase images.

There has been growing interest in the study of two-dimensional, periodic, elastic structures known as phononic crystals [132]. Phononic crystals offer the possibility to create

acoustic phonon bandgaps manipulating the electron–phonon interaction. Moreover, phononic crystals are of interest as functional elements of SAW devices. Measurements and calculations of SAW localization have been reported in one-dimensional Fibonacci superlattices [133], as well as in two-dimensional periodic elastic structures [59, 134].

SAW localization was studied in the non-collinear geometry on GaAs(001). A regular lattice of Au dots (diameter: $1 \mu\text{m}$, thickness: 45 nm) has been placed in the center of a crossed delay line structure. The face-centered cubic (fcc) lattice spacing was $\Delta x = 4 \mu\text{m}$ and its width $100 \mu\text{m}$. The Rayleigh waves were excited at a frequency of 694 MHz ($\lambda = 4.0 \mu\text{m}$, acoustic aperture: $65 \mu\text{m}$). Figure 33(a) shows a $20 \times 20 \mu\text{m}^2$ scan close to the edge of the regular dot lattice. Two collinear IDTs of the device (right and left of the array) were powered at $+5 \text{ dBm}$. The phase image (b) shows a predominantly linear phase behavior with the phase fronts being strongly deformed at the positions of the dots. Around the dots a phase lag becomes obvious indicating scattered components. In the corresponding amplitude image (c) regular, localized spots of high wave amplitude at the dot

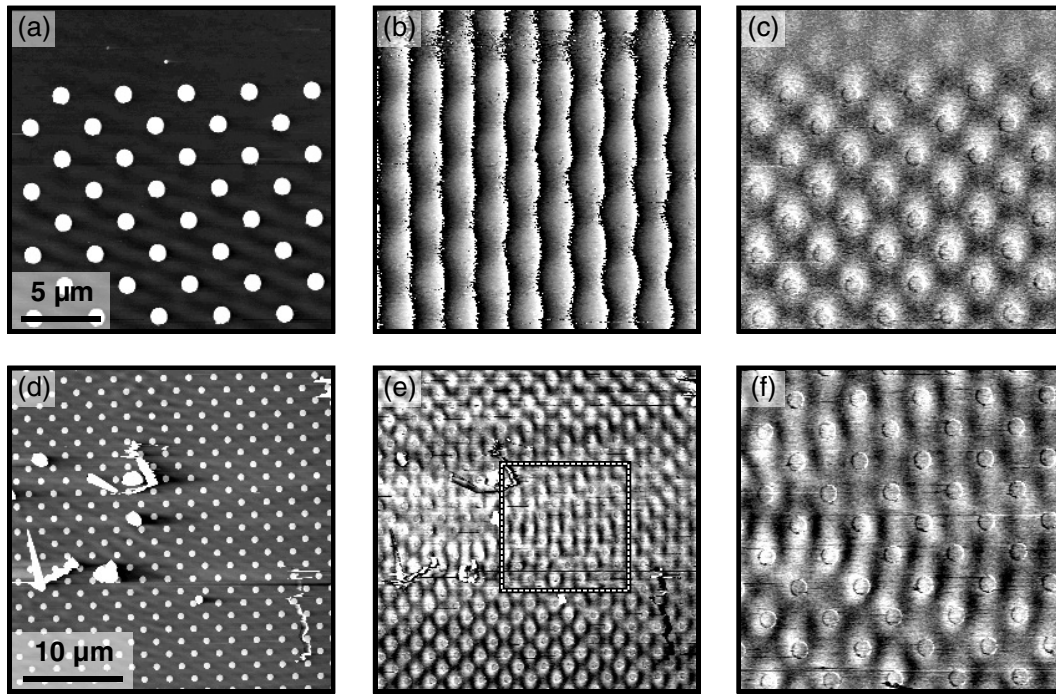


Figure 33. Scattering in a two-dimensional acoustic reflector lattice. Above: topography (a), amplitude (b) and phase (c) of a regular lattice. Below: results for a distorted lattice. The topography (d) shows surface adsorbates that lead to additional scattering components in the amplitude image (e) and its close-up (f).

positions are found. Outside the dot lattice (at the upper edge of the image), the signal quickly decays.

Figure 33(d) displays a $50 \times 50 \mu\text{m}^2$ topography scan of a locally damped dot lattice. The distortions were weakly coupling surface contaminations that mainly lead to a local wave amplitude damping. The corresponding amplitude image (e) shows the same apparent amplitude localization as in (c) above and below the locally damped region. The amplitude appears to be concentrated in certain angular regions around the defects. The $20 \mu\text{m}$ zoom (f) of the amplitude (the inset in (e) indicates the relative position) confirms the wave reflection preferably under an angle of 25° with respect to the horizontal propagation direction. For the correct interpretation of the results, full three-dimensional simulations are needed [135, 136].

7.3. Emission from elementary wave sources

The most important aspect for SAW applications is the effective wave excitation and detection on piezoelectric substrates. The optimization of this process, especially at very high frequencies and submicrometer wavelengths, requires both improved characterization and simulation tools. At the core of each transducer is a rather inefficient electrode pair which is repeated in a regular fashion to form an efficient acoustic device. The knowledge of the acoustic characteristics of an individual electrode pair would enable new, more physical simulation schemes for SAW devices. The study of wave excitation from an individual source is extremely challenging as the involved amplitudes are orders of magnitude below 1 nm. The experimental results [137–140] demonstrate

the very high vertical resolution of the SAW-AFM which is smaller than 0.01 pm .

The simplest acoustic source is a single electrode pair. Figure 34(b) shows the topography of the single-finger transducer on GaAs. The 50 nm thick Al electrodes have been fabricated by electron beam lithography with a gap width of $1.4 \mu\text{m}$. The device under test (DUT) was placed in the propagation path of a regular IDT delivering a reference wave field at 397 MHz ($\lambda = 7.2 \mu\text{m}$), as sketched in (a).

A SAW-AFM mixing signal is detected in the vicinity of the DUT when both sources are powered with $> +10 \text{ dBm}$. In order to increase the sensitivity of the SAW-AFM, especially soft cantilevers with a spring constant of 0.01 N m^{-1} were used (Microlever, Veeco). Figures 34(c) and (d) show the phase signal and the corresponding amplitude, respectively. The phase image exhibits above and below the single electrode pair behavior that is already known from non-collinear mixing experiments. The 45° -inclined phase fronts are indicative of two perpendicularly propagating waves, i.e. the single electrode pair is emitting waves perpendicular to the finger axis. This finding is confirmed by the amplitude measurement (d). Over the length of the electrodes, areas of high amplitude (bright) are found, whereas the amplitude quickly decays at the end of the single-finger structure. The modulation of the amplitude parallel to the phase fronts is a result of electric, inter-transducer cross-talk. It has to be noted that the single-finger structure is a quasi-ideal broadband emitter whose transmission characteristic cannot be determined by conventional electric measurements (vector network analyzer).

A dramatic increase in the emitted amplitude is achieved when the *hot* electrode is surrounded on both sides by electrodes that are connected to RF ground. Figure 35(a)

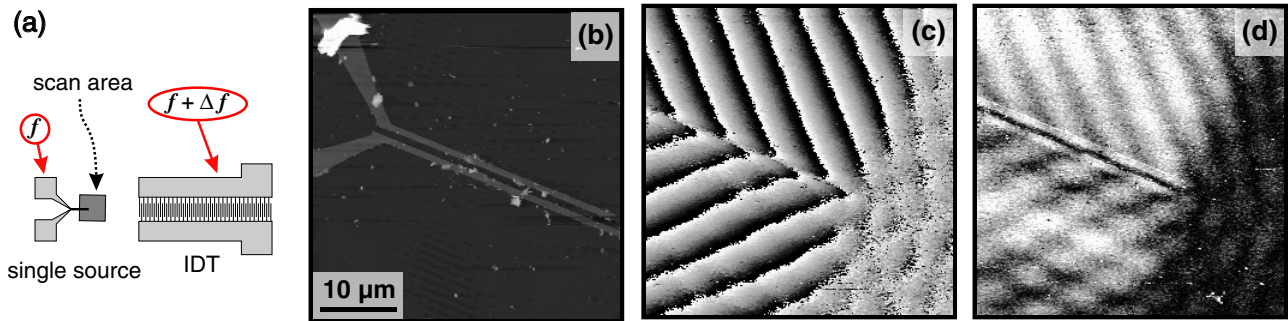


Figure 34. Radiation characteristic of an individual single-finger source. (a) Scheme of the probing geometry showing the device under test and the IDT for the excitation of the reference wave field. (b) Topography, (c) SAW-AFM phase image and (d) SAW-AFM amplitude image. The wave emission occurs predominantly in directions perpendicular to the electrodes.

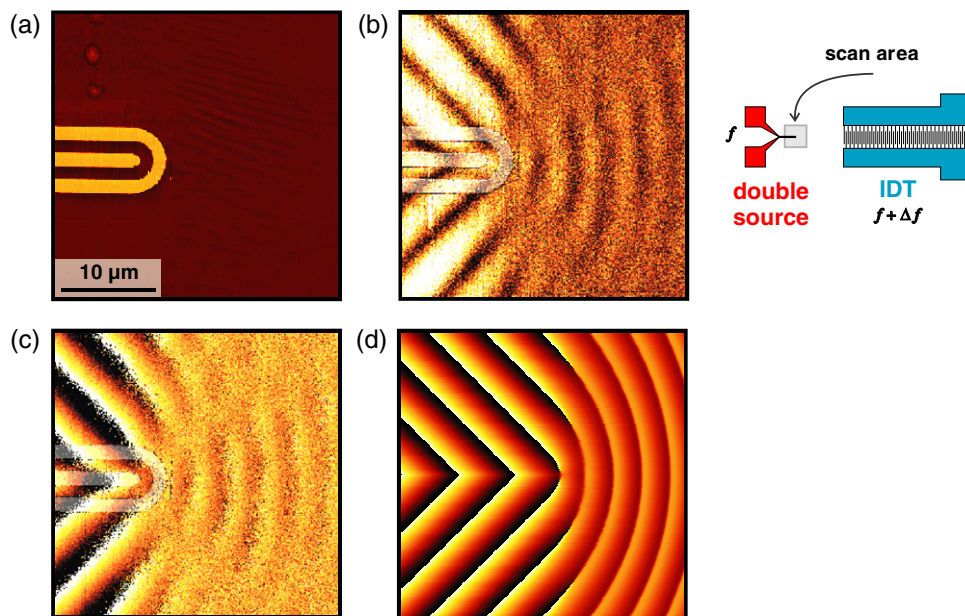


Figure 35. Emission characteristic of a single double-finger source (geometry on the rhs). (a) Topography, (b) SAW-AFM amplitude image, (c) phase image and (d) simulation of the phase signal.

shows the topography image of the otherwise identical double-finger device structure. The schematic on the rhs illustrates the DUT position within the reference wave path. The term double-finger source refers to the number of areas with high electric field strength along the excitation direction. As can be seen in the amplitude (b) and phase (c) images, the wave emission is very similar to the emission from a single source, however, with a highly increased excitation efficiency and considerably reduced noise level. At the end of the transducer, a small amount of acoustic energy is also radiated in the direction of the reference IDT. In this direction, the signal period is $\lambda/2 = 3.5 \mu\text{m}$ (simulating a finger-end effect). Furthermore, the phase fronts are bent as the emission from the end of the transducer resembles the emission from a point source. Under 45° , no waves are emitted as no electromechanically coupling Rayleigh wave exists in this direction [141]. For simulating the phase contrast (d), the wave emission was assumed to occur from a line source coupled to a circular source in the rhs half-space. The efficiency of the circular source was chosen to be much smaller than that of the line source. The distortion due to the electric cross-talk, which

is clearly visible in the amplitude image, was taken into account in the simulation. The measured phase image (c) shows reasonable agreement with the simulated phase contrast (d).

Finally, a point-like source [142] was fabricated and investigated [140]. The advantage of such a source is that the anisotropy of the electromechanical coupling and the k -vectors can be measured conveniently on any given piezoelectric surface in a single measurement. The point-like acoustic source shown in figure 36(a) was fabricated by electron beam lithography on GaAs(001) and placed within a 890 MHz delay line structure ($\lambda = 3.2 \mu\text{m}$). The hot circular electrode (diameter: $4 \mu\text{m}$) is surrounded by an open ring electrode (gap distance: $1 \mu\text{m}$) which was connected to RF ground. The SAW-AFM measurement, especially that of the amplitude (b), shows that the wave excitation is preferably occurring in directions parallel and perpendicular to the reference beam—giving rise to a clover-shaped pattern. This behavior is in accordance with the simulated angular dependence of the coupling factor shown in figure 37. In the preferred directions, the pseudo-SAW converts into a true Rayleigh wave (TSAW) and exhibits its coupling maximum. At an angle of 23° , the TSAW has

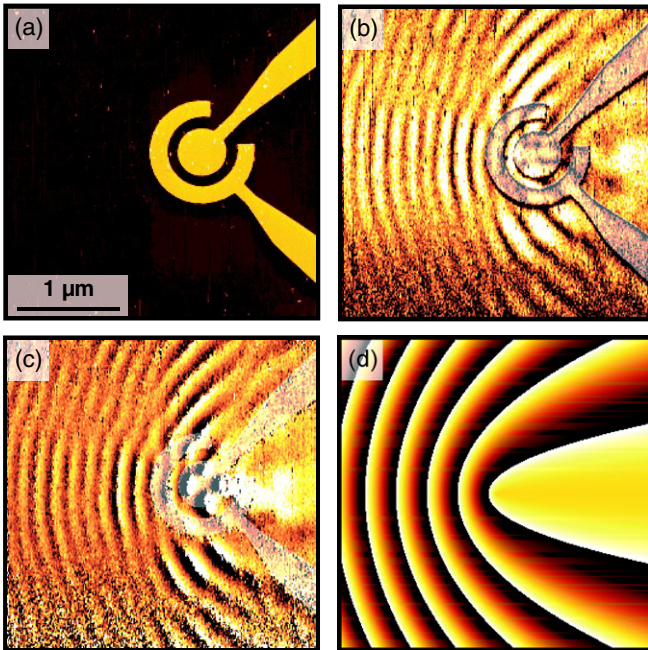


Figure 36. Emission pattern of a single point-like source on GaAs(001). (a) Topography, (b) SAW-AFM amplitude and (c) phase. The simulated phase contrast is shown in (d).

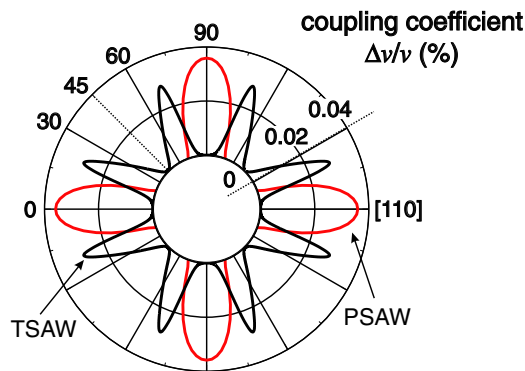


Figure 37. Polar plot of the electromechanical coupling coefficient $K = \Delta v/v$ for the true SAW (TSAW) and the pseudo-SAW (PSAW).

its coupling maximum and shows vanishing beam steering. Around 45° , no electrically coupling mode exists as can be seen in the amplitude and phase images. In between the high-coupling directions, the modes are in parts strongly damped and show significant beam-steering effects.

The phase signal (figure 36(c)) shows in areas above and below the circular source a behavior similar to that of the two single-finger sources, i.e. a characteristic dip at 45° . On the lhs of the source, i.e. where the emission direction is opposite to the propagation direction of the reference wave field, characteristic $\lambda/2 = 1.6 \mu\text{m}$ phase jumps are observed as expected from a SAW-AFM mixing experiment in the collinear geometry. On the other side of the DUT, the k -vectors of reference source and circular source are parallel. As the lateral variation of the phase signal is a function of the *difference* of the involved k -vectors—which is vanishing in this case—the phase remains constant along this direction. These characteristics of the

phase image are reproduced qualitatively by the simulations shown in figure 36(d). Note that the influence of the substrate anisotropy requires corrections of this model involving more complex details.

8. Ultrasound and friction on the nanoscale

So far, the focus was on vertically acting tip-sample forces, except for the detection of in-plane polarized waves with SAW-LFM. In general, however, there are also lateral forces acting on the tip, which impede the movement of the tip on the surface and lead to a torsion of the cantilever. The torsion of the cantilever is maximized when the scan direction is perpendicular to the cantilever axis. The torsion signal changes sign when the scan direction is reversed (e.g. at the end of the scan window), leading to a scan hysteresis with a positive torsion signal in one scan direction and a negative signal in the opposite scan direction. The LFM signal reflects the torsion of the cantilever due to friction or steep topographical features and it is dependent on the interacting materials, the scan speed, the force set-point and the tip geometry, as well as the temperature and the humidity. Lateral force microscopy is a well-established technique for the investigation of friction phenomena on the micro- and nanoscale [143].

Friction is the force between two bodies in contact that opposes their motion. For many industrial applications, the main tribological concern is to reduce the friction coefficient, and by that dissipated energy. The common way of controlling friction is the use of lubricants. However, also ultrasound was found to be a helpful tool to overcome friction in a controlled way [144, 145]. The influence of acoustic bulk waves on the microscopic tip-sample contact has been investigated [19, 146] and acoustically induced superlubricity has been reported. Compared with acoustic bulk wave studies [147–149], SAWs offer the advantage of an extremely well-defined, pure acoustic mode spectrum. The combination of SAW-AFM and LFM has therefore the advantage of being able to precisely determine the origin of ultrasound-induced superlubricity in nanoscopic contacts [150].

8.1. Acoustically-induced superlubricity

SAWs were found to have a strong influence on the LFM signal [151]. To study the related effects in detail, a SAW device structure with a narrow aperture was used, conveniently allowing for cross-beam scans. The device consists of 1000-electrode-IDTs and was fabricated on GaAs for excitation at $f = 538 \text{ MHz}$ ($\lambda = 5.2 \mu\text{m}$). Figure 38(a) shows the topography (lower lhs corner) and the simultaneously recorded SAW amplitude information (upper rhs corner). In the $60 \mu\text{m}$ scan, the SAW beam emitted from the transducer is visible as a bright area (high amplitude). In (b), a close-up of the LFM signal is presented ($40 \mu\text{m}$ scan, position indicated by white square). The forward (bottom left) and backward (top right) scans clearly show that the cantilever torsion—and thus friction—is reduced in the areas of the SAW beam. This reduction leads to a brighter area in the forward scan direction and to an equivalently darker area in the backward

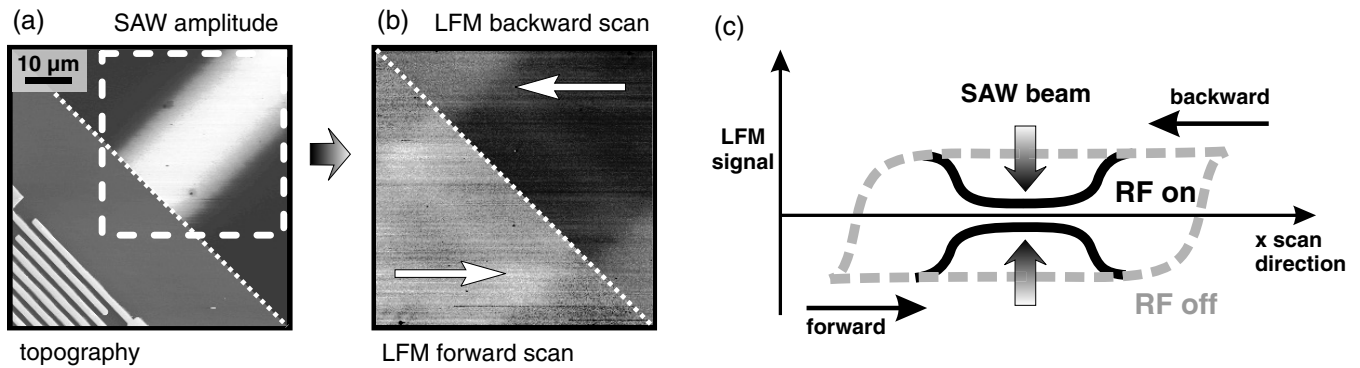


Figure 38. Acoustic friction reduction: (a) topography (lower triangle) and corresponding SAW-AFM amplitude (upper triangle), showing the acoustic beam launched from the transducer (bright area). (b) LFM close-up (forward scan: lower triangle; backward scan: upper triangle) across the propagating SAW beam. (c) Illustrates the observed lubrication effect: the scan direction-dependent hysteresis is significantly reduced at the position of the SAW beam.

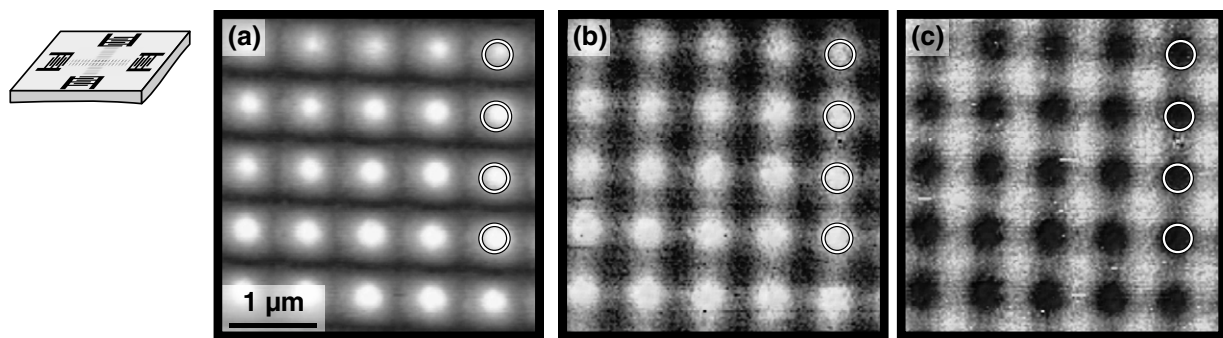


Figure 39. Demonstration of ultrasonic lubrication in a crossed, standing wave field: (a) SAW-AFM amplitude, (b) LFM forward and (c) backward scan.

scan direction. In contrast to the SAW-AFM amplitude image, the RF signal was not modulated and had the same nominal power of +5 dBm. Therefore, the effect on the LFM signal is solely due to the RF surface oscillations and not due to low-frequency cantilever vibrations.

This friction reduction effect on the LFM signal is further illustrated in figure 38(c): in the absence of the SAW, a strong hysteretic effect is found for the whole (inner) scan range without any local variation (dashed lines). At the turning points, the direction of the cantilever movement reverses and the friction force changes sign (and goes through zero). In the case of an applied wave field, however, friction is locally reduced and approaches zero friction force values. In a complementary manner, this effect leads in the forward direction to a local increase in the LFM signal, whereas in the backward direction it leads to a decrease in the LFM signal.

By exciting crossed, standing wave fields on GaAs(001), the friction reduction effect can be made visible in two dimensions. In figure 39(a), the measurement of the standing wave field pattern by standard mode SAW-AFM is shown. It exhibits an egg-carton-shaped pattern (raw data) with a periodicity of $\lambda_{\text{SAW}}/2$. As two RF generators were used to power three of the IDTs, while the 4th was used as a reflector, the modulation along the x -axis direction is slightly less pronounced. In figures 39(b) and (c), the LFM scans in the forward (left to right) and the backward (right to left)

scan direction are shown. In the forward scan direction, the LFM image basically reproduces the egg carton pattern, i.e. the areas of high wave amplitude show up as areas of increased LFM signal, whereas in the backward scan direction the image appears inverted. Again, the reason is the existence of a pronounced effect of locally reduced friction. This leads to a smaller LFM hysteresis, appearing as an increase in the forward (bright spots) and a decrease (dark spots) in the backward scan direction at the positions of maximum oscillation amplitude (see also the sketch in figure 38(c)).

The interesting question is whether a complete suppression of friction at higher applied power is possible. As the narrow aperture IDTs show very poor impedance matching, the following higher power measurements were performed using conventional split-finger SAW devices. A Rayleigh wave delay line on ST-quartz operating at 562 MHz was employed, where one IDT was powered with +2 dBm while the opposing one was driven with variable power. This way, a partial standing wave field was established between the IDTs.

Figure 40 shows a pseudo-three dimensional representation of 10 μm LFM linescans. Along the slow scan axis, the power of the second IDT was increased from -8 to +16 dBm. At low power, a strong modulation of the LFM signal is found which has the same periodicity as the standing wave field ($\lambda/2 = 2.6 \mu\text{m}$). As in the case of the acoustic beam measurement (figure 38), the oscillation amplitude in the standing

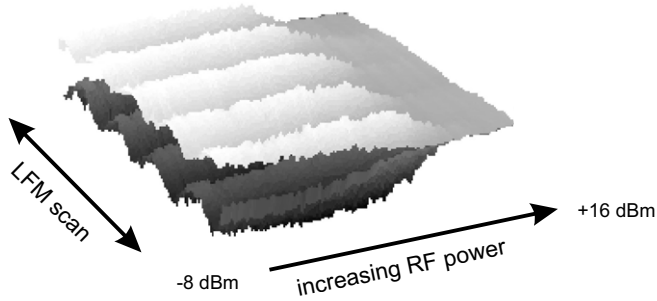


Figure 40. Acoustic power dependence of the friction reduction effect in a weakly modulated standing wave field. LFM linescans: backward scan (upper surface) and forward scan (lower surface). The power was increased from -8 dBm to 16 dBm.

wave field varies with position and thus leads to a position dependence of the friction reduction effect. This effect is complementary for the forward and backward scan directions. With increasing power, the modulation depth of the LFM signal increases until a maximum modulation is reached for $+4$ dBm. Above $+8$ dBm, the signals for the forward and backward scans become identical around the positions of the friction minima. Moreover, the modulation depth decreases and the areas of identical forward and backward LFM signal get wider. Above $+12$ dBm, the modulation as well as the difference between the forward and backward signal have vanished. The LFM hysteresis is now fully suppressed and both LFM signals are identical and zero.

By combining SAW-LFM and SAW-AFM, the origin of the friction reduction effect and its influence on the coupling between tip and sample can be studied in great detail. For this purpose, a standing Rayleigh wave field was excited at 198 MHz on GaAs. With a nominal power of $+5$ dBm applied to both transducers, the standing wave field shows a degree of modulation of close to 100% (see diagram in figure 41(b)). An area measuring $20 \times 20 \mu\text{m}^2$ was scanned in subsequent SAW-LFM and SAW-AFM scans. The power has been chosen such that friction is vanishing around the wave field maxima only, and the LFM hysteresis is fully developed elsewhere (cf figure 41(a)). Since the SAW-AFM is more sensitive toward vertical oscillation components than in-plane oscillation components (about one order of magnitude) [152], it can be concluded that the maxima in (b) indeed coincide with the maxima of the vertical oscillation component.

From comparison, it is obvious that the areas of vanishing friction coincide with the areas of maximum vertical surface oscillation. This observation points toward the conclusion that the mechanical diode effect is responsible for the friction reduction effect. In this scenario, the rectification of the vertical, high-frequency oscillations of the surface lead to an effective counteracting force, which acts vertically on the surface and leads to a shift of the cantilever away from the surface. The reduction in the force the tip exerts on the surface, and the reduction in the interaction area, results in an effective reduction in the acting lateral forces.

The SAW amplitude signal detected by LFM (cf figure 41(c)) shows behavior that is significantly different from

the vertically detected amplitude signal. Intuitively, it could be assumed that the SAW-LFM signal is not coupling to the vertical movement of the surface, but to the in-plane movement of the surface which is phase-shifted by 90° in the case of a Rayleigh wave. However, the finding that the positions of the amplitude maxima of the standing wave field at small power are identical to the positions of the vertical oscillation maxima speaks against this assumption. Figure 41(c) shows maxima which are shifted with respect to these positions. It has to be noted that the differences between the forward and backward scans can be attributed to the tip asymmetry.

An elegant explanation for this experimental finding is again given by the friction reduction effect. In the case of small applied power levels, the friction forces lead to a static torsion of the cantilever during scanning, i.e. the tip is not in its rest position. Therefore, additional, vertically acting tip forces lead to torque on the cantilever and a vertical oscillation of the tip can therefore be seen in both the vertically (deflection signal) and torsionally (LFM signal) detected cantilever oscillation. For high SAW power, friction vanishes at the positions of the maxima of the standing wave field, leading to the loss of static torsion of the cantilever. Now, the vertical oscillation does not lead to torque on the cantilever and the LFM-detected amplitude signal breaks down. Instead of maxima, minima can be found in figure 41(c). In order to aid the interpretation, the corresponding graphs of the forward and backward scans also show the vertically detected amplitude signal (in grey). Above the threshold power for the complete friction reduction, the torsional amplitude of the cantilever is drastically reduced and has its minimum for maximum vertical oscillation amplitude. The friction forces between tip and surface are therefore critical for contrast formation in SAW-LFM.

The reason for the SAW-AFM and SAW-LFM both responding primarily to the vertical oscillation maxima is that the nonlinear lateral coupling strength was found to be at least one order of magnitude weaker than the vertical coupling strength. Therefore, the tip experiences only the vertical vibration of the surface and it is hardly sensitive to the 90° shifted maxima of the longitudinal component of the standing wave field (in the case of Rayleigh waves). Thus, another *effective* lateral coupling mechanism must exist.

Finally, it has to be noted that the friction reduction effect was observed for a variety of substrates and thin films (quartz, GaAs, AlN, LiTaO₃, SiO₂, Al, Au, Ni) in the frequency range from 200 MHz to 3 GHz. For carefully carried out measurements on in-plane polarized SAW modes, no measurable friction reduction effect was found—even at the highest applied acoustic powers. It has to be noted, however, that if the surface has a non-vanishing roughness (at best on the atomic scale), transversal oscillations *always* lead to vertical forces in a microscopic contact. It can be concluded that the friction reduction effect can be unambiguously linked to the mechanical rectification of the vertical oscillation component [152].

A possible explanation of the breakdown of the lateral coupling mechanism is sketched in figure 42. In the presence of friction (friction force $F_f \neq 0$), i.e. for small vertical

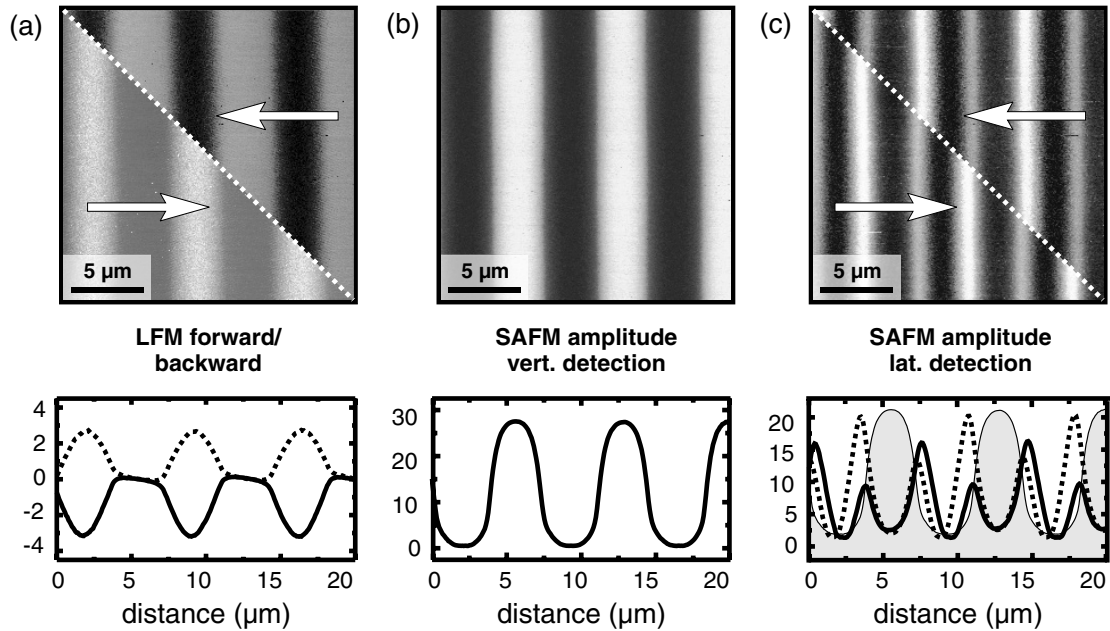


Figure 41. Investigation of the nonlinear coupling mechanism: (a) shows the forward and backward scans of the LFM signal, (b) the corresponding vertical SAW-AFM amplitude image of the standing Rayleigh wave field and (c) the SAW-LFM image. Representative line scans are shown below. At the positions of antinodes in the standing wave field (bright areas in (b)), friction is locally reduced (flat areas in (a)). In between those areas, the LFM image exhibits typical hysteresis behavior. At the positions of the wave field maxima, the SAW-LFM image (c) shows minima that are accompanied by two side maxima.

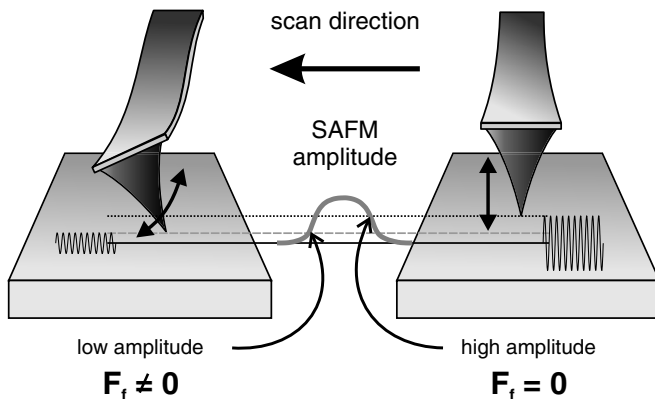


Figure 42. Explanation of the breakdown of the lateral nonlinear coupling mechanism. At low wave amplitudes (lhs), frictional forces act on the scanning cantilever resulting in a quasi-static torsion. At higher wave amplitudes (rhs), friction breaks down and the cantilever is sensitive to vertical movements only.

surface displacements, the cantilever experiences a quasi-static torsion as it is scanned over the surface. In this state, torsion is a nonlinear function of lateral (and vertical) displacements. In-plane surface oscillations consequently couple into the cantilever via this nonlinearity. However, as the wave amplitude is increased beyond the point of complete friction suppression ($F_f = 0$), the cantilever is no longer twisted. The reason is that the cantilever's effective rest position is shifted off the surface due to the mechanical diode effect.

The coupling mechanism is, however, not directly mediated through the dynamic altering of the friction coefficient since friction is largely unaffected by purely

in-plane polarized Love waves. Thus, there must exist an *effective* nonlinearity of the quasi-static torsion–distance relation that comes into play when the cantilever is already pre-twisted during scanning in the presence of friction (torsional angle $\varphi_{qs} \neq 0$). Without friction, the cantilever is quasi-relaxed ($\varphi_{qs} = 0$) and the nonlinearity is negligible. Now, in-plane surface oscillations of different amplitudes all lead to the same quasi-static (time-averaged) torsion $\varphi_{qs} = \overline{\varphi_{RF}} = 0$ and the lateral nonlinear coupling mechanism breaks down.

8.2. Lateral force rectification

So far, the investigations were limited to applications that are characterized by small to moderate RF powers, which are typical for SAW-AFM. For larger SAW amplitudes, however, surface forces can be generated that can be used to move macroscopic objects [153], liquid droplets [154] or to atomize droplets [155]. Now, the behavior of lateral forces in the limit of large oscillation amplitudes in strongly modulated wave fields will be discussed.

Figure 43 shows the SAW-LFM measurements in the backward (a) and forward (b) scan direction in the middle of a delay line on GaAs. The applied RF power was varied along the slow scan direction from +12 dBm to +24.5 dBm in steps of 0.5 dBm every 10 lines. The $12 \times 12 \mu\text{m}^2$ large area was scanned with a line frequency of 1 Hz. LFM forward and backward scans at selected SAW powers are given in (c); the presented data have been averaged over 10 scans. At +12 dBm, identical behavior to figure 40 is found: both LFM traces are complementary and modulated with the periodicity of the standing wave field ($2.6 \mu\text{m}$). The LFM hysteresis is still present. At higher applied power (+19 dBm), the hysteresis is

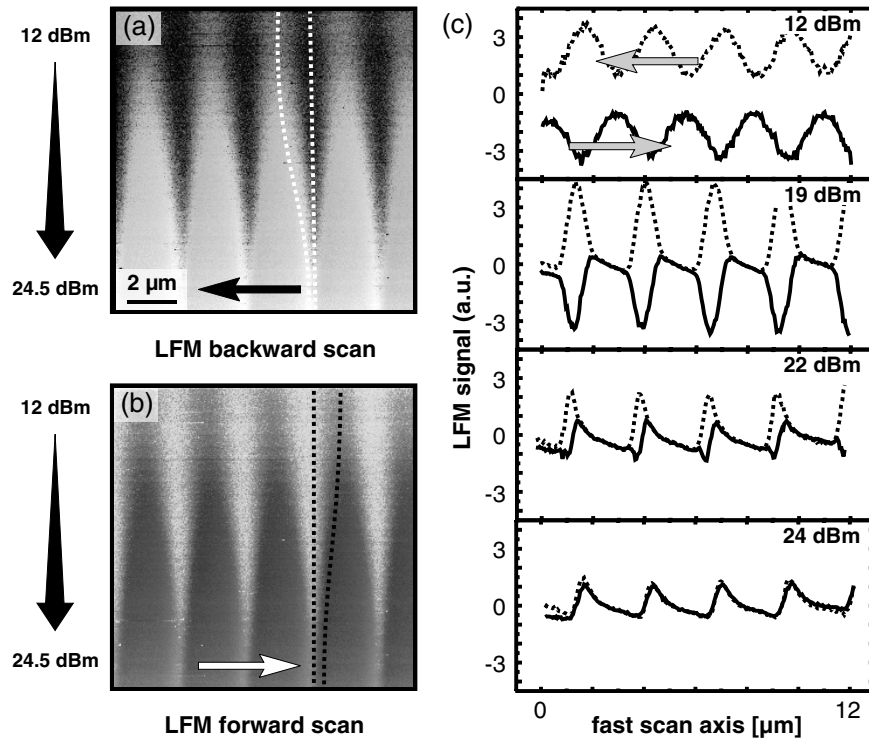


Figure 43. Amplitude dependence of the LFM signal in a strongly modulated standing wave field. LFM scans in the (a) forward and (b) backward scan direction. Along the y-axis, the RF power was increased. LFM scans for selected SAW powers are shown in (c).

completely suppressed around the maxima of the wave field. The behavior is analogous to that found in figure 41(a). For further increased power (+22 dBm), the hysteretic areas are further reduced and both traces are no longer symmetric about the line of zero friction.

When following the maxima and minima with increasing power (dotted lines in (a) and (b)), it appears that the maxima and minima merge into one point, while areas of vanishing friction dominate the image (forward and backward scans identical). Interestingly, at the maximum applied power of +24 dBm, the forward and backward scans merge, however, not as expected, exhibiting vanishing friction. Instead, a sawtooth-like shape is visible. Surprisingly, the sign of the force on the tip no longer changes its sign when reversing the scan direction, but is independent of the scan direction. Obviously, this case is different from the situation in figure 40, where the propagating wave contribution to the standing wave field is dominant and the LFM signal is vanishing.

To explain this counter-intuitive behavior, one has to take a look at the structure of the standing wave field. The oscillations within a Rayleigh wave consist of two parts: a vertical oscillation and a 90° phase shifted longitudinal component. In the present material system, the ratio of both oscillation amplitudes is 5 : 3. When two Rayleigh waves of equal amplitude are brought into interference, a standing wave field is formed whereby the nodes of one oscillation component coincide with the antinodes of the other component. Figure 44(a) illustrates this situation. The positions of the maxima of the vertical oscillation component are indicated by a dashed line. They correspond to the pattern that is observed by an SAW-AFM image. The maxima of the longitudinal

oscillation component are phase-shifted by 90° and are not detected in SAW-AFM (overshadowed by the vertical effect). Their positions are marked by a dotted line. In between the maxima of the respective components, both polarizations are superimposed and the local surface oscillation plane is tilted (gray arrows).

The consequences for the LFM signal are at low power initially dominated by the vertical oscillation component. Figure 44(b) illustrates this behavior, which was found experimentally as shown in figures 40 and 43. At the positions of the maxima of the vertical component (dashed line, black triangle), friction is reduced due to the mechanical diode effect and the LFM traces approach the zero friction line. A further increase in the power leads to a complete suppression of the friction at these positions. The LFM traces are still complementary, i.e. mirror-symmetric with regards to the zero friction line. Above this power level, the difference between the forward and backward scan traces vanishes—and thus friction.

Now, the longitudinal component of the wave field becomes relevant. As can be seen, the positions of vanishing friction coincide with the nodes (the zeros) of the longitudinal oscillation component (dashed line). The surface oscillation is thus entirely in the vertical direction. On the left and right of the nodes, a longitudinal component is added to the vertical movement. The sum of both thus leads to an inclined oscillation direction. In the case that the amplitude of this inclined oscillation is large enough, its vertical oscillation component can be rectified by the mechanical diode effect. As a result, a lateral force is acting on the tip which is independent of the scan direction of the cantilever and which is

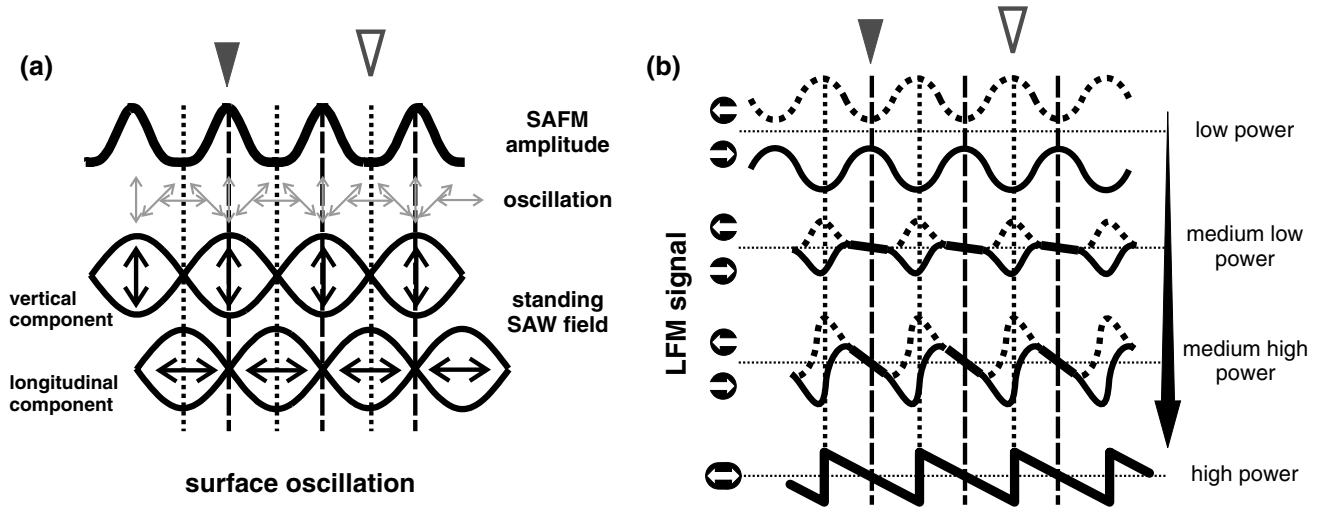


Figure 44. Schematic representation of the effect of lateral rectification: (a) illustrates the oscillation components within a standing Rayleigh wave field. In (b), the corresponding LFM signal is sketched as a function of SAW power. Dotted and dashed lines, as well as arrows, indicate identical positions in both scans.

always pointing away from the wave maxima. Contrary to this follows for the maxima of the longitudinal oscillation (dotted lines) that an additional lateral force is pointing toward their positions. As a consequence, the tip is alternately attracted and repelled—independent of its scan direction. These laterally rectifying forces vanish at the maxima of the vertical oscillation component and change their sign abruptly at the maxima of the longitudinal oscillation component.

Figure 44(b) illustrates this behavior in the form of a sawtooth-shaped characteristic. In reality, this characteristic is slightly different and the result of rather complicated nonlinear behavior. Nevertheless, this simple qualitative model is able to reproduce the experimental behavior found in figure 43. The four power regimes described in the model are roughly equivalent to the four power regimes shown in figure 43(c). In summary, it can be concluded that the macroscopic forces, which are the result of high-power SAW fields, were found in the presented microscopic model system as well and were explained qualitatively.

9. Technical applications—SAW device characterization

The spatially resolved investigation of wave fields is an important prerequisite for the development and optimization of novel SAW devices. Ultra-small SAW filters for the frequency range above 5 GHz deal with acoustic wavelengths in the sub-micrometer range that are hard to detect by conventional methods. At higher frequencies, second-order effects caused by SAW diffraction, electrode edges, propagation losses due to scattering at nanoscale surface inhomogeneities and mass loading effects become increasingly important. SAW-AFM is an ideal tool for studying these effects as it combines nanoscale lateral resolution imaging of topography and wave properties.

9.1. Resonator structures

The ability to detect in-plane polarized SAW modes [156] allows for the analysis of resonator devices which make use of transversally polarized acoustic modes. This type of device is of broad interest since the achievable frequencies are about 40% higher than in Rayleigh wave-based devices. A number of theoretical papers deal with their investigation (e.g. [157]), however, the number of experimental studies is rather small [158]. The general setup of a resonator device consists of input and output IDTs, surrounded by two reflector banks. The finger spacing in the Bragg reflectors is identical with the electrode spacing in the IDTs. The Bragg reflectors are several 100 wavelengths long and they are connected to RF ground. The very narrow reflection bandwidth of the reflectors leads to the high overall frequency selectivity of the device. The investigated STW resonator structure has been designed for an operating frequency of 510 MHz (bandwidth: 200 kHz) on AT-cut quartz. The crystal cut, in combination with the chosen propagation direction, leads to the desired temperature independent of the STW phase velocity. The working frequency was set to the maximum of the transmission spectrum.

The area shown in figure 45 is within the reflector, close to its aperture (horizontal edge) and shifted away from the center (toward the lower vertical edge). The amplitude (a) is obtained by analyzing the LFM signal at a reference frequency of 5 kHz in SAW-AFM mode; (b) depicts the topography. The $100 \times 100 \mu\text{m}^2$ scans were performed with a very low scan rate of 0.1 lines s^{-1} (40 min per image). The amplitude shows a standing wave field ($\lambda/2 = 5 \mu\text{m}$) with the wave maxima located on the reflector electrodes. Along the wave propagation direction only a small spatial variation of the amplitude is found as a result of the relatively small reflection coefficient of the individual reflector fingers. In the perpendicular direction, the amplitude decay is easily visible and the energy distribution can be quantified.

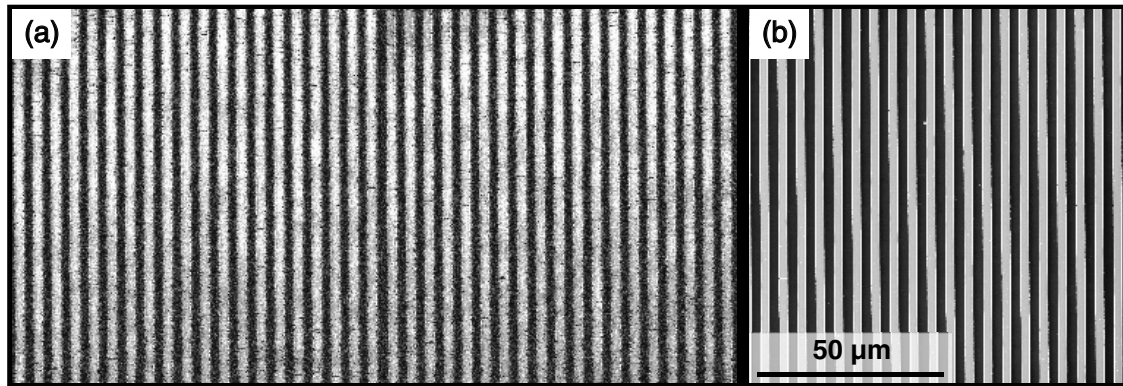


Figure 45. Amplitude image of a STW resonator structure: (a) shows the amplitude within one of the reflectors of the STW device and (b) the corresponding topography.

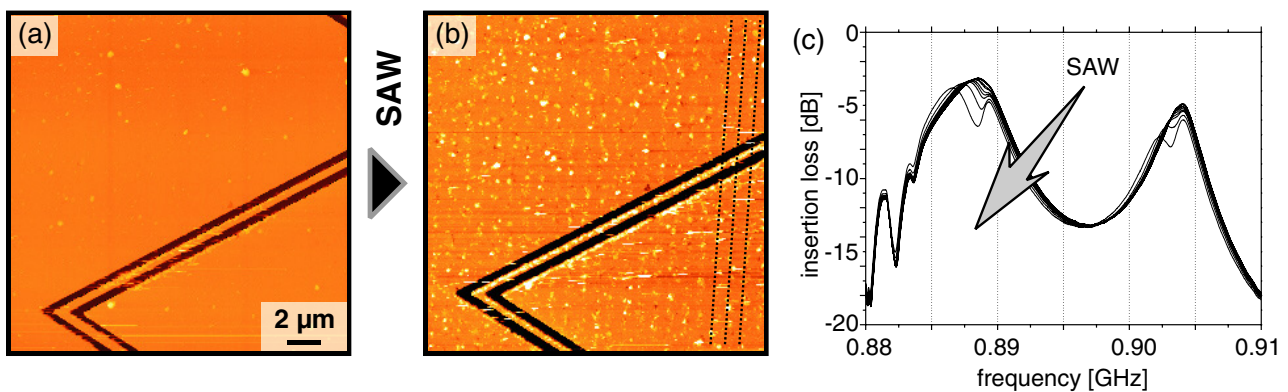


Figure 46. Damage of a thin metal film due to acoustomigration in a standing wave field. The $20 \times 20 \mu\text{m}^2$ topography scans, taken before (a) and after (b) the application of a power of +10 dBm to the test device for 4 h show rows of defects (bright contrast spots) that line up with the phase fronts of the wave field (indicated by the dotted lines). The corresponding transmission spectra as a function of time are shown in (c).

9.2. Acoustomigration

Stress-induced material transport in SAW devices—so-called acoustomigration—is a prominent failure mechanism, especially critical for high-power applications [159, 160]. Acoustomigration has its origin in the elastic wave-related stress acting on thin films and is thus a power-dependent phenomenon [161]. *In situ* high-resolution microscopy is essential for the study of acoustomigration as it is a phenomenon that not only results in the formation of macroscopic voids and hillocks but also affects the microscopic grain structure of the film. SAW-AFM allows through the simultaneous measurement of topography and wave amplitude for a direct correlation of damage and stress field distribution. Figure 46 shows the typical result of acoustomigration: damaged metallized areas within the standing wave field of a resonator device before (a) and after 4 h of loading at +10 dBm (b). It is obvious that high-power acoustic waves significantly alter the topography of the metal cavity. Interestingly, the bright spots in (b) line up along parallel lines (cf dotted lines). Furthermore, the performance of the device (insertion loss at the position of the resonances) is deteriorating as a function of loading time. The transmission spectra shown in figure 46(c) exhibit initially two resonances that get weaker and split as a result of acoustic loading. Although there are recipes to prolong the lifetime of

metallized areas in SAW devices, e.g., based on the addition of Cu to commonly used Al metallizations [162], little is known about the details of the damage mechanism. Its understanding, on the other hand, is the basis for improving the power resistance of metallizations.

SAW resonators are an ideal test medium for thin film migration and fatigue studies as their power densities are comparably high [162]. Note that since the typical operation frequencies are in the hundreds of megahertz, many damage cycles are accumulated in a short time. In order to extract precise information about the film damage, the acoustic power distribution has to be known at every time in the course of the stress testing. As the electrodes of the device also are subject to damage and thus changing the stress level in the whole structure, a special test device was designed [163]. An optical micrograph of the test device, consisting of IDTs, reflectors and the cavity, is shown in figure 47(c).

To correlate the lateral position of the film damage events with the stress distribution, topography and amplitude images are recorded simultaneously. Figure 47(a) shows the topography of the cavity and parts of the IDT, and (b) the corresponding vertical wave amplitude of the standing wave field obtained by SAW-AFM in vertical deflection mode. As the excited waves in the resonator are primarily in-plane polarized (>90%, cf (c)), and as the vertical detection mode is

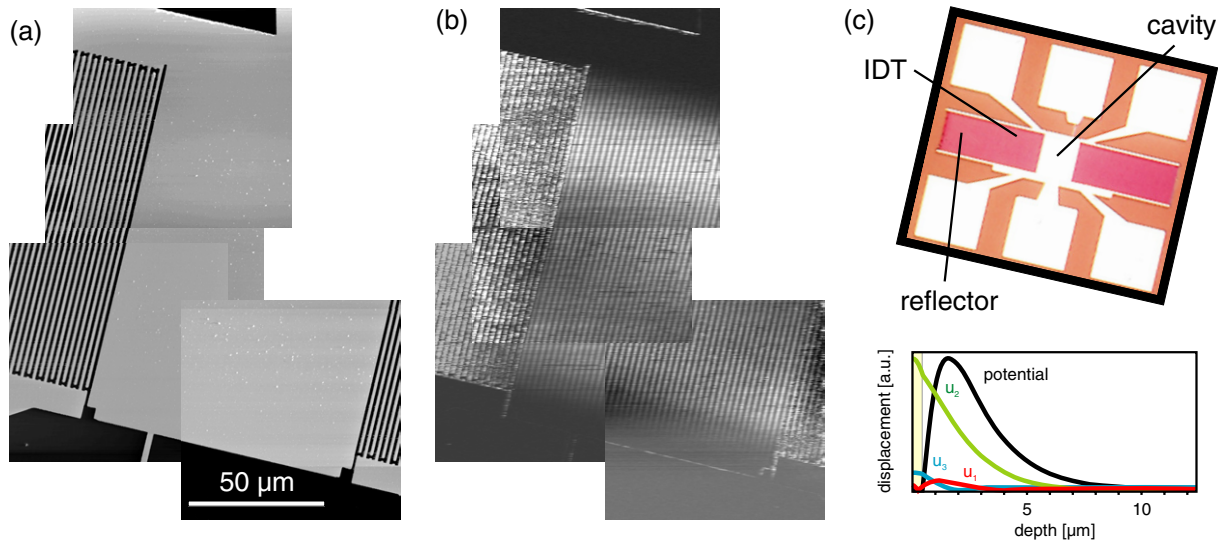


Figure 47. Standing wave field in the cavity of the test device: (a) topography and (b) out-of-plane component of the standing SAW field. (c) Optical micrograph of the test device and, below, distribution of the oscillation components and the electric field as a function of penetration depth. The yellow box indicates the metal film (vanishing electric potential) on the substrate. The transverse in-plane oscillation component u_2 dominates over the longitudinal in-plane component u_1 , and the out-of-plane component u_3 .

roughly an order of magnitude more sensitive than the in-plane detection mode, the contrast in out-of-plane and in-plane SAW-AFM is virtually the same for this particular sample. In such a case, however, out-of-plane detection is favored as it allows for faster scanning. For the amplitude mapping, a power of 0 dBm was applied to one of the IDTs. The frequency was set to the first resonance peak (889.5 MHz). The standing wave pattern exhibits a distance of $\lambda/2 = 2.2 \mu\text{m}$ between the amplitude maxima. As for the previously discussed resonator structure, the wave field quickly decays outside the propagation path which is defined by the acoustic aperture.

In the present test device, the amplitude maxima of the standing wave field are found to be at the lower electrode edge of the transducer region (see figures 48(a) and (b)). The strain maxima are shifted by 90° with respect to the amplitude maxima as strain is the derivative of displacement. With stress being proportional to the strain, the two are in phase with each other. The fact that stress is the driving source of acoustomigration is visualized in figure 48 (upper row: topography, lower row: amplitude distribution). In figures 48(a) and (b), the outer electrodes of the pristine transducer are visible, and figures 48(c) and (d) and figures 48(e) and (f) show the film damage after 15 min and 25 min, respectively, with the device powered at +7 dBm (note the different position and scale compared with figures 48(a) and (b)). The dotted lines are guides to the eye and indicate the positions of the amplitude minima in the standing wave field. Compared with figure 46, a closer look at the film reveals that the damaged areas of the pure Al film consist of hillocks and voids, as indicated in figure 48(c). Hillocks are protrusions on the surface of the film and are due to a relaxation of compressive stress. These areas, which are aligned with the displacement minima, correspond to the positions of maximum stress and are shifted by 90° with respect to the amplitude maxima. Comparing the topography scans after 15 and 25 min of operation, the dynamics of the film damage can

be observed. With increasing time, the surface roughens by forming a nonlinearly increasing number of hillocks and voids. In this power regime, the apparent size of these defects does not increase after an initial growth stage (cf 15 and 25 min). From these measurements, the migration process on a micrometer scale appears to be the growth of hillocks, driven by the formation of nearby voids ($<1 \mu\text{m}$) along the wave front.

Power-dependent damage experiments were performed (not shown), where the applied energy was kept constant. Independent of the power level, the formation of hillocks is the governing damage mechanism. With increasing power, an increasing number of hillocks is formed. However, the number of large hillocks does not increase above +13 dBm and, instead of forming new large hillocks ($>0.5 \mu\text{m}$), individual hillocks grow in size to a point at which they can be easily manipulated by the AFM tip.

10. Conclusions and perspectives

This review summarized SAW-assisted scanning probe microscopy. The key to detecting high-frequency signals by bandwidth-limited SPM is a nonlinear signal–distance relationship. The nonlinearity allows for the application of homodyne (self-mixing) and heterodyne (mixing of two detuned waves) detection schemes in AFM and STM. Homodyne detection by AFM relies on the mechanical rectification of the high-frequency surface oscillations, leading to a shift of the cantilever's rest position as a function of acoustic amplitude (\rightarrow mechanical diode effect). The heterodyne detection scheme requires a reference signal, either an acoustic wave or an electrical ac signal, at a slightly different frequency. The mixing of both signals at the nonlinearity then gives access to the wave's amplitude and phase.

With SAW-AFM, it was for the first time possible to image SAWs with nanometer-scale lateral resolution at gigahertz

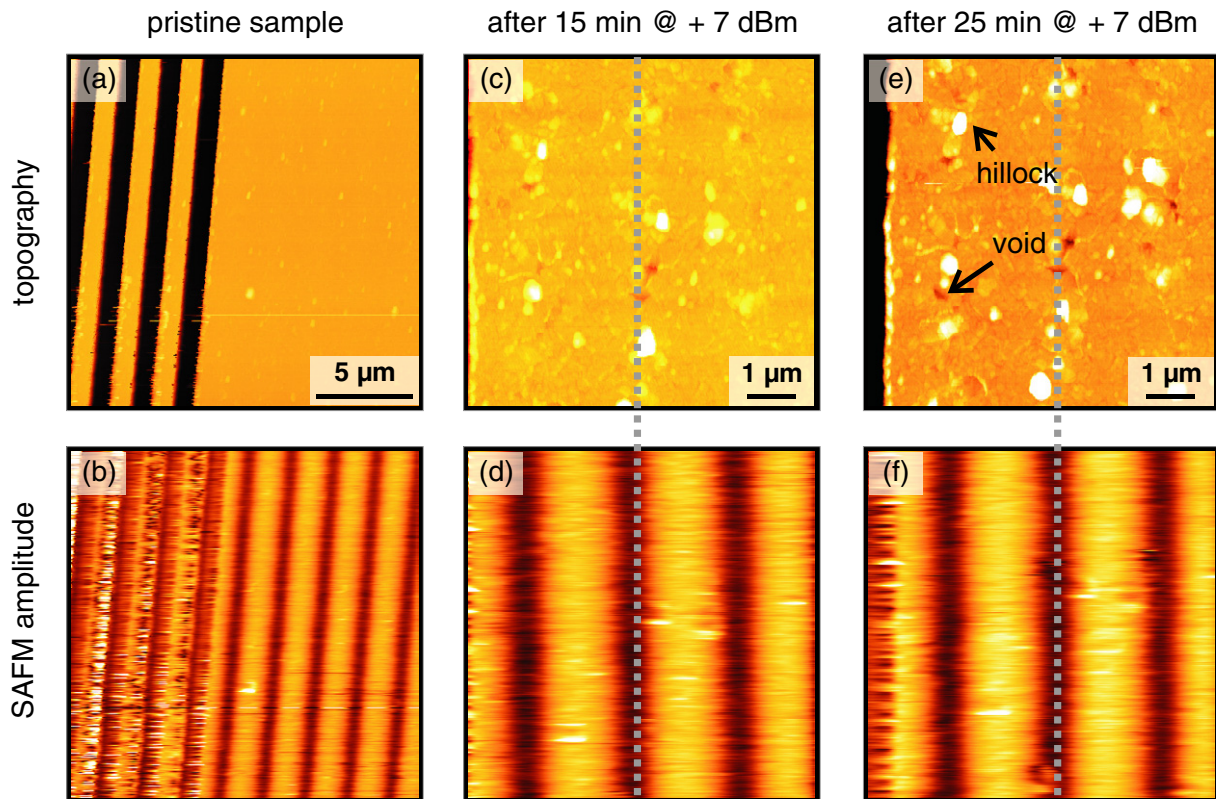


Figure 48. Correlation of film damage and amplitude distribution: topography (upper row) and out-of-plane SAW-AFM amplitude (lower row). In the left column, the pristine sample is shown. After 15 and 25 min of insonification at +7 dBm, hillocks and voids are forming as shown in the middle and rhs row, respectively. The dashed lines indicate the position of an amplitude minimum in the standing wave field, which coincides with an area of increased film damage.

frequencies. Examples were discussed in sections 4 and 9. SAW-AFM phase imaging has been employed to measure the phase velocity on the nanoscale (cf section 5). By solving the inverse problem of wave propagation numerically the elastic constants of the probed region are obtained. As differently polarized modes can be detected simultaneously, the precision for the determination of the elastic constants was considerably improved. An important advancement of the technique was the detection of in-plane polarized waves in LFM mode, as they are rather difficult to detect by other means. Based on the demonstration of Love wave detection, SAW-LFM was used for the successful search for high-velocity pseudo-SAWs. Moreover, it is rather astonishing that a nonlinear coupling mechanisms between in-plane oscillations and cantilever torsion exists. The reason lies in the concerted action of friction forces and surface roughness. Using SAW-LFM, the effect of ultrasound-induced superlubricity was reviewed (section 8). Superlubricity is a result of the mechanical diode effect, and in the investigated systems solely due to the vertical oscillation component of the wave. At higher wave amplitudes a lateral force rectification effect was found.

Elementary wave phenomena, such as scattering and diffraction from point-like sources, had not been studied before as the sensitivity of the available tools was not sufficient. In section 7 it was shown that SAW-AFM is capable of detecting very weak waves, whose signals are as much as 40 dB smaller than the reference wave. Wave reflection, mode

conversion and scattering off various microscopic objects have been discussed. These studies are of great relevance for the design and modeling of low-loss SAW devices. Further, the wave excitation from single SAW sources, such as single-finger electrodes, double-finger electrodes and point sources was successfully demonstrated. The SAW-AFM mixing technique allows an insight into the whole range of SAW-related phenomena, ranging from single elements—where pm oscillation amplitudes are detected—to local wave absorption studies.

In SAW-STM (section 6), the observed contrast was explained as a convolution of the local topography with the particle oscillation trajectory. On the nanoscale this leads to a contrast enhancement in the topography by differentiation of the image. On an atomic scale, surface oscillations reduce the topographic contrast and lead to surprising sub-atomic patterns in the phase and amplitude images. By using a simple model, the experimentally observed contrast was explained successfully.

For obtaining the elastic constants of spatially confined nanostructures, the precision in the determination of the phase velocity has to be further increased, e.g., by using ultra flat, high-resolution scan tables. Important systems that are in the focus of interest are ferroelectric domain structures and phase transitions in thin films. More flexibility will be given when the SAW excitation can be decoupled from the substrate (contact-free SAW excitation). For instance, by using a pulsed laser for the SAW excitation in combination with broadband

SPM detection [126], elastic spectroscopy up to 20 GHz seems feasible (by using SAW-STM [164]).

Acknowledgments

I would like to thank first and foremost G Behme and the tireless effort of our SAW engineer W Seidel, who both contributed extensively to this work. The development of SAW-AFM and SAW-STM is the result of many fruitful collaborations within the former Department for Nanoacoustics at the PDI in Berlin (E Chilla, H-J Fröhlich, J Enderlein, R Koch, P Voigt, Y Yang, C Flannery, D Rapoport), the other PDI departments, as well as collaborations with groups in Oxford (G A D Briggs and O Kolosov), Saarbrücken (W Arnold, S Hirsekorn and U Rabe), Besançon (M Bigler, P Vairac, F Sthal and B Cretin), Montpellier (J Attal), St Petersburg (S Makarov and S Semenov), Lausanne (N A Burnham and A J Kulik), and Boulder (D Hurley). I am especially thankful for the intense collaboration with EPCOS A.G. in Munich (W Ruile and F Kubat), and for the technical help by S Krauß and H Kostial. Finally, I want to express my gratitude to K H Ploog for his steady and solid support for this project. Funding from the DFG (Deutsche Forschungsgemeinschaft), the DAAD (Deutscher Akademischer Austauschdienst), the Humboldt Foundation, the Leopoldina, the National Science Foundation and the European Union is acknowledged.

References

- [1] Kulik A J, Kis A, Gremaud G, Hengsberger S, Zysset P K and Forró L 2005 *Nanotribology and Nanomechanics* ed B Bhushan (Berlin: Springer)
- [2] Vogel E M 2007 *Nature Nanotechnol.* **2** 25
- [3] Jain S C, Willander M and Maes H 1996 *Semicond. Sci. Technol.* **11** 641
- [4] Briggs A 1992 Acoustic microscopy—a summary *Rep. Prog. Phys.* **55** 851
- [5] Lemons R A and Quate C F 1974 *Appl. Phys. Lett.* **24** 163
- [6] Synge E H 1928 *Phil. Mag.* **6** 356
- [7] Dürr W, Sinclair D A and Ash E A 1980 *Electron. Lett.* **21** 805
- [8] Vairac P and Cretin B 1996 *Appl. Phys. Lett.* **68** 461
- [9] Takata K, Hasegawa T, Hosaka S, Hosoki S and Komoda T 1989 *Appl. Phys. Lett.* **55** 1718
- [10] Rohrbeck W and Chilla E 1992 *Phys. Status Solidi a* **131** 69
- [11] Kolosov O and Yamanaka K 1993 *Japan. J. Appl. Phys.* **32** L1095
- [12] Yamanaka K, Ogiso H and Kolosov O 1994 *Japan. J. Appl. Phys.* **33** 3197
- [13] Yamanaka K, Ogiso H and Kolosov O 1994 *Appl. Phys. Lett.* **64** 178
- [14] Huey B D 2007 *Ann. Rev. Mater. Res.* **37** 351
- [15] Rabe U and Arnold W 1994 *Appl. Phys. Lett.* **64** 1493
- [16] Hirsekorn S, Rabe U and Arnold W 1996 *Europhys. News* **27** 93
- [17] Rabe U, Amelio S, Kester E, Scherer V, Hirsekorn S and Arnold W 2000 *Ultrasonics* **38** 430
- [18] Jamitzky F, Stark M, Bunk W, Heckl W M and Stark R W 2006 *Nanotechnology* **17** S213
- [19] Scherer V, Arnold W and Bhushan B 1999 *Surf. Interface Anal.* **27** 578
- [20] Amelio S, Goldade A V, Rabe U, Scherer V, Bhushan B and Arnold W 2001 *Thin Solid Film* **392** 75
- [21] Burnham N A, Kulik A J, Gremaud G, Gallo P-J and Oulevey F 1996 *J. Vac. Sci. Technol. B* **14** 794
- [22] Huey B D, Langford R M, Briggs G A D and Kolosov O V 2001 *Microsc. Semicond. Mater.* **169** 531
- [23] Kolosov O V, Castell M R, Marsh C D, Briggs G A D, Kamins T I and Williams R S 1998 *Phys. Rev. Lett.* **81** 1046
- [24] Burnham N A, Kulik A J, Gremaud G and Briggs G A D 1995 *Phys. Rev. Lett.* **74** 5092
- [25] Oulevey F, Gremaud G, Semoroz A, Kulik A J, Burnham N A, Dupas E and Gourdon D 1998 *Rev. Sci. Instrum.* **69** 2085
- [26] Cuberes M T, Assender H E, Briggs G A D and Kolosov O V 2000 *J. Phys. D: Appl. Phys.* **33** 2347
- [27] Cantrell S A, Cantrell J H and Lillehei P T 2007 *J. Appl. Phys.* **101** 114324
- [28] Parlak Z and Degertekin F L 2008 *J. Appl. Phys.* **103** 114910
- [29] Cantrell J H and Cantrell S A 2008 *Phys. Rev. B* **77** 165409
- [30] Dinelli F, Biswas S K, Briggs G A D and Kolosov O V 2000 *Phys. Rev. B* **61** 13995
- [31] Shekhawat G S and Dravid V P 2005 *Science* **310** 89
- [32] Lord Rayleigh 1885 *Proc. Lond. Math. Soc.* **17** 4
- [33] Hickernell F S 1999 *Physical Acoustics* vol 24 (San Diego, CA: Academic)
- [34] Pereira da Cunha M P and Adler E L 1995 *IEEE Trans. Ultrason. Ferroelectr. Freq. Control* **UFFC-42** 840
- [35] Fahmy A H and Adler E L 1973 *Appl. Phys. Lett.* **22** 495
- [36] Makarov S, Chilla E and Fröhlich H-J 1995 *J. Appl. Phys.* **78** 5028
- [37] White R M and Voltmer F W 1965 *Appl. Phys. Lett.* **7** 314
- [38] Skeie H and Engan H 1975 *Radio Electron. Eng.* **45** 207
- [39] Tancrèll R H 1977 *Surface Wave Filters* ed H Matthews (New York: Wiley)
- [40] Smith W R, Gerard H M, Collins J H, Reeder T W and Shaw H J 1969 *IEEE Trans. Microw. Theory Tech.* **MTT-17** 856
- [41] Hartmann C S, Bell D F and Rosenfeld R C 1973 *IEEE Trans. Microw. Theory Tech.* **MTT-21** 162
- [42] Campbell C 1989 *Surface Acoustic Wave Devices and Their Signal Processing Applications* (San Diego, CA: Academic)
- [43] Datta S 1986 *Surface Acoustic Wave Devices* (Englewood Cliffs, NJ: Prentice-Hall)
- [44] Daniau W, Kumar A K S, Paruch P, Marré D, Triscone J-M and Ballandras S 2004 *Proc. IEEE Ultrasonics Symp. (Montreal)* (New York: IEEE) p 441
- [45] Hickernell F S 1985 *IEEE Trans. Sonics Ultrason.* **SU-32** 621
- [46] Namba A, Sugimoto M, Ogura T, Tomita Y and Eda K 1995 *Appl. Phys. Lett.* **67** 3275
- [47] Hess P 1989 *Topics in Current Physics* vol 42 (Berlin: Springer)
- [48] Nishino H, Tsukahara Y, Nagata Y, Koda T and Yamanaka K 1993 *Appl. Phys. Lett.* **62** 2036
- [49] Arnold W, Betz B and Hoffman B 1985 *Appl. Phys. Lett.* **47** 672
- [50] Lin K H, Yu C T, Sun S Z, Chen H P, Pan C C, Chyi J I, Huang S W, Li P C and Sun C K 2006 *Appl. Phys. Lett.* **89** 043106
- [51] Ippen E P 1967 *Proc. IEEE Ultrasonics Symp. (Vancouver)* (New York: IEEE) p 248
- [52] Monchalain J-P 1986 *IEEE Trans. Ultrason. Ferroelectr. Freq. Control* **UFFC-33** 485
- [53] Engan H 1978 *IEEE Trans. Sonics Ultrason.* **SU-25** 372
- [54] Tanski W J and Wittels N D 1979 *Appl. Phys. Lett.* **34** 537
- [55] Eberharter G and Feuerbaum H P 1980 *Appl. Phys. Lett.* **37** 698
- [56] Richardson B A and Kino G S 1970 *Appl. Phys. Lett.* **16** 82
- [57] Chiba T and Togami Y 1976 *Appl. Phys. Lett.* **29** 793
- [58] Cerva H and Graeff W 1985 *Phys. Status Solidi a* **87** 35
- [59] Cerva H and Graeff W 1985 *Phys. Status Solidi a* **87** 507
- [59] Vines R E and Wolfe J P 1999 *Physica B* **263-264** 567

- [60] Schneider D, Schwarz T and Schultrich B 1992 *Thin Solid Films* **219** 92
- [61] Siegel R W 1994 *Encyclopedia of Applied Physics* vol 11 ed G L Trigg (Weinheim: VCH)
- [62] Winau D, Koch R, Führmann A and Rieder K H 1991 *J. Appl. Phys.* **70** 3081
- [63] Wolf D and Lutsko J F 1988 *Phys. Rev. Lett.* **60** 1170
- [64] Veprek S and Reiprich S 1995 *Thin Solid Films* **268** 64
- [65] Tan I H, Mirin R, Jayaraman V, Shi S, Hu E and Bowers J 1992 *Appl. Phys. Lett.* **61** 300
- [66] Achenbach J D 1995 *Advances in Acoustic Microscopy* vol 1 ed A Briggs (New York: Plenum) p 153
- [67] Turner J A, Hirsekorn S, Rabe U and Arnold W 1997 *J. Appl. Phys.* **82** 966
- [68] Cuberes M T 2009 *J. Nanomater.* 762016
- [69] Hou A S, Ho F and Bloom D M 1992 *Electron. Lett.* **28** 2302
- [70] Hesjedal T, Chilla E and Fröhlich H-J 1995 *Appl. Phys. A* **61** 237
- [71] Schmidt J, Rapoport D H, Behme G and Fröhlich H-J 1999 *J. Appl. Phys.* **86** 7094
- [72] Burnham N A and Colton R J 1989 *J. Vac. Sci. Technol. A* **7** 2906
- [73] Hesjedal T, Chilla E and Fröhlich H J 1997 *Appl. Phys. Lett.* **70** 1372
- [74] Israelachvili J N 1985 *Intermolecular and Surface Forces* (London: Academic)
- [75] Cutler P H, Feuchtwang T E, Tsong T T, Nguyen H and Lucas A A 1987 *Phys. Rev. B* **35** 7774
- [76] Lucas A A, Culter P H, Feuchtwang T E, Tsong T T, Sullivan T E, Kuk Y, Nguyen N and Silverman P J 1988 *J. Vac. Sci. Technol. A* **6** 461
- [77] Smith D P E, Binnig G and Quate C F 1986 *Appl. Phys. Lett.* **49** 1641
- [78] Chilla E, Fröhlich H-J, Riedel J and Rohrbeck W 1989 *Proc. 8. Tagung Akustik/ 11. Winterschule Mikroakustik* (Berlin: Phys. Ges. Berlin) p 212
- [79] Rohrbeck W, Chilla E, Fröhlich H-J and Riedel J 1991 *Appl. Phys. A* **52** 344
- [80] Strozewski K J, McBride S E and Wetsel G C Jr 1992 *Ultramicroscopy* **42-44** 388
- [81] McBride S E and Wetsel C G Jr 1992 *Proc. IEEE Ultrasonics Symp. (Tucson, AZ)* (New York: IEEE) p 445
- [82] Chen C J 1993 *Introduction to Scanning Tunneling Microscopy* (New York: Oxford University Press)
- [83] Ueha S, Shiota K, Okada T and Tsujiuchi J 1975 *Japan. J. Appl. Phys.* **14** 335
- [84] Holmgren O, Knuuttila J V, Makkonen T, Kokkonen K, Plessky V P, Steichen W, Solal M and Salomaa M M 2005 *Appl. Phys. Lett.* **86** 024101
- [85] Martin G, Weihnacht M and Franke K 1995 *Proc. IEEE Ultrasonics Symp. (Seattle, WA)* (New York: IEEE) p 291
- [86] Odagawa H, Qureshi J A, Meguro T and Yamanouchi K 1998 *Japan. J. Appl. Phys.* **37** 2927
- [87] Takagaki Y, Hesjedal T, Brandt O, Ploog K H 2004 *Semicond. Sci. Technol.* **19** 256
- [88] Behme G 2001 Rasterkraftmikroskopische Untersuchung hochfrequenter akustischer Oberflächenwellenfelder *PhD Thesis* Humboldt University, Berlin
- [89] Dupas E, Behme G, Burnham N, Kulik A, Chilla E and Fröhlich H-J 1999, unpublished
- [90] Auld B A 1990 *Acoustic Fields and Waves in Solids* (Malabar, FL: Krieger)
- [91] Maynard J 1996 *Phys. Today* **49** 26
- [92] Giessibl F-J 1995 *Science* **267** 68
- [93] Chilla E, Hesjedal T and Fröhlich H-J 1997 *Phys. Rev. B* **55** 15852
- [94] See, for instance, PI's PicoCube at <http://www.physikinstrumente.com>
- [95] Behme G, Hesjedal T, Chilla E and Fröhlich H-J 1998 *Appl. Phys. Lett.* **73** 882
- [96] Lewis M 1977 *Proc. IEEE Ultrasonics Symp. (Phoenix, AZ)* (New York: IEEE) p 744
- [97] Herrmann F and Büttgenbach S 1998 *Phys. Status Solidi a* **131** R3
- [98] Love A E H 1911 *Some Problems of Geodynamics* (London: Cambridge University Press)
- [99] Wohltjen H 1984 *Sensors Actuators* **5** 307
- [100] Biryukov S V and Weihnacht M 1998 *J. Appl. Phys.* **83** 3276
- [101] Makarov S and Belkova A 1997 *Appl. Phys. Lett.* **70** 2100
- [102] Sato T, Ohkubo Y and Abe H 1999 *IEEE Trans. Ultrason. Ferroelectr. Freq. Control* **UF46-46** 383
- [103] Behme G, Hesjedal T, Chilla E and Fröhlich H-J 1999 *Surf. Interface Anal.* **27** 558
- [104] Pereira da Cunha M 1997 *Proc. IEEE Ultrasonics Symp. (Toronto)* (New York: IEEE) p 239
- [105] Behme G and Hesjedal T 2001 *IEEE Transact. Ultrason. Ferroelectr. Freq. Control* **48** 1132
- [106] Behme G and Hesjedal T 2000 *Appl. Phys. Lett.* **77** 759
- [107] Chilla E, private communication
- [108] Slobodnik A J, Conway E D and Delmonico R T 1973 *Microwave Acoustic Handbook* (Springfield, VA: NTIS)
- [109] Hamers R J and Cahill D G 1990 *Appl. Phys. Lett.* **57** 2031
- [110] Bridges G E, Said R A and Thompson D J 1993 *Electron. Lett.* **29** 1448
- [111] Botkin D, Weiss S, Ogletree D F, Beeman J, Salmeron M and Chemla D S 1995 *Rev. Sci. Instrum.* **66** 4130
- [112] Kochanski G P 1989 *Phys. Rev. Lett.* **62** 2285
- [113] Seifert W, Gerner E, Stachel M and Dransfeld K 1992 *Ultramicroscopy* **42-44** 379
- [114] Nunes Jr. G and Freeman M R 1993 *Science* **262** 1029
- [115] Weiss S, Ogletree D F, Botkin D, Salmeron M and Chemla D S 1993 *Appl. Phys. Lett.* **63** 2567
- [116] Chilla E, Rohrbeck W, Fröhlich H-J and Riedel J 1992 *Acoustical Imaging* vol 19 ed H Ermert and H-P Harjes (New York: Plenum) p 737
- [117] Chilla E, Rohrbeck W, Fröhlich H-J, Koch R and Rieder K H 1994 *Ann. Phys., Lpz.* **3** 21
- [118] Abraham D W, Williams C C and Wickramasinghe H K 1988 *Appl. Phys. Lett.* **53** 1503
- [119] Stoll E P and Gimzewski J K 1991 *J. Vac. Sci. Technol. B* **9** 643
- [120] Stoll E, Baratoff A, Selloni A and Carnevali P 1984 *J. Phys. C: Solid State Phys.* **17** 3073
- [121] Voigt P 2002 Untersuchungen akustischer Oberflächenwellenfelder auf der Nanometerskala *PhD Thesis* Humboldt University, Berlin
- [122] Koch R and Yang J 2005 *J. Appl. Phys.* **97** 104321
- [123] Tersoff J and Hamann D R 1985 *Phys. Rev. B* **31** 805
- [124] Chilla E, Rohrbeck W, Fröhlich H-J, Koch R and Rieder K H 1992 *Appl. Phys. Lett.* **61** 3107
- [125] Heil J, Wesner J and Grill W 1988 *J. Appl. Phys.* **64** 1939
- [126] Stranik S J and Weiss P S 1993 *Rev. Sci. Instrum.* **64** 1232
- [127] Mizutani W, Michel B, Schierle R, Wolf H and Rohrer H 1993 *Appl. Phys. Lett.* **63** 147
- [128] Hesjedal T, Chilla E and Fröhlich H-J 1996 *Appl. Phys. Lett.* **69** 354
- [129] Hallmark V M, Chiang S, Rabolt J F, Swalen J D and Wilson R J 1987 *Phys. Rev. Lett.* **59** 2879
- [130] Behme G and Hesjedal T 2001 *Appl. Phys. A* **72** 491
- [131] Hesjedal T and Behme G 2001 *Appl. Phys. Lett.* **78** 1948
- [132] Kushwaha M S, Halevi P, Dobrzynski L and Djafari-Rouhani B 1993 *Phys. Rev. Lett.* **71** 2022
- [133] Macon L, Desideri J P and Sornette D 1991 *Phys. Rev. B* **44** 6755
- [134] Tanaka Y, Narita M and Tamura S 1998 *J. Phys.: Condens. Mater.* **10** 8787

- [135] Zidek H P, Baghai-Wadji A and Männer O 1993 *Proc. IEEE Ultrasonics Symp. (Baltimore, MD)* (New York: IEEE) p 149
- [136] Pereira da Cunha M and Adler E L 1995 *IEEE Trans. Ultrason. Ferroelectr. Freq. Control* **UFFC-42** 168
- [137] Hesjedal T and Behme G 2000 *Electron. Lett.* **36** 1903
- [138] Hesjedal T and Behme G 2001 *IEEE Trans. Ultrason. Ferroelectr. Freq. Control Lett.* **48** 641
- [139] Hesjedal T and Behme G 2001 *Europhys. Lett.* **54** 154
- [140] Hesjedal T and Behme G 2001 *Appl. Phys. Lett.* **79** 1054
- [141] Penunuri D and Lakin K M 1975 *Proc. IEEE Ultrasonics Symp. (Los Angeles, CA)* (New York: IEEE) p 478
- [142] Maznev A A, Lomonosov A M, Hess P and Kolomenskii A A 2003 *Europ. Phys. J. B* **35** 429
- [143] Meyer G and Amer N M 1990 *Appl. Phys. Lett.* **57** 2089
- [144] Fridman H D and Levesque P 1959 *J. Appl. Phys.* **30** 1572
- [145] Pohlman R and Lehfeldt E 1966 *Ultrasonics* **4** 178
- [146] Dinelli F, Biswas S K, Briggs G A D and Kolosov O V 1997 *Appl. Phys. Lett.* **71** 1177
- [147] Tsai C C and Tseng C H 2006 *Arch. Appl. Mech.* **75** 164
- [148] Cuberes M T 2007 *Fundamentals of Friction and Wear on the Nanometer Scale* ed E Gnecco and E Meyer (Berlin: Springer) p 49
- [149] Cuberes M T 2009 *Applied Scanning Probe Methods* ed B Bhushan, H Fuchs and H Yamada (Berlin: Springer)
- [150] Hesjedal T and Behme G 2002 *IEEE Trans. Ultrasonics Ferroelectr. Freq. Control* **UFFC-49** 356
- [151] Behme G and Hesjedal T 2001 *J. Appl. Phys.* **89** 4850
- [152] Behme G and Hesjedal T 2000 *Appl. Phys. A* **70** 361
- [153] Kurosawa M K, Takahashi M and Higuchi T 1998 *IEEE Trans. Ultrasonics Ferroelectr. Freq. Control* **UFFC-45** 1229
- [154] Wixforth A 2003 *Superlatt. Microstruct.* **33** 389
- [155] Yamamoto A, Nishimura M, Ooishi Y, Tsukada N and Higuchi T 2006 *J. Robotics Mechatron.* **18** 146
- [156] Hesjedal T, Fröhlich H-J and Chilla E 1998 *Appl. Phys. A* **66** S325
- [157] Gavignet E, Ballandras S and Bigler E 1995 *J. Appl. Phys.* **77** 6228
- [158] Gualtieri J G and Kosinski J A 1996 *IEEE Trans. Instrum. Meas.* **45** 872
- [159] Bell D 1977 *Proc. IEEE Ultrason. Symp. (Phoenix, AZ)* (New York: IEEE) p 851
- [160] Shreve W R 1977 *Proc. IEEE Ultrason. Symp. (Phoenix, AZ)* (New York: IEEE) p 857
- [161] Shreve W R, Bray R C, Elliott S and Chu Y C 1981 *Proc. IEEE Ultrason. Symp.* (New York: IEEE) p 94
- [162] Latham J I, Shreve W R, Tolar N J and Ghate P B 1979 *Thin Solid Films* **64** 9
- [163] Ruile W, Raml G, Springer A and Weigel R 2000 *Proc. IEEE Ultrason. Symp.* (New York: IEEE) p 275
- [164] Hesjedal T, Chilla E and Fröhlich H-J 1996 *J. Vac. Sci. Technol. B* **15** 1569